Icarus 274 (2016) 131–162

Contents lists available at ScienceDirect

Icarus

journal homepage: www.elsevier.com/locate/icarus

Noncircular features in Saturn's rings III: The Cassini Division

Richard G. French[a,*], Philip D. Nicholson[b], Colleen A. McGhee-French[a], Katherine Lonergan[a], Talia Sepersky[a], Mathew M. Hedman[c], Essam A. Marouf[d], Joshua E. Colwell[e]

[a] Department of Astronomy, Wellesley College, Wellesley, MA 02481, USA
[b] Department of Astronomy, Cornell University, Ithaca, NY 14853, USA
[c] Department of Physics, University of Idaho, Moscow, ID 83844,USA
[d] Department of Electrical Engineering, San Jose State University, San Jose, CA 95192, USA
[e] Department of Physics, University of Central Florida, Orlando, FL 32816, USA

ARTICLE INFO

Article history:
Received 4 February 2016
Revised 17 March 2016
Accepted 21 March 2016
Available online 4 April 2016

Keywords:
Occultations
Planetary rings

ABSTRACT

We have conducted a comprehensive survey of 22 sharp-edged ringlets and gaps in the Cassini Division of Saturn's rings, making use of nearly 200 high-SNR stellar and radio occultation chords obtained by the *Cassini* VIMS, UVIS, and RSS instruments between 2005 and 2013. We measure eccentricities from as small as $ae = 80$ m to nearly 30 km, free normal modes with amplitudes from ~ 0.1 to 4.1 km, and detectable inclinations as small as $a \sin i = 0.2$ km. Throughout the entire region, the Mimas 2.1 ILR (inner Lindblad resonance) produces systematic forced $m = 2$ distortions that quantitatively match the expected amplitudes, phases, and pattern speed. The narrow Russell, Jeffreys, Kuiper, Bessel, and Barnard gaps are simplest, and do not contain dense ringlets. Their outer edges are generally quite sharp and four of them are circular to within ~0.25 km, whereas most of the inner gap edges have significant eccentricities. Three gaps are more complex, containing one or more isolated ringlets. First among these is the 361 km-wide Huygens gap, containing two ringlets. The wider Huygens ringlet has nearly identical eccentricities on the two edges, in addition to OLR-type (outer Lindblad resonance) normal modes on the inner edge and ILR-type modes on the outer edge. A secondary $m = 1$ (eccentric) mode is present on the outer edge of the ringlet, with a pattern speed similar to that of the B ring's outer edge. Variations in the ringlet's width are complex, but are statistically consistent with the expected magnitudes resulting from the random superposition of the multiple normal modes on the two edges. Also present in the Huygens gap is the very narrow so-called Strange ringlet, with a substantial eccentricity and inclination, as well as both ILR- and OLR-type normal modes. The 100 km-wide Herschel gap's inner edge is highly eccentric, with at least seven ILR-type normal modes. The outer gap edge is also eccentric, and hosts four OLR-type normal modes, and a secondary $m = 1$ mode with a pattern speed quite close to that of the B ring's outer edge. The Herschel ringlet itself is eccentric and inclined, but neither the pericenters nor the nodes are well-aligned. The third of the complex gaps is the 241 km-wide Laplace gap, containing the Laplace ringlet. Both gap edges are eccentric, with very similar pericenter longitudes and apsidal precession rates, in spite of their large radial separation. The Laplace ringlet has eccentric edges and an abundance of normal modes. Like the Herschel ringlet, the Laplace ringlet does not precess rigidly and does not conform to the usual dynamical picture of an eccentric ringlet. Normal modes are abundant in the Cassini Division. Consistently, we find free ILR-type normal modes ($m > 0$) at the outer edges of ringlets and the inner edges of gaps, and free OLR-type normal modes ($m \leq 0$) at inner ringlet edges and outer edges of gaps, as expected from the resonant cavity model of normal modes. We estimate the surface density of ring features from the resonance locations of the normal modes. The Cassini Division exhibits apsidal precession rates that are anomalously large, compared to the predicted values based on Saturn's zonal gravity field. The overall radial trend matches the secular contribution expected from the nearby B ring, assuming a surface mass density of $\Sigma = 100$ gm cm^{-2}. However, the outer edges of the

* Corresponding author. Tel.: +781 283 3747.
E-mail address: rfrench@wellesley.edu (R.G. French).

http://dx.doi.org/10.1016/j.icarus.2016.03.017

Huygens and Laplace gaps, and the outer edge of the Laplace ringlet, have conspicuously large residuals, exceeding their predicted precession rates by more than $0.03^\circ\,d^{-1}$. These patterns are probably the result of forcing by nearby ring material, but at present we cannot account for them in detail.

1. Introduction

Conventionally, Saturn's main ring system is subdivided into three components: the A, B and C rings, in order of decreasing radius. The Cassini Division lies between the brighter A and B rings, at approximately 1.97 Saturn radii ($1\,R_S = 60,330$ km), and is ~4500 km wide. Its normal optical depth averages ~0.1 (Colwell et al., 2009b; Cuzzi et al., 1984), comparable to broad areas of the C ring, which it strongly resembles in structure and in its spectral and particle properties. As first revealed in *Voyager* images (Smith et al., 1982), the Cassini Division is a highly complex region, with eight distinct gaps that in turn contain at least seven narrow ringlets. Most of these features have now been given official names by the IAU, as indicated in Fig. 1. Starting at the outer edge of the B ring—which is controlled and strongly perturbed by the Mimas 2:1 inner Lindblad resonance (Goldreich and Tremaine, 1978; Porco et al., 1984)—we find the 361 km-wide Huygens gap, the Herschel gap (95 km), the Russell gap (38 km), the Jeffreys gap (37 km), the Kuiper gap (4.6 km), the Laplace gap (241 km), the Bessel gap (12.5 km) and the Barnard gap (12.4 km). The Huygens, Herschel and Laplace gaps contain a total of four narrow, dense ringlets that are visibly noncircular. While the Huygens ringlet was named at the time of the *Voyager* encounters, those in the Herschel and Laplace gaps have previously been informally referred to as the 1.960 R_S and 1.990 R_S ringlets (Nicholson et al., 1990), based on their mean distances from Saturn's center. We shall simply refer to them as the Herschel and Laplace ringlets. A fourth ringlet, identified as R6 by Colwell et al. (2009b) in their list of Cassini Division ringlets and gaps, but informally dubbed the Strange ringlet, inhabits the outer part of the Huygens gap, and was first identified in *Cassini* images. In addition to these relatively prominent ringlets, *Cassini* images have revealed the presence of at least three more tenuous ringlets within the Huygens, Jeffreys and Laplace gaps (Porco et al., 2005).

There are relatively few previous kinematic studies of these features, prior to the advent of *Cassini* data. Lissauer et al. (1981) proposed that each gap might contain a small satellite, which would prevent the gap from collapsing by counteracting the viscous torque in the rings. *Cassini* images have so far failed to reveal any Moons within the Cassini Division, although the validity of this general concept was later confirmed by the discovery of two such Moons in the outer A ring: Pan, which orbits within the Encke gap (Showalter, 1991) and Daphnis, which occupies a similar place in the Keeler gap (Porco et al., 2005). It is perhaps significant that both of these gaps lie much closer to the Roche limit for icy bodies than does the Cassini Division.

Besides the outer edge of the B ring, the most obviously noncircular feature in the Cassini Division seen in *Voyager* images was the nearby Huygens ringlet. This feature was studied by Porco (1983) and Turtle et al. (1991), and although no completely satisfactory model was obtained, it was established that the ringlet's perturbations have both $m = 1$ (i.e., keplerian) and $m = 2$ components. The latter were assumed to be driven by the nearby Mimas resonance. These studies were updated using early *Cassini* images by Spitale and Porco (2006), and in a more extensive recent study by Spitale and Hahn (2016), based on nearly a decade of *Cassini* ISS data.

Marouf and Tyler (1986), using the single radio occultation profile returned by *Voyager* 1, examined the wavelike structures in the regions on either side of the Herschel gap, interpreting these as satellite wakes analogous to the recently-discovered Pan wakes in the A ring (Showalter et al., 1986). However, Flynn and Cuzzi (1989) found that these structures are axisymmetric and more likely permanent features of the rings. The latter also examined the edges of the Huygens and Herschel gaps in multiple *Voyager* images, concluding that the inner edge of the latter is eccentric.

Nicholson et al. (1990), in their study of the radius scale of the rings using *Voyager* radio and stellar occultation data, first noted that the ringlets in the Herschel and Laplace gaps were also noncircular and that the same was probably true of what they referred to as the 1.994 R_S ringlet (now considered to be the region between the Bessel and Barnard gaps; see Fig. 1). With only two occultation cuts, however, they were unable to estimate the ringlets' shapes or eccentricities.

Hedman et al. (2010) carried out the first systematic studies of the Cassini Division using *Cassini* data, measuring the radii of all eight gap edges in a set of 41 stellar occultation profiles from the VIMS instrument. French et al. (2010) performed a similar analysis with a set of 10 radio occultation profiles from the RSS experiment. Their principal results, as summarized in Table 3 of Hedman et al. (2010), were as follows:

- The *outer* edges of the Russell, Jeffreys, Kuiper, Barnard and (possibly) Bessel and Herschel gaps are circular to within ~1 km.
- In addition to the Huygens ringlet, the *inner* edges of the Herschel, Russell, Jeffreys, Kuiper, Laplace and Bessel gaps, as well as the *outer* edges of the Laplace ringlet and gap, are elliptical, with apsidal precession rates that match those calculated from Saturn's zonal gravity harmonics.
- The inner edge of the Barnard gap is also noncircular, but is not well fit by a precessing $m = 1$ model. Instead, it appears to exhibit an $m = 5$ perturbation, perhaps forced by the nearby Prometheus 5:4 ILR.
- The inner edge of the Laplace ringlet, both edges of the Herschel ringlet and the outer edge of the Huygens gap are measurably noncircular, but were not satisfactorily fit by any of the models they considered.

In the present paper we update these results and re-examine the edges of all the gaps and optically-thick ringlets within the Cassini Division, using a comprehensive set of *Cassini* data from radio occultation (RSS) and stellar occultation (UVIS and VIMS) experiments carried out between 2005 and 2013. This is the third in a series of papers based on essentially the same data sets, using a standard data analysis protocol and an identical suite of orbit-fitting software. In Paper I (Nicholson et al., 2014a) we studied a single feature, the outer edge of the B ring, characterizing its complex response to the strong Mimas 2:1 Lindblad resonance and also identifying a rich set of normal modes that further perturb the edge. In Paper II (Nicholson et al., 2014b) we studied the innermost of Saturn's main rings, the C ring, with particular attention to the Colombo, Maxwell, Bond and Dawes gaps and their associated narrow ringlets. In addition to several edges that are perturbed by resonances with distant satellites and others that are freely

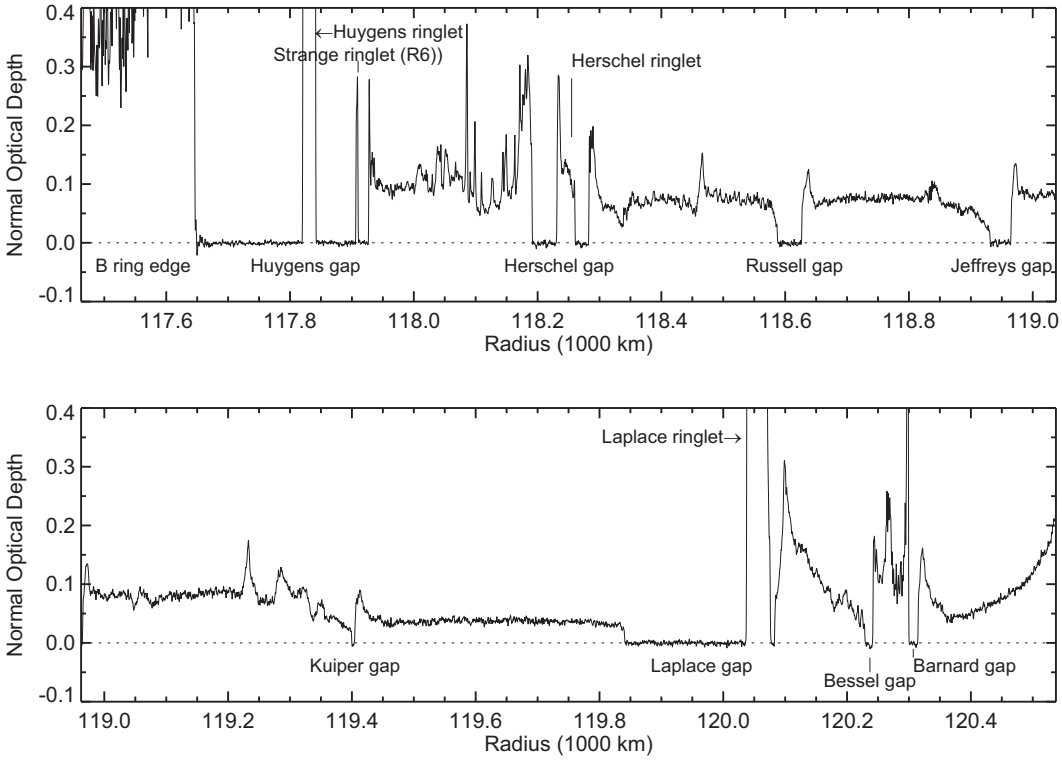

Fig. 1. Prominent ringlets and gaps in the Cassini Division, shown in an optical depth profile from the *Cassini* RSS egress occultation on rev 7.

precessing, we again identified numerous ringlet and gap edges with multiple normal modes. Paper IV (in preparation) will present an absolute radius scale for Saturn's rings, based on a comprehensive analysis of all available *Cassini* occultation data.

In Section 2 we briefly review the data sets used in this study, and summarize our measurement techniques and orbit-fitting procedure. Our main results are presented in Sections 3–6. In Section 3 we discuss the five simple gaps—those without dense embedded ringlets—which are found to have many aspects in common. The remaining three gaps are discussed individually in Sections 4–6: first, the broad Huygens gap containing the narrow, relatively opaque Huygens and Strange (or R6) ringlets; then the Herschel gap with its wider but less-dense ringlet; and finally the Laplace gap and its ringlet. (We do not discuss the three tenuous ringlets in the Cassini Division identified by Porco et al. (2005), and designated as R5, R8 and R9 by Colwell et al. (2009b), as these features are generally not visible in occultation profiles.) Section 7 summarizes the large number of normal modes identified in the Cassini Division, and attempts to extract some common aspects of these features, while in Section 8 we review the signatures of resonant forcing. Section 9 is devoted to the numerous features that appear to be well described—at least in part—as freely-precessing ellipses, exploring the radial trends in their eccentricities and apsidal precession rates and revisiting the three-body resonance model of Hedman et al. (2010). Our conclusions are summarized in Section 10.

Historically, there is some ambiguity concerning the true status of the Bessel and Barnard gaps. Nicholson et al. (1990) considered them to be parts of a single gap, and referred to the intervening material as the 1.994 R_S ringlet. In their review of ring structure, Colwell et al. (2009b) referred to this region as the R11 ringlet. But this supposed ringlet is almost as wide as the gap in which it resides and—unlike the Huygens and Laplace ringlets—-it is not substantially more opaque than the surrounding material. This situation led the IAU to redesignate this region as two discrete gaps. Similar arguments might suggest that the Herschel gap and ringlet should also be reclassified as a pair of nearby gaps—we will explore the evidence in more detail below. Although we have chosen to follow the official IAU-approved nomenclature here, it should be kept in mind that future studies might lead to a reclassification of some of these features.

2. Observations and ring orbit determination

For this study, we made use of an extensive set of high-SNR *Cassini* ring occultation observations from the RSS, VIMS, and UVIS instruments, restricting our attention to high-SNR events with spatial resolution of 1 km or better that include at least four fiducial circular features, used to establish an accurate absolute radius scale for each event. We excluded stellar occultations of binary stars, as well as several distant occultations where the large spacecraft range to the rings made it difficult to establish the event geometry with sufficient accuracy. In the end, our results incorporate over 10,000 individual ring measurements from 34 ingress or egress RSS radio occultations between May 2005 and January 2010, and 160 separate ingress or egress UVIS/VIMS occultations between July 2005 and September 2013. All of the data used in this study are publicly available from the NASA Planetary Data System Rings Node (http://http://pds-rings.seti.org/).

As described in detail in French et al. (2010), for each occultation we first constructed a geometry-independent "pseudo-intensity" profile to represent the normalized intensity $\mathcal{I}$ that would be measured when viewing the ring at normal incidence (i.e., $\sin B = 1$, where B is the incidence angle to the ring plane), assuming a classical many-particles-thick model for ring vertical structure:

$$\mathcal{I}(r') = e^{-\tau(r')}, \tag{1}$$

where τ is the normal optical depth and r' represents the nominal ring plane radius, uncorrected for trajectory errors or ring

inclination. To preserve the convention that increasing optical depth increases vertically on a plot, we invert the curve using the auxiliary function

$$\mathcal{F}(r') = 1 - \mathcal{I}(r') = 1 - e^{-\tau(r')}, \tag{2}$$

and fit a logistic model function to each sharp edge profile using

$$\mathcal{F}_m(r') = \mathcal{F}_0 + \frac{\mathcal{F}_1}{1 + e^{\pm(r'-r'_{1/2})/\sigma}}, \tag{3}$$

with the mid-point $r'_{1/2}$ of the feature defined to be where $\mathcal{F}_m(r') = \mathcal{F}_0 + \mathcal{F}_1/2$. For unresolved narrow ringlets, we fitted Gaussian, Lorentzian, or Voigt profiles, depending on the detailed shape of the feature. VIMS occultation observations include regular data gaps, associated with instrumental background measurements, and we took care to exclude individual VIMS ring events when data gaps affected the fitted ring location.

With a complete set of ring edge measurements in hand, we next established the ring plane radius scale and pole direction using a set of 67 quasi-circular, equatorial ring features with well-determined orbits and extensive high quality observations, with post-fit rms errors for each ring of < 0.22 km. (All of these features lie within the C ring, the B ring, and the Cassini Division; no sharp-edged circular features are present in the A ring that meet this stringent circularity condition.) We used a well-tested ring fitting code (RINGFIT) written in IDL that makes use of the NAIF SPICE toolkit (Acton, 1996) and the *Cassini* Navigation Team's reconstructed spacecraft trajectory kernels. Comparison of the orbit fit with those of a completely independent code (R. Jacobson, personal communication) give nearly identical results and formal errors: calculated ring orbital radii agree to better than 1 m. The *a priori* errors of the spacecraft ephemerides are of order 1 km; we fitted for the best along-track timing corrections for each ingress or egress occultation, which greatly reduced the post-fit rms errors. For each of a small number of occultations, we fitted an additional first-order correction term to compensate for remaining systematic residuals as a function of orbital radius, after the along-track timing correction had been applied. For several ring features with rather broad edges, we solved for a systematic radius correction—typically, of order a few hundred meters—to the RSS observations to compensate for the 1-km resolution of the diffraction-corrected data, compared to the higher spatial resolution of the VIMS and UVIS data used in this study.

The final geometric solution for the ephemeris corrections, orbital elements of the 67 circular features, and pole direction included 8245 data points, with a post-fit rms error per degree of freedom of just 0.14 km. We used a simple linear model to account for the precession of Saturn's pole, with a final solution (and formal errors) for the pole in J2000 coordinates of $\alpha_P = 40.579408 \pm 0.000062^\circ$, $\delta_P = 83.537218 \pm 0.000009^\circ$, $\dot{\alpha}_P = -0.034978 \pm 0.004062^\circ$ cy^{-1}, and $\dot{\delta}_P = -0.003191 \pm 0.000480^\circ$ cy^{-1}, for an epoch of 2008 January 1 12:00 UTC (JED 2454467.0). The corresponding position angle of the direction of polar precession is 129.02 ± 4.58° at a rate of 0.005068 ± 0.000525° cy^{-1}, or a 10% formal uncertainty in the pole precession rate based on this fit to *Cassini* data only. Formal errors in the semimajor axes of the circular features are quite small: of order 0.025 km; a more realistic estimate that accounts for possible systematic errors and incorporates historical occultation data from *Voyager* 1 and 2 (see French et al., 2010), the 28 Sgr stellar occultation of 1989 July 3 (French et al., 1993), and two HST occultations (Bosh, 1994; Elliot et al., 1993) is 0.25 km. Additional details of the adopted absolute radius scale and its uncertainty, and tighter constraints on the pole precession rate using all historical observations, will be provided in Paper IV of this series. All ring orbit fits presented in this paper are based on this geometric solution.

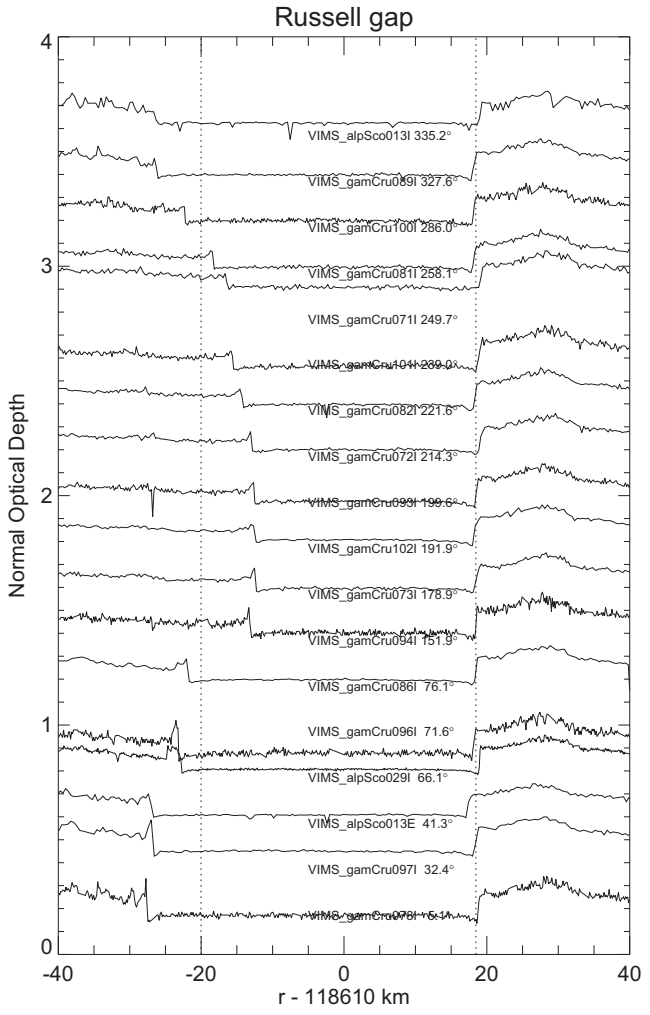

Fig. 2. Optical depth profiles for the Russell gap region, derived from selected VIMS stellar occultation profiles. The profiles are offset vertically by a constant amount, and arranged (and labeled) in order of increasing true anomaly of the eccentric inner edge. Vertical dotted lines indicate the mean radii of the inner and outer gap edges, based on our orbital fits.

Fig. **SM-1** [1] shows representative profiles of the 22 Cassini Division ringlet and gap edges that are the focus of the present study, from a single diffraction-corrected RSS occultation profile processed at 1 km resolution and sampled at 0.25 km.

Our least-squares orbit fitting program uses a common kinematic model for all ringlet and gap edges. We summarize the essential points below; additional details are provided in Paper II. The basic model is of a precessing, inclined keplerian ellipse, specified by:

$$r(\lambda, t) = \frac{a(1-e^2)}{1 + e\ \cos f}, \tag{4}$$

where the true anomaly $f = \lambda - \varpi = \lambda - \varpi_0 - \dot{\varpi}\,(t - t_0)$. Here, r, λ and t are the radius, inertial longitude and time (at ring intercept) of the observation, a and e are the ring edge's semimajor axis and eccentricity, ϖ and $\dot{\varpi}$ are its longitude of periapse and apsidal precession rate, and t_0 is the epoch of the fit. For most features, we assume that the ring edge lies in Saturn's mean equatorial plane. For inclined features, we include three additional parameters: i (inclination relative to the mean ring plane), Ω_0 (longitude of the

[1] Throughout this paper, we will refer to a number of figures that are accessible in the online Supplemental Material (SM).

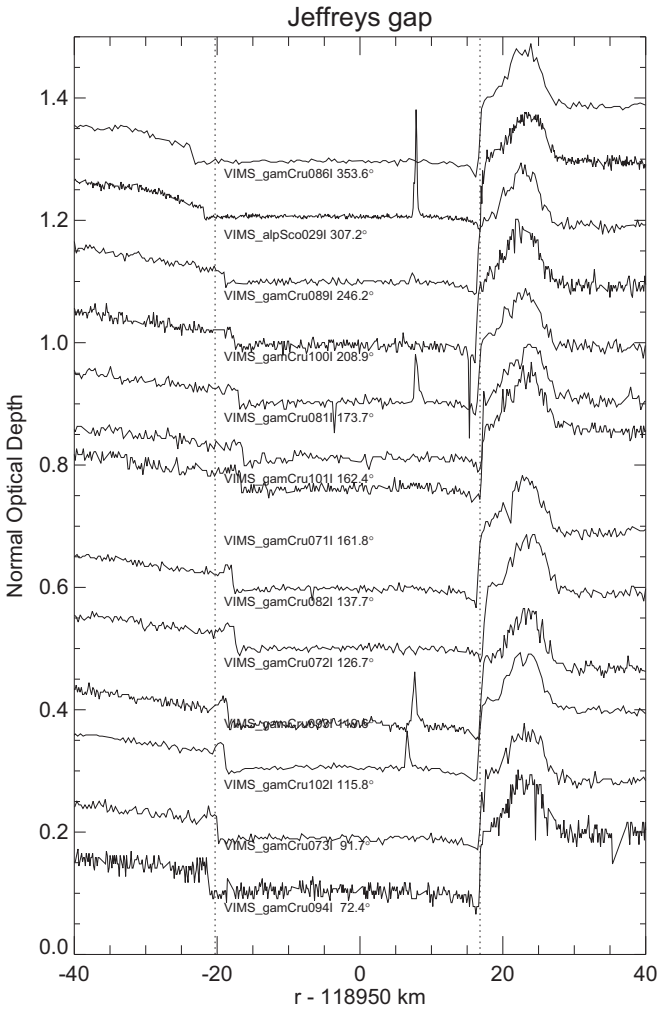

Fig. 3. Optical depth profiles for the Jeffreys gap region, derived from selected VIMS stellar occultation profiles. The profiles are offset vertically by a constant amount, and arranged (and labeled) in order of increasing true anomaly of the eccentric inner edge. Vertical dotted lines indicate the mean radii of the inner and outer gap edges, based on our orbital fits.

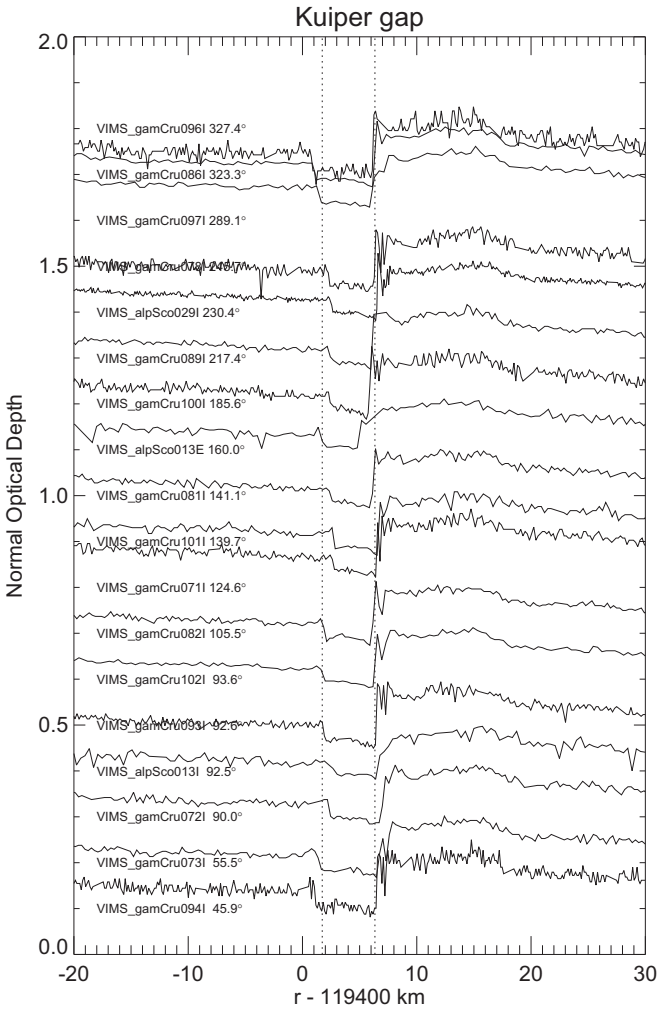

Fig. 4. Optical depth profiles for the Kuiper gap region, derived from selected VIMS stellar occultation profiles. The profiles are offset vertically by a constant amount, and arranged (and labeled) in order of increasing true anomaly of the eccentric inner edge. Vertical dotted lines indicate the mean radii of the inner and outer gap edges, based on our orbital fits.

ascending node) and $\dot{\Omega}$ (nodal regression rate), and compute the intercept point of the ray from the spacecraft to the Earth or star with the specified inclined ring plane. The zero-point for the inertial longitudes λ, ϖ_0 and Ω_0 (as well as δ_m and ϵ_m below) is the ascending node of Saturn's equator on the Earth's equator of J2000. All of our models use a common epoch of 2008 January 1, 12:00 UTC = JED 2454467.0, as in Papers I and II.

We also allow for other possible modes of radial distortion, each of which is specified by

$$\Delta r(\lambda, t) = -A_m \cos(m\theta), \tag{5}$$

where

$$\theta = \lambda - \Omega_p(t - t_0) - \delta_m \tag{6}$$

and m is the number of radial minima and maxima in the pattern. This expression describes free or normal modes of oscillation, where A_m is the mode's radial amplitude, δ_m is the longitude of one of the m radial minima, at $t = t_0$, and the pattern speed Ω_P is its angular rotation rate in inertial space, expected to be close to that of a Lindblad resonance located at the ring's semimajor axis (Borderies and Longaretti, 1987; French et al., 1991), as given by Eq. (7). We take as an *a priori* estimate

$$\Omega_p \simeq [(m-1)n + \dot{\varpi}_{sec}]/m, \tag{7}$$

where the mean motion n and apsidal precession rate $\dot{\varpi}_{sec}$—given by Eqs. (8) and (3), respectively, of Paper II—are evaluated at the semimajor axis of the edge. A positive value of m corresponds to an ILR-type (inner Lindblad resonance) normal mode, while a negative value of m corresponds to an OLR-type (outer Lindblad resonance) normal mode. We expect to find the former at the outer edges of ringlets (OER) or the inner edges of gaps (IEG), and the latter at the inner edges of ringlets (IER) or the outer edges of gaps (OEG). In either case, Ω_P is positive. For each mode, the additional fit parameters are A_m, Ω_P and δ_m. We note that an $m = 1$ ILR-type mode is equivalent, at least to first order in e, to a precessing keplerian ellipse with $A_1 = ae$, $\Omega_p = \dot{\varpi}_{sec}$ and $\delta_1 = \varpi_0$, the longitude of pericenter at $t = 0$. Below, we will find examples of ring features that contain more than one $m = 1$ mode simultaneously.

Equation (5) can also be used to describe radial perturbations forced by a Lindblad resonance with an external satellite, in which case the pattern speed, m-value, and phase are all determined by the satellite's orbital parameters, and Eq. (7) now serves to specify implicitly the exact resonance location $a_{\rm res}$.

Our model also includes terms describing possible vertical oscillations, using an equation of the form:

$$z(\lambda, t) = B_m \sin(m\theta), \tag{8}$$

Table 1
Orbital elements of five simple Casssini Division gaps.

ID	Feature	a(km)		m	ae (km)	ϖ_0(°)[a]	$\dot{\varpi}$ (°/d)	$\Delta\dot{\varpi}$ (°/d)	$\Delta a_{\dot{\varpi}}$ (km)
		N	rms (km)		$a \sin i$ (km)	Ω_0(°)	$\dot{\Omega}$(°/d)	$\Delta\dot{\Omega}$(°/d)	$\Delta a_{\dot{\Omega}}$ (km)
					A_m (km)	δ_m(°)	Ω_p(°/d)	$\Delta\Omega_p$(°/d)	Δa_p (km)
123	Russell Gap IEG	118589.92 ± 0.02		1	7.60 ± 0.03	236.73 ± 0.25	4.90922 ± 0.00028	0.00376	−25.40 ± 1.87
		157	0.25		[0.000][b]				
				2	0.23 ± 0.03	165.64 ± 4.19	376.94996 ± 0.00492	0.01784	−3.69 ± 1.02
				2_{Mimas}	0.51 ± 0.03	80.23 ± 1.89	381.98584 ± 0.00212	0.00234	−0.48 ± 0.44
				3	0.25 ± 0.03	92.19 ± 2.46	500.95134 ± 0.00286	0.01022	−1.60 ± 0.45
13	Russell Gap OEG	118628.40 ± 0.01		1	0.11 ± 0.01	73.68 ± 6.47	4.90829 ± 0.00644	0.00851	−57.61 ± 43.56
		160	0.09		[0.000][b]				
				2_{Mimas}	0.47 ± 0.01	78.01 ± 0.73	381.98525 ± 0.00080	0.00175	−0.36 ± 0.17
120	Jeffreys Gap IEG	118929.63 ± 0.02		1	3.26 ± 0.02	333.51 ± 0.47	4.85753 ± 0.00049	0.00201	−13.77 ± 3.35
		93	0.13	1	0.17 ± 0.01	292.09 ± 3.43	−4.82576 ± 0.00907	−0.00164	−11.37 ± 62.74
				2_{Mimas}	0.44 ± 0.02	75.98 ± 1.64	381.99151 ± 0.00181	0.00801	−1.67 ± 0.38
15	Jeffreys Gap OEG	118966.70 ± 0.01		1	0.08 ± 0.01	114.89 ± 11.68	4.80910 ± 0.01146	−0.04101	281.19 ± 78.54
		162	0.12		[0.000][b]				
				2_{Mimas}	0.37 ± 0.01	74.90 ± 1.18	381.98629 ± 0.00120	0.00279	−0.58 ± 0.25
119	Kuiper Gap IEG	119401.67 ± 0.01		1	0.93 ± 0.02	19.55 ± 1.32	4.79845 ± 0.00164	0.01125	−78.45 ± 11.45
		137	0.16	1	0.18 ± 0.01	226.51 ± 3.73	−4.78025 ± 0.01000	−0.02376	−167.37 ± 70.47
				2_{Mimas}	0.25 ± 0.02	79.87 ± 2.53	381.98534 ± 0.00298	0.00184	−0.39 ± 0.63
118	Kuiper Gap OEG	119406.30 ± 0.01		1	0.10 ± 0.02	220.24 ± 9.59	4.75654 ± 0.01096	−0.03000	209.20 ± 76.43
		157	0.13		[0.000][b]				
				2_{Mimas}	0.29 ± 0.02	79.03 ± 1.75	381.98449 ± 0.00188	0.00099	−0.21 ± 0.40
127	Bessel Gap IEG	120231.17 ± 0.04		1	1.78 ± 0.05	263.16 ± 1.76	4.68450 ± 0.00214	0.01438	−103.50 ± 15.40
		170	0.44		[0.000][b]				
				2_{Mimas}	0.29 ± 0.05	73.47 ± 5.32	381.97875 ± 0.00648	−0.00475	1.02 ± 1.39
				8	0.36 ± 0.05	10.70 ± 1.10	642.50158 ± 0.00133	0.00838	−1.04 ± 0.16
11	Bessel Gap OEG	120243.71 ± 0.02		1	0.64 ± 0.03	206.45 ± 2.58	4.68565 ± 0.00302	0.01727	−124.40 ± 21.74
		169	0.23		[0.000][b]				
				0	0.20 ± 0.03	350.38 ± 8.45	728.80164 ± 0.00982	−0.02595	2.87 ± 1.08
				2_{Mimas}	0.23 ± 0.03	76.05 ± 3.64	381.98984 ± 0.00410	0.00634	−1.36 ± 0.88
				−1	0.14 ± 0.03	302.43 ± 11.28	1462.27575 ± 0.01320	−0.04746	2.60 ± 0.72
10	Barnard Gap IEG	120303.69 ± 0.05		1	0.44 ± 0.06	200.07 ± 8.92	4.68212 ± 0.01267	0.02205	−159.22 ± 91.46
		161	0.43		[0.000][b]				
				2	0.61 ± 0.07	44.12 ± 3.25	368.82370 ± 0.00399	0.02142	−4.60 ± 0.86
				2_{Mimas}	0.25 ± 0.07	67.07 ± 7.39	381.99503 ± 0.00842	0.01153	−2.48 ± 1.81
				3	1.31 ± 0.06	108.47 ± 1.02	490.20424 ± 0.00150	0.02111	−3.42 ± 0.24
				4	1.64 ± 0.07	46.00 ± 0.57	550.89054 ± 0.00084	0.01698	−2.46 ± 0.12
				5	1.36 ± 0.06	27.61 ± 0.57	587.28565 ± 0.00088	−0.00216	0.29 ± 0.12
				6	0.59 ± 0.07	24.56 ± 1.01	611.58228 ± 0.00179	0.01830	−2.39 ± 0.23
				7	0.55 ± 0.06	46.93 ± 0.95	628.91493 ± 0.00130	0.01082	−1.37 ± 0.17
				8	0.30 ± 0.07	10.41 ± 1.59	641.92788 ± 0.00251	0.01868	−2.32 ± 0.31
				9	0.71 ± 0.07	8.38 ± 0.55	652.04071 ± 0.00065	0.01644	−2.01 ± 0.08
				10	0.42 ± 0.06	1.75 ± 0.98	660.13055 ± 0.00128	0.01422	−1.72 ± 0.15
				13	0.36 ± 0.06	26.84 ± 0.86	676.93190 ± 0.00124	0.00900	−1.06 ± 0.15
9	Barnard Gap OEG	120316.04 ± 0.01		1	0.23 ± 0.01	166.62 ± 3.44	4.66313 ± 0.00365	0.00477	−34.47 ± 26.40
		161	0.11		[0.000][b]				
				2_{Mimas}	0.22 ± 0.01	79.36 ± 1.83	381.98624 ± 0.00202	0.00274	−0.59 ± 0.43
				5	0.19 ± 0.01	58.97 ± 0.87	587.28403 ± 0.00103	0.08724	−11.84 ± 0.14

[a] The epoch is UTC 2008 January 1, 12:00:00.
[b] Quantities in square brackets were held fixed during orbit determination.

with

$$\theta = \lambda - \Omega_p(t - t_0) - \epsilon_m. \tag{9}$$

Again, this expression can accommodate either free or resonantly-forced modes, as appropriate. B_m and ϵ_m are the mode's vertical amplitude and phase, respectively, and in this case the pattern speed Ω_P is expected to be close to that of a vertical resonance located at the particles' orbit. We therefore take as an *a priori* estimate

$$\Omega_p \simeq [(m-1)n + \dot{\Omega}_{sec}]/m, \tag{10}$$

where $\dot{\Omega}_{sec}$ is the nodal regression rate as given by Eq. (4) of Paper II. In this expression, a positive value of m corresponds to an IVR-type normal mode, or to a forced perturbation at a satellite IVR. Note that an $m = 1$ mode is equivalent, to first order in i, to an inclined keplerian orbit with $B_m = a \sin i$, $\Omega_p = \dot{\Omega}_{sec}$ (the nodal regression rate) and $\epsilon_1 = \Omega_0$ (the longitude of the ascending node at $t = 0$).

Although in-plane perturbations manifest themselves directly as radial offsets with respect to a keplerian model, out-of-plane perturbations must be handled differently. In such cases, the apparent radial offset of the ring depends on the vertical displacement z, on the elevation B_* of the line of sight to the star (or to the Earth, in the case of a radio occultation) with respect to the ring plane, and on the longitude of observation λ. Denoting the inertial longitude of the line of sight to the star (or Earth) as λ_*, then the apparent radial displacement of the ring segment in the occultation profile is given by Nicholson et al. (1990) and Jerousek et al. (2011):

$$\Delta r = -\frac{z \cos\phi}{\tan B_*}, \tag{11}$$

where $\phi = \lambda - \lambda_*$. For vertically-perturbed rings, we add the above term to our ring model, where $z(\lambda, t)$ is given by Eq. (8).

The quality of the observational data, coupled with the extremely high accuracy of the fitted orbit models, makes it possible in some instances to fit for systematic radial distortions ae or A_m as small as $\simeq$ 0.1 km, and for inclinations $a \sin i$ as small as

≃ 0.05 km. To test for the robustness of these results, and to establish realistic uncertainties on the non-circularity and inclination of nominally circular and equatorial features, we have developed a pattern-scanning technique in which we specify a range of expected pattern speeds for a suspected radial distortion, inclination, or warp in the ring plane, and determine the amplitude and rms residuals of the best fitting distortion at each pattern speed. To be considered real, the overall best fit (lowest rms residuals) must be substantially better than all other fits, and the best-fitting pattern speed must be near to the theoretically expected value. For a distortion forced by an external satellite, an additional requirement is that the phase of the distortion be consistent with the mean longitude of the satellite. In cases where no such best fit exists, the typical amplitude of the fitted mode over the range of scanned pattern speed is used to estimate an upper limit to the mode in question.

In our orbit fits, we will make use of several quantities to compare the fitted and predicted apsidal and nodal precession rates. We let $\Delta\dot{\varpi}$ specify the difference between the fitted precession rate and the calculated value at the fitted semimajor axis, and define $\Delta a_{\dot{\varpi}} = \Delta\dot{\varpi}/(d\dot{\varpi}/da)$ as the corresponding amount by which the fitted semimajor axis would have to be shifted to match the observed value of $\dot{\varpi}$. Similarly, the corresponding difference between the fitted nodal rate and the calculated value is $\Delta\dot{\Omega}$, and $\Delta a_{\dot{\Omega}} = \Delta\dot{\Omega}/(d\dot{\Omega}/da)$ is the corresponding amount by which the fitted semimajor axis would have to be shifted to match the observed value of $\dot{\Omega}$. For normal modes, we define $\Delta\Omega_p$ to be the difference between the fitted value of Ω_P and that predicted by Eq. (7). The corresponding radial offset is given by $\Delta a_p = \Delta\Omega_p/(d\Omega_p/da)$.

3. Simple gaps in the Cassini Division

We begin our survey with the five narrow gaps in the Cassini Division that do *not* contain dense ringlets: the Russell, Jeffreys, Kuiper, Bessel and Barnard gaps. In Figs. 2–5 we show sample radial profiles of each of these features, selected from the highest-quality VIMS occultation data. The individual profiles in each figure are sorted by the true anomaly f of the more eccentric edge, so as to illustrate any nonzero eccentricity. As a general observation, we note first that at 300–500 m resolution, all 10 edges appear quite sharp. However, the outer edges of these simple gaps usually show greater contrast and are thus more easily measured than are the inner edges. The only exception to this generalization is the Barnard gap, whose inner edge is much more prominent. A second feature common to most of these gaps is a broad bump in optical depth located between 5 and 15 km exterior to the outer gap edge. This bump is most prominent for the Jeffreys gap, but absent for the Bessel gap. (A similar feature is seen exterior to the Laplace gap in Fig. 22 below.)

Our own fits to the edges of these five gaps largely corroborate the findings of Hedman et al. (2010) and French et al. (2010). In particular, we confirm that the *outer* edges of the Russell, Jeffreys, Kuiper and Barnard gaps are circular to within ~0.25 km; these are in fact the only features in the Cassini Division that have survived in our list of circular fiducial features used to define the ring plane radius scale and pole direction.[2] For the *inner* edges of these gaps and the *outer* edge of the Bessel gap, precessing keplerian ellipse (i.e., $m = 1$) models provide generally satisfactory fits, although in almost all cases we find evidence for additional normal modes. The

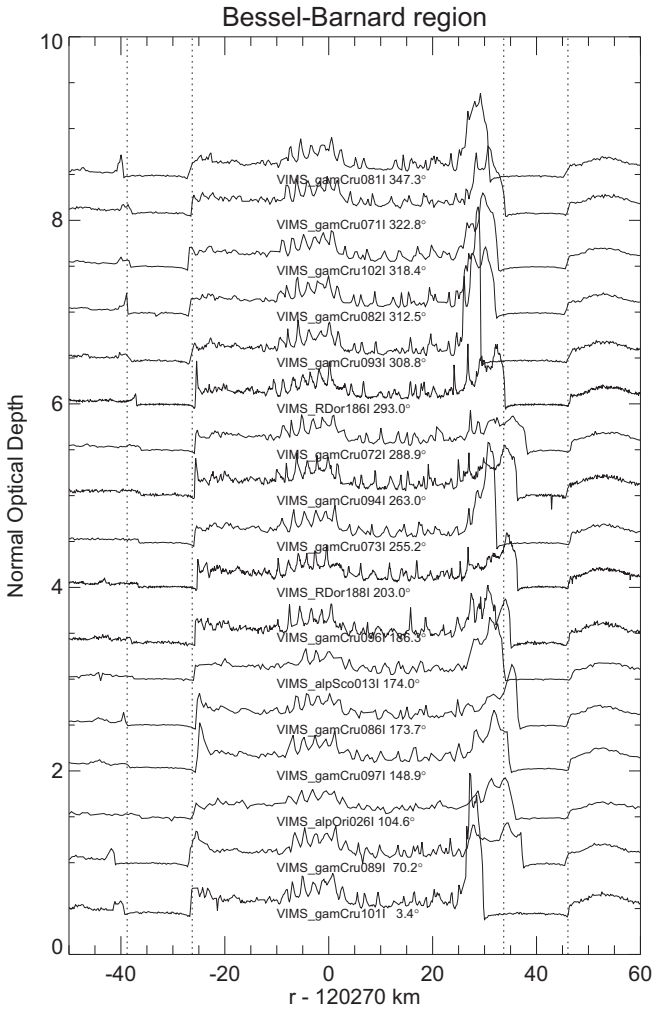

Fig. 5. Optical depth profiles for the region containing the Bessel (left) and Barnard (right) gaps, derived from selected VIMS stellar occultation profiles. The profiles are offset vertically by a constant amount, and arranged (and labeled) in order of increasing true anomaly of the eccentric inner edge of the Barnard gap. Vertical dotted lines indicate the mean radii of the gap edges, based on our orbital fits.

inner edge of the Barnard gap is again unusual, inasmuch as it has a very small eccentricity and is instead dominated by no less than three normal modes of comparable strength with $m = 3$, 4 and 5.

In the discussion below, the reader is referred to Table 1, which contains our best-fitting orbital elements for all of the simple Cassini Division gap edges. For each measured edge, we list, for reference, the feature ID number (an extension of the numbering scheme given in French et al., 1993), the mean radius a, the number of data fitted N and the post-fit rms residual. For each component of the fit, we also list the value of m; the amplitude ae, $a \sin i$ or A_m; the phase ϖ_0, Ω_0 or δ_m; the pattern speed, $\dot{\varpi}$, $\dot{\Omega}$ or Ω_P; the departures of these rates from their predicted values; and the corresponding offsets in semimajor axis, $\Delta a_{\dot{\varpi}}$, $\Delta a_{\dot{\Omega}}$, and Δa_p, as defined previously.

3.1. The Russell gap

The Russell gap may be considered the type example of a simple Cassini Division gap, with an eccentric inner edge ($ae = 7.6$ km) and a circular outer edge ($ae < 0.1$ km). The only other significant perturbations are $m = 2$ modes, attributed to the effect of the Mimas 2:1 ILR, with amplitudes of ~0.50 km. (These so-called Mimas modes appear on almost all sharp edges in the Cassini

[2] As discussed further in Section 8.1, almost all of the sharp edges in the Cassini Division also show an $m = 2$ signature due to forcing by the very strong Mimas 2:1 ILR at the outer edge of the B ring. But for the purpose of selecting reference features we will generally ignore this additional perturbation, although it is of course included in our fits and in the tables of fit parameters.

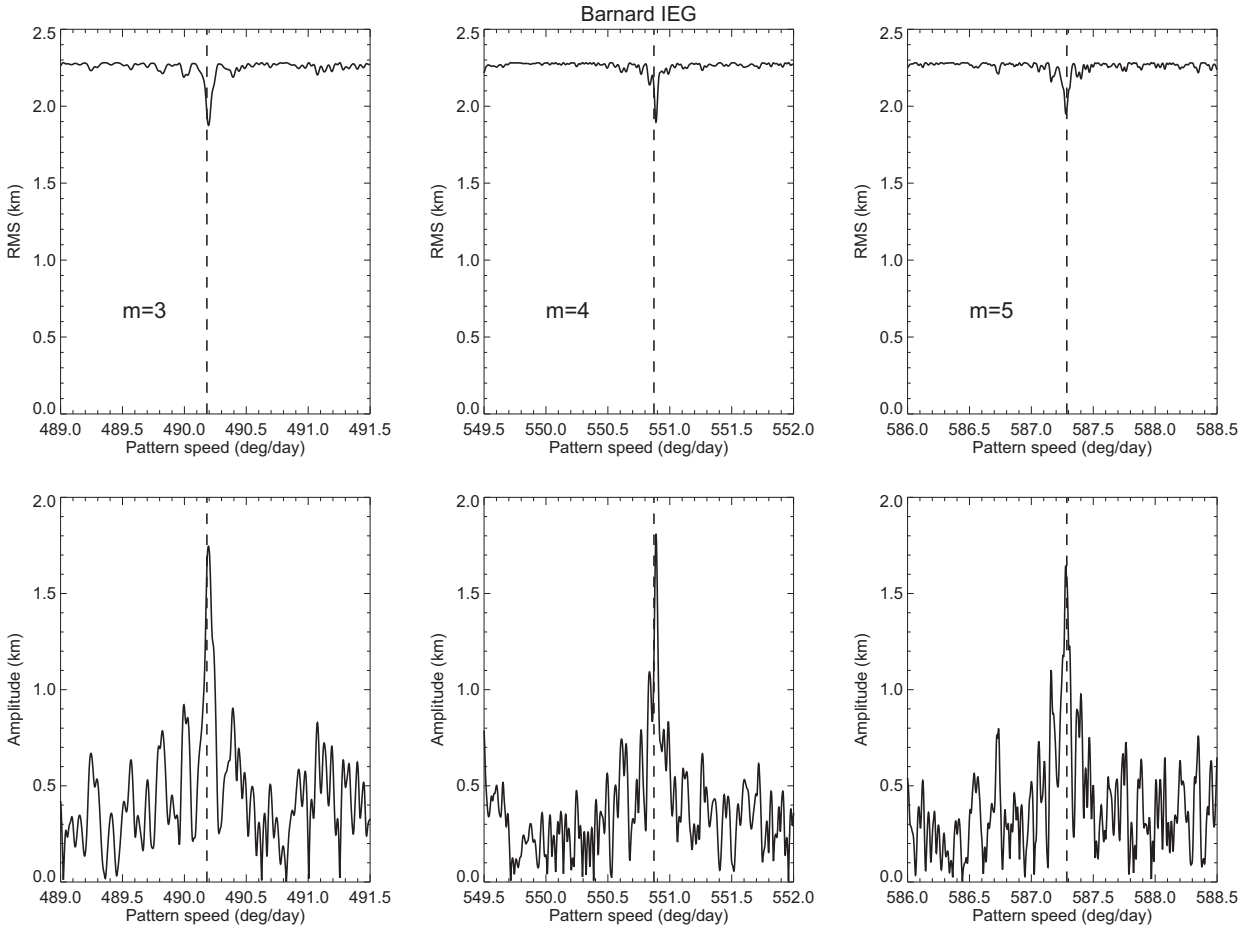

Fig. 6. Barnard IEG (inner edge of gap) normal mode scans for $m = 3$, 4 and 5. The vertical dashed lines indicate the predicted pattern speeds for the three modes.

Division, and are discussed as a group in Section 8.) There are very weak $m = 2$ and 3 ILR-type modes on the inner edge, but no detectable inclination is seen on either edge ($a \sin i < 0.1$ km). Post-fit rms residuals are 0.25 and 0.09 km for inner and outer edges, respectively. The mean width of the Russell gap is 38.5 km, and a series of radial profiles is shown in Fig. 2.

3.2. The Jeffreys gap

A similar story holds for the Jeffreys gap, which sports a somewhat less eccentric inner edge ($ae = 3.4$ km) and a circular outer edge. The only other significant perturbations are the $m = 2$ Mimas modes, with slightly smaller amplitudes of ~0.35 km, owing to their greater radial separation from the resonance location. Again, no detectable inclination is seen on either edge. Post-fit rms residuals are 0.14 and 0.12 km for the inner and outer edges, respectively. The mean width of the Jeffreys gap is 37.1 km, almost the same as that of the Russell gap, and a series of radial profiles is shown in Fig. 3. The sharp peaks in four of the profiles in this plot are due to a very narrow, discontinuous or clumpy ringlet at a radius of ~118, 958 km. We have not attempted to measure this feature, designated as R8, which is also visible in *Cassini* images (Colwell et al., 2009b).

3.3. The Kuiper gap

The Kuiper gap is exceptionally narrow, with a width that averages only 4.6 km. Indeed, it is only barely resolved in some *Cassini* occultations, and not at all in ground-based occultations of bright stars such as 28 Sgr (French et al., 1993; Nicholson et al., 2000). But in all other respects it resembles the much wider Russell and Jeffreys gaps, with an eccentric inner edge ($ae = 0.9$ km) and a circular outer edge ($ae < 0.1$ km). The usual Mimas modes have amplitudes of ~0.27 km. There is a possible inclination on the inner edge with $a \sin i = 0.18$ km, but no other detectable normal modes. Post-fit rms residuals are 0.16 and 0.13 km for inner and outer edges, respectively. A series of radial profiles is shown in Fig. 4.

3.4. The Bessel gap

In most respects the Bessel gap is similar to the Russell, Jeffreys and Kuiper gaps, with an eccentric inner edge ($ae = 1.8$ km). However, in this case the outer edge is not quite circular, with an $m = 1$ amplitude of $ae = 0.6$ km. Note that the pericenters of the two edges are misaligned by 57°, although they may well be precessing at the same rate, given the fit uncertainties (see Table 1). The only other significant perturbations are the $m = 2$ Mimas modes, with amplitudes of ~0.25 km, a weak $m = 8$ ILR-type mode on the inner edge, and two even weaker OLR-type modes ($m = 0$ and $m = -8$) on the outer edge. Again, no detectable inclination is seen on either edge. Post-fit rms residuals are 0.44 and 0.23 km for inner and outer edges, respectively. The mean width of the Bessel gap is 12.5 km, and a series of radial profiles covering both Bessel and Barnard gaps is shown in Fig. 5.

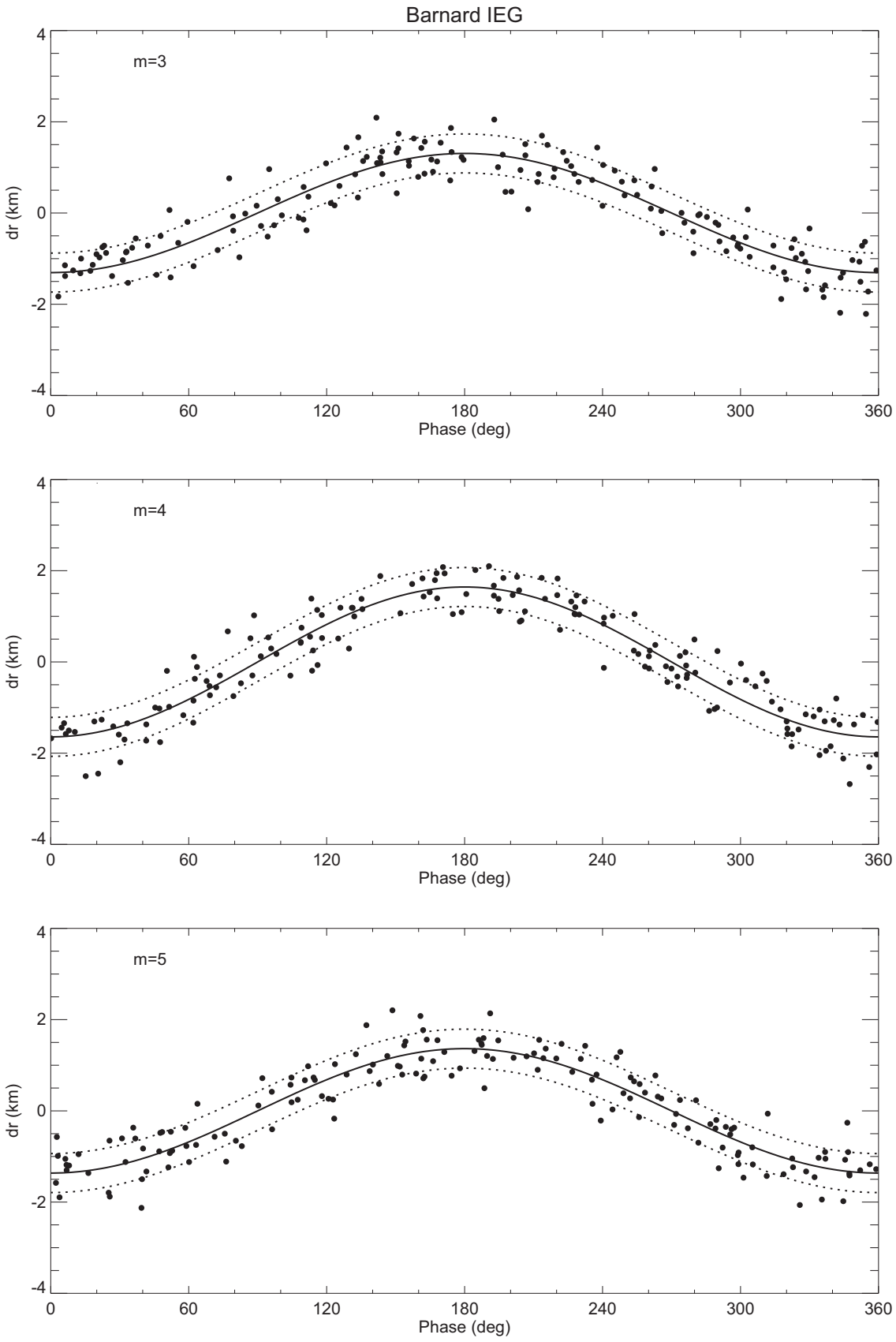

Fig. 7. Residuals of Barnard IEG vs phase for $m = 3, 4$ and 5. The fitted amplitudes are 1.31, 1.64, and 1.36 km, respectively. For each plot, all other fitted modes have been subtracted from the measurements.

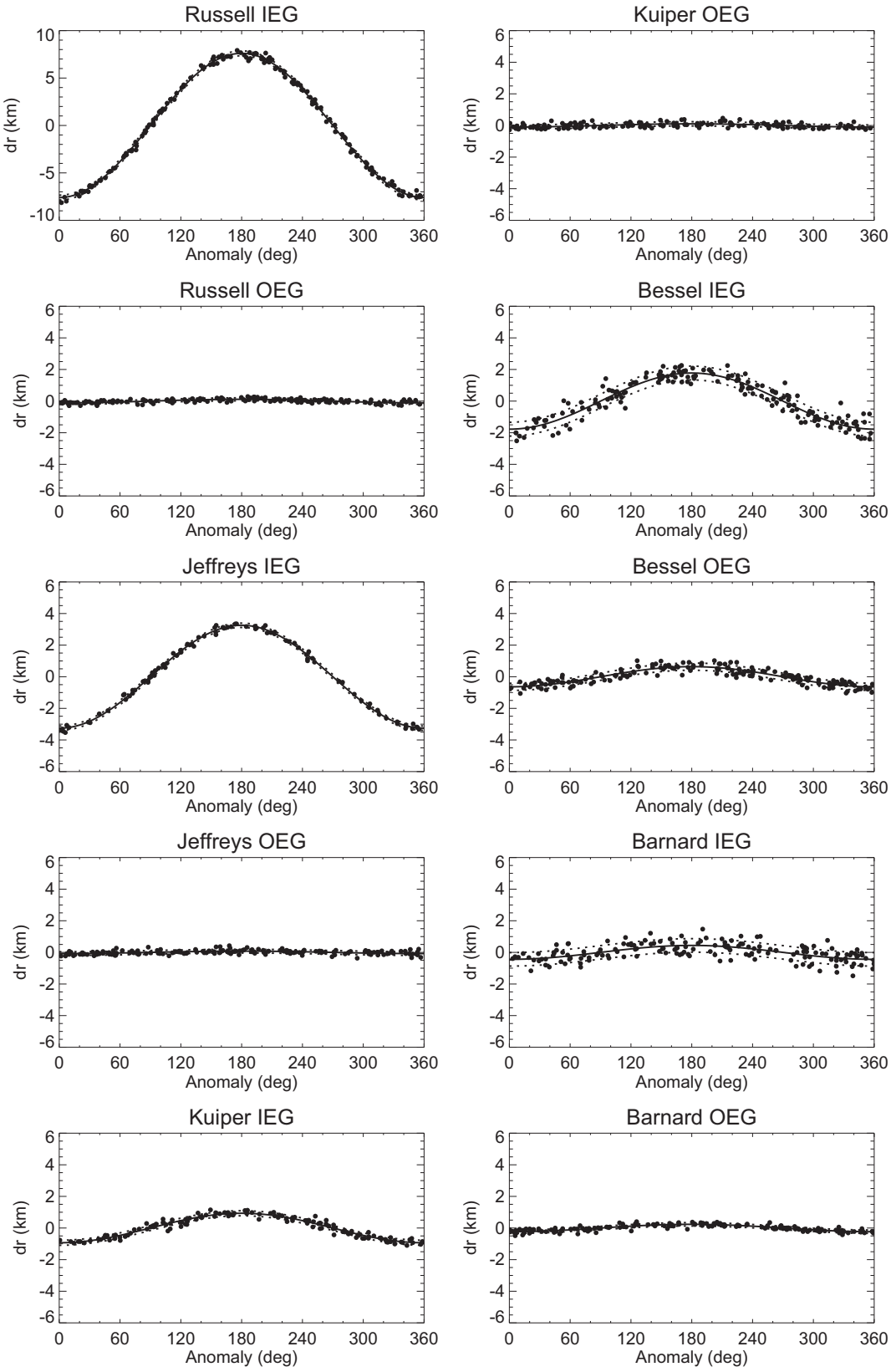

Fig. 8. A gallery of $m = 1$ models for the five simple gaps in the Cassini Division and their residuals, plotted vs true anomaly. Other normal modes, when present, have been removed. Fitted amplitudes are listed in Table 1.

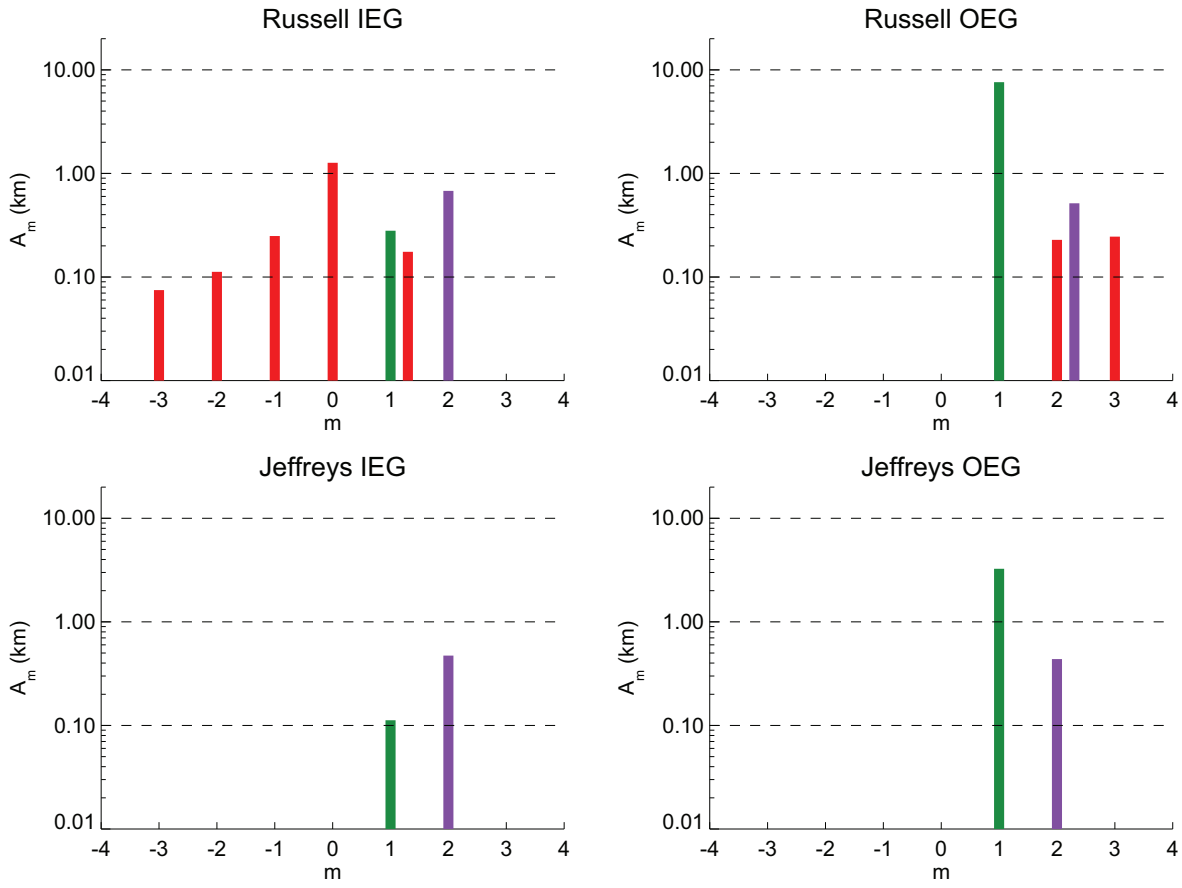

Fig. 9. Normal modes for the Russell and Jeffreys gaps. Inner edges of gaps (IEG) are shown on the left, and outer edges of gaps (OEG) on the right. Modes are coded by color: free eccentric modes ($m = 1$) are green, other free modes are red, and modes forced by an external satellite (in this case, the $m = 2$ mode forced by Mimas) are violet. (For interpretation of the references to color in this figure legend, the reader is referred to the web version of this article.)

3.5. The Barnard gap

As already noted above, the Barnard gap differs in several ways from its siblings. Its prominent inner edge shows no less than 11 distinct normal modes, with $1 \leq m \leq 13$, of which the $m = 1$ mode has the nearly smallest amplitude! The largest are the $m = 3$, 4 and 5 ILR-type modes, with amplitudes of $1.3 - -1.7$ km. The outer edge, however, is almost circular, a characteristic it shares with most of the other simple gaps.

In Fig. 6 we present normal mode scans of the inner gap edge for $m = 3$, 4 and 5. Each of these scans begins with a common reference fit that includes only the $m = 1$ mode, and whose rms residual is 2.3 km; in each case the rms residual is reduced to ~1.9 km. The final least-squares fit, with all 11 normal modes included, has a post-fit rms residual of 0.43 km (see Table 1). Fig. 7 shows the pattern of residuals as a function of longitude for each of the $m = 3$, 4 and 5 modes, after removing the contributions from all other modes.

By comparison with the inner edge, the outer edge of the Barnard gap is relatively simple: we find small $m = 1$ and 5 ILR-type modes, with amplitudes of ~0.2 km, and a Mimas signature of comparable size. Post-fit rms residuals are a very small 0.11 km. The mean width of the Barnard gap is 12.4 km, essentially identical to that of the Bessel gap.

Although the sheer number of modes detected on the inner edge of the Barnard gap is unprecedented, the presence of the $m = 5$ mode on both edges is very likely due to the proximity of the Prometheus 5:4 ILR at 120304.0 km. Indeed, the best-fit pattern speeds closely match the mean motion of Prometheus, as expected for a first-order Lindblad resonance. We will examine the agreement of the amplitude and phase with that predicted for this resonance in Section 8.2.

3.6. Summary

In Fig. 8 we present a gallery of our elliptical model fits to the 10 simple gap edges, displayed where feasible at a common vertical scale so as to facilitate comparisons. In each case we plot the measured radius variations vs true anomaly, after removal of any other significant perturbations with $m \neq 1$. Note the near-circularity of the outer edges of the Russell, Jeffreys, Kuiper and Barnard gaps, which we use as reference features in our reconstruction of the geometry for each occultation. None of these gap edges has a significant inclination ($a \sin i < 0.2$ km). We defer additional discussion of the eccentricities and precession rates to Section 9 below.

Figs. 9 and 10 summarize the normal modes detected on the edges of the Russell, Jeffreys, Bessel and Barnard gaps, based on the fits reported in Table 1. We discuss the normal mode characteristics as a group in Section 7.

We return now to the issue raised in Section 1 as to whether the Bessel and Barnard gaps are better considered as two nearby simple gaps, or as a single complex gap containing a rather broad, isolated ringlet. In favor of the former hypothesis, we observe that (1) the putative 1.994 R_S ringlet is hardly more dense than the surrounding regions (unlike the Huygens and Laplace ringlets, or the Titan and Maxwell ringlets in the C ring); and (2) the pericenters of its inner and outer edges differ by $38 \pm 22°$, unlike most other

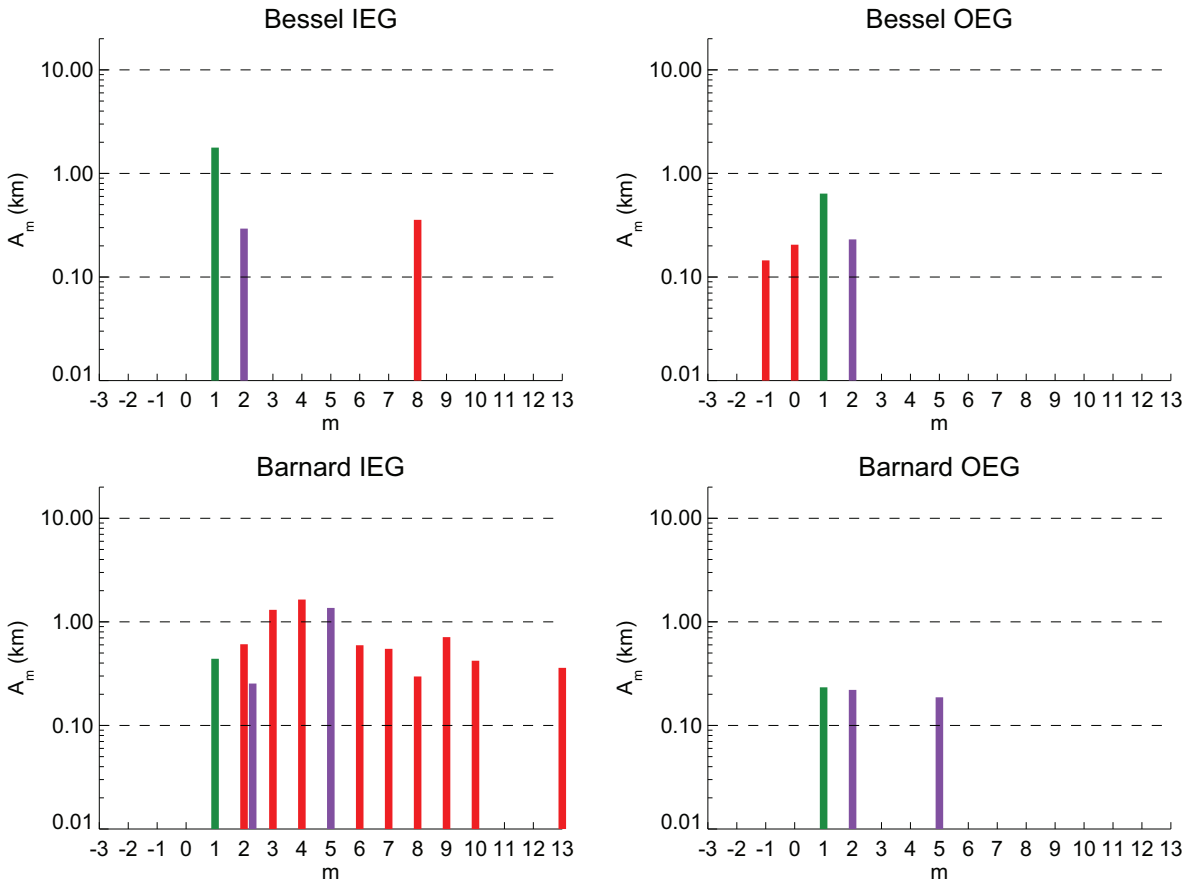

Fig. 10. Normal modes for the Bessel and Barnard gaps. Modes are coded by color: free eccentric modes ($m = 1$) are green, other free modes are red, and modes forced by an external satellite are violet (Mimas, for $m = 2$, and the Prometheus 5:4 ILR for the $m = 5$ modes for the Barnard IEG and OEG). (For interpretation of the references to color in this figure legend, the reader is referred to the web version of this article.)

eccentric ringlets. In favor of the latter we note that (1) the outer edge of the Bessel gap lacks the bump in optical depth seen exterior to most other simple gaps; (2) this same edge is definitely eccentric, unlike all other outer edges of simple gaps but like most narrow ringlet edges; and (3) the inner edge of the Barnard gap is unusually well-defined. None of these items of evidence seems to be definitive, however, and indeed there is no agreed-upon definition of a ringlet in this context.

4. The Huygens gap

We turn next to what we may refer to as complex gaps: i.e., those containing one or more isolated ringlets. This group includes the Huygens, Herschel and Laplace gaps. We begin with the Huygens gap, which is bordered on its inner edge by the outer edge of the B ring. The latter was discussed in detail by Spitale and Porco (2010) and Nicholson et al. (2014a), and we will not repeat their results here. In summary, the shape of this highly-noncircular feature is dominated by perturbations due to the Mimas 2:1 ILR, one of the strongest satellite resonances in Saturn's rings, but the edge also exhibits normal modes with $m = 1$, 2, 3, 4 and 5. The forced and free $m = 2$ components are each ~35 km in amplitude and beat against one another with a period of 5.4 years, so that the instantaneous amplitude of the $m = 2$ signature varies from as little as a few km to as much as 70 km (Nicholson et al., 2014a). The amplitudes of the other modes range from 6 to 20 km, with $m = 1$ being the largest.

The Huygens gap is 361 km wide and is host to two narrow and relatively opaque ringlets, known as the Huygens and (informally) Strange ringlets. (The latter was designated R6 by Colwell et al., 2009b, but has not yet been given an official designation by the IAU.) We will first discuss the ringlets, and then the outer edge of the gap. Perhaps not surprisingly, our fits show that the entire Huygens gap region is subject to strong direct perturbations from the Mimas 2:1 resonance, probably combined with indirect perturbations from the large and variable $m = 2$ distortion of the B ring edge.

4.1. Huygens ringlet

In Fig. 11 we present a series of optical depth profiles of the Huygens ringlet, arranged by increasing true anomaly. Both edges are quite sharp, and the optical depth profile is U-shaped, with a broad minimum near the ringlet's centerline. Its mean width is ~18 km. As previously reported by Porco (1983) and Turtle et al. (1991), on the basis of *Voyager* observations, and confirmed by Hedman et al. (2010), this ringlet is well-described to first order as a precessing keplerian ellipse, similar to the Titan and Maxwell ringlets in the C ring, or the uranian ϵ ring. In Fig. 12, we plot the radii of both edges of the Huygens ringlet as a function of true anomaly f. The pericenters of inner and outer edges are aligned to within 5°, and their independently-fitted precession rates are equal to within the fit uncertainties. Unlike all other known eccentric rings, however, the edges of the Huygens ringlet have almost identical eccentricities. As a result, the width of the ringlet is essentially independent of f. The fitted amplitudes are ~28.3 km and differ by less than 1 km.

Table 2
Huygens Ringlet, Huygens Gap, and Strange Ringlet (R6) orbital elements.

ID	Feature	a(km)	m	ae(km)	ϖ_0(°)[a]	$\dot{\varpi}$ (°/d)	$\Delta\dot{\varpi}$ (°/d)	$\Delta a_{\dot{\varpi}}$ (km)
		N rms (km)		$a \sin i$ (km)	Ω_0(°)	$\dot{\Omega}$(°/d)	$\Delta\dot{\Omega}$(°/d)	$\Delta a_{\dot{\Omega}}$ (km)
				A_m (km)	δ_m(°)	Ω_p(°/d)	$\Delta\Omega_p$(°/d)	Δa_p (km)
54	Huygens Ringlet IER	117805.55 ± 0.11	1	27.81 ± 0.16	137.53 ± 0.36	5.02872 ± 0.00039	0.00536	−35.15 ± 2.56
		178 1.30	1	0.59 ± 0.10	115.57 ± 8.12	−4.98852 ± 0.01787	0.00170	11.27 ± 118.31
			2_{Mimas}	2.09 ± 0.16	81.56 ± 2.39	381.98744 ± 0.00250	0.00394	−0.80 ± 0.51
			−10	0.74 ± 0.17	14.73 ± 1.23	831.59967 ± 0.00132	−0.03113	2.93 ± 0.12
			−5	0.85 ± 0.16	43.95 ± 2.38	906.74404 ± 0.00252	−0.03291	2.84 ± 0.22
			−4	1.85 ± 0.17	32.20 ± 1.32	944.31186 ± 0.00135	−0.03818	3.17 ± 0.11
			−3	1.20 ± 0.17	84.52 ± 2.73	1006.92419 ± 0.00291	−0.04765	3.71 ± 0.23
			−2	1.12 ± 0.16	168.38 ± 4.40	1132.15800 ± 0.00515	−0.05744	3.98 ± 0.36
53	Huygens Ringlet OER	117823.65 ± 0.12	1	28.03 ± 0.17	141.77 ± 0.38	5.02587 ± 0.00042	0.00528	−34.60 ± 2.78
		183 1.50	1	0.58 ± 0.11	96.86 ± 8.97	−4.97462 ± 0.01895	0.01288	85.31 ± 125.53
			2	1.54 ± 0.17	105.43 ± 3.62	380.68870 ± 0.00393	0.02379	−4.84 ± 0.80
			2_{Mimas}	1.84 ± 0.17	71.33 ± 2.93	381.98878 ± 0.00313	0.00528	−1.07 ± 0.64
			5	0.71 ± 0.17	26.40 ± 3.00	606.07903 ± 0.00319	0.02733	−3.52 ± 0.41
53	Huygens Ringlet OER	117823.68 ± 0.08	1	29.72 ± 0.83	135.22 ± 1.16	5.03028 ± 0.00096	0.00969	−63.51 ± 6.27
		183 0.97	1	0.51 ± 0.07	99.91 ± 6.94	−5.01183 ± 0.01649	−0.02435	−161.32 ± 109.28
			1	3.89 ± 0.83	247.39 ± 9.03	5.08186 ± 0.00698	0.06160	−403.89 ± 45.73
			2	2.02 ± 0.12	101.38 ± 1.85	380.69456 ± 0.00197	0.02981	−6.07 ± 0.40
			2_{Mimas}	1.78 ± 0.11	75.55 ± 2.04	381.98465 ± 0.00226	0.00115	−0.23 ± 0.46
			5	0.55 ± 0.11	23.13 ± 2.57	606.07959 ± 0.00281	0.02814	−3.62 ± 0.36
560	Strange Ringlet (R6) IER	117907.04 ± 0.15	1	7.63 ± 0.21	153.21 ± 1.73	5.00570 ± 0.00184	−0.00219	14.43 ± 12.12
		167 1.63	1	7.44 ± 0.16	117.20 ± 0.91	−4.97620 ± 0.00166	−0.00128	−8.49 ± 11.05
			0	2.42 ± 0.20	9.73 ± 5.24	750.48932 ± 0.00555	−0.00685	0.72 ± 0.58
			2	3.75 ± 0.21	105.79 ± 1.67	380.25154 ± 0.00179	−0.00411	0.84 ± 0.37
			2_{Mimas}	1.29 ± 0.20	75.92 ± 5.16	381.97024 ± 0.00576	−0.01326	2.70 ± 1.17
			3	2.49 ± 0.21	37.53 ± 1.62	505.33539 ± 0.00177	−0.00295	0.45 ± 0.27
			5	1.06 ± 0.20	29.00 ± 2.57	605.39489 ± 0.00258	−0.00961	1.24 ± 0.33
100	Strange Ringlet (R6) COR	117907.73 ± 0.14	1	7.53 ± 0.20	154.38 ± 1.74	5.00549 ± 0.00185	−0.00230	15.12 ± 12.19
		179 1.60	1	7.15 ± 0.16	117.70 ± 0.97	−4.97991 ± 0.00198	−0.00509	−33.84 ± 13.20
			0	2.47 ± 0.20	22.66 ± 5.22	750.47404 ± 0.00550	−0.01557	1.64 ± 0.58
			2	3.79 ± 0.20	104.82 ± 1.75	380.25159 ± 0.00184	−0.00067	0.14 ± 0.38
			2_{Mimas}	1.52 ± 0.20	73.00 ± 4.44	381.97443 ± 0.00493	−0.00907	1.85 ± 1.01
			3	2.33 ± 0.21	31.24 ± 1.71	505.33606 ± 0.00181	0.00219	−0.34 ± 0.28
			5	1.05 ± 0.20	26.78 ± 2.46	605.39733 ± 0.00272	−0.00181	0.23 ± 0.35
			−3	0.86 ± 0.20	15.26 ± 5.50	1005.65070 ± 0.00564	−0.00957	0.75 ± 0.44
			−2	0.96 ± 0.21	46.53 ± 6.56	1130.72302 ± 0.00651	−0.01885	1.31 ± 0.45
			−1	0.59 ± 0.21	2.39 ± 22.71	1505.95636 ± 0.02229	−0.03032	1.58 ± 1.16
561	Strange Ringlet (R6) OER	117908.77 ± 0.17	1	7.40 ± 0.24	153.83 ± 2.10	5.00735 ± 0.00220	−0.00028	1.86 ± 14.48
		180 1.99	1	7.39 ± 0.17	120.60 ± 0.99	−4.97938 ± 0.00187	−0.00472	−31.38 ± 12.44
			0	2.56 ± 0.24	19.83 ± 5.94	750.47956 ± 0.00607	−0.00019	0.02 ± 0.64
			2	4.13 ± 0.23	106.14 ± 1.83	380.25204 ± 0.00186	0.00486	−0.99 ± 0.38
			2_{Mimas}	1.55 ± 0.24	77.43 ± 4.85	381.96666 ± 0.00512	−0.01684	3.44 ± 1.04
			3	2.60 ± 0.25	33.24 ± 1.80	505.33449 ± 0.00182	0.00736	−1.13 ± 0.28
			−1	1.14 ± 0.24	352.19 ± 13.97	1505.96783 ± 0.01326	0.00102	−0.05 ± 0.69
20	Huygens Gap OEG	117930.90 ± 0.04	1	2.20 ± 0.06	248.91 ± 1.55	5.03383 ± 0.00174	0.02956	−194.63 ± 11.46
		176 0.45	1	0.44 ± 0.03	245.71 ± 4.15	−4.98428 ± 0.00947	−0.01295	−86.15 ± 62.98
			0	1.82 ± 0.05	143.90 ± 1.86	750.25152 ± 0.00226	−0.01801	1.90 ± 0.24
			2_{Mimas}	1.34 ± 0.05	76.17 ± 1.27	381.98394 ± 0.00148	0.00044	−0.09 ± 0.30
			−4	0.35 ± 0.06	45.35 ± 2.42	942.82225 ± 0.00269	−0.01859	1.55 ± 0.22
			−3	0.40 ± 0.06	84.75 ± 2.84	1005.34998 ± 0.00299	−0.01332	1.04 ± 0.23
			−1	0.82 ± 0.05	66.96 ± 4.26	1505.51227 ± 0.00470	−0.03071	1.60 ± 0.25

[a] The epoch is UTC 2008 January 1, 12:00:00.

As noted by Turtle et al. (1991), however, a purely elliptical model provides a relatively poor fit to the Huygens ringlet. Further investigation reveals, as anticipated, a substantial $m = 2$ signature attributable to the Mimas resonance, with an amplitude of 1.9 km on the inner edge and 1.7 km on the outer edge. In addition, we find OLR-type normal modes with $m = -2, -3, -4, -5$, and -10 on the inner edge, and ILR-type modes with $m = 2$ and 5 on the outer edge. These modes range in amplitude from 0.7 to 1.8 km. (The forced and free $m = 2$ modes on the outer edge are readily distinguished by their different pattern speeds of 381.985 and 380.695° d^{-1}, respectively)

We also see evidence for a possible secondary $m = 1$ mode for the Huygens OER, as indicated in the normal mode scan shown in Fig. 13. The corresponding post-fit rms is reduced from 1.50 to 0.97 km by the inclusion of this second mode, which has an amplitude of 3.9 km and an apse rate $\dot{\varpi} = 5.082°\,d^{-1}$, considerably faster than that of the primary $m = 1$ mode. We speculate that this second $m = 1$ mode may be forced by the B ring itself, which has a nearly identical fitted $m = 1$ pattern speed of $5.0835 \pm 0.0019°\,d^{-1}$ (Nicholson et al., 2014a), although the exact forcing mechanism remains to be explored quantitatively. Fit parameters are listed in Table 2, while Fig. 14 shows the forced $m = 2$ modes on the inner and outer edges.

Finally, and equally surprisingly, we find evidence that the Huygens ringlet has a small but significant inclination. Fits to both edges yield vertical amplitudes, $a \sin i \simeq 0.6$ km, with very similar nodal longitudes at epoch. The fitted nodal regression rates are also equal to within their uncertainties, at $-4.99 \pm 0.02°\,d^{-1}$, and very close to the rate predicted using Saturn's zonal gravity harmonics. Fig. 15 shows node rate scans that demonstrate the statistical significance of the fitted inclinations

Table 3
Orbital elements of Herschel Ringlet and Gap.

ID	Feature	a(km)		m	ae(km)	ϖ_0(°)[a]	$\dot{\varpi}$ (°/d)	$\Delta\dot{\varpi}$ (°/d)	$\Delta a_{\dot{\varpi}}$ (km)
		N	rms (km)		$a \sin i$ (km) A_m (km)	Ω_0(°) δ_m(°)	$\dot{\Omega}$(°/d) Ω_p(°/d)	$\Delta\dot{\Omega}$(°/d) $\Delta\Omega_p$(°/d)	$\Delta a_{\dot{\Omega}}$ (km) Δa_p (km)
19	Herschel Gap IEG	118188.42 ± 0.04		1	8.27 ± 0.06	347.32 ± 0.41	4.97362 ± 0.00045	0.00826	−54.96 ± 2.98
		173	0.41	1	0.34 ± 0.03	279.55 ± 4.80	−4.95092 ± 0.01091	−0.01809	−121.61 ± 73.32
				2	1.34 ± 0.06	95.16 ± 1.20	378.89248 ± 0.00138	0.01218	−2.50 ± 0.28
				2_{Mimas}	0.89 ± 0.06	82.69 ± 1.86	381.98160 ± 0.00239	−0.00190	0.39 ± 0.49
				3	0.71 ± 0.05	5.26 ± 1.51	503.53264 ± 0.00181	0.01392	−2.16 ± 0.28
				4	0.35 ± 0.05	89.58 ± 2.32	565.85131 ± 0.00276	0.01337	−1.85 ± 0.38
				5	0.36 ± 0.06	71.76 ± 1.77	603.24143 ± 0.00197	0.01197	−1.55 ± 0.26
				6	0.37 ± 0.06	4.74 ± 1.50	628.16426 ± 0.00190	0.00711	−0.89 ± 0.24
				7	0.37 ± 0.05	45.09 ± 1.26	645.97255 ± 0.00159	0.00991	−1.20 ± 0.19
				8	0.34 ± 0.05	31.40 ± 1.24	659.32551 ± 0.00169	0.00876	−1.04 ± 0.20
				10	0.25 ± 0.05	24.43 ± 1.40	678.02618 ± 0.00174	0.01366	−1.58 ± 0.20
18	Herschel Ringlet (R7) IER	118234.30 ± 0.02		1	1.49 ± 0.03	172.81 ± 1.26	4.96229 ± 0.00140	0.00382	−25.44 ± 9.36
		171	0.26	1	1.49 ± 0.02	274.14 ± 0.64	−4.92970 ± 0.00144	−0.00370	−24.90 ± 9.68
				0	0.32 ± 0.03	237.88 ± 5.66	747.36440 ± 0.00607	−0.03297	3.49 ± 0.64
				2_{Mimas}	0.69 ± 0.03	79.00 ± 1.36	381.98129 ± 0.00157	−0.00221	0.45 ± 0.32
17	Herschel Ringlet (R7) OER	118263.25 ± 0.04		1	1.76 ± 0.05	264.77 ± 1.78	4.95659 ± 0.00178	0.00247	−16.47 ± 11.87
		147	0.35	1	2.12 ± 0.03	294.58 ± 0.77	−4.93101 ± 0.00192	−0.00930	−62.71 ± 12.91
				2	0.37 ± 0.05	6.80 ± 3.98	378.53785 ± 0.00484	0.02192	−4.50 ± 1.00
				2_{Mimas}	0.72 ± 0.05	77.59 ± 2.30	381.98303 ± 0.00231	−0.00047	0.10 ± 0.47
				3	0.32 ± 0.05	32.76 ± 3.08	503.04880 ± 0.00336	0.01216	−1.89 ± 0.52
				4	0.20 ± 0.05	76.13 ± 3.75	565.30770 ± 0.00401	0.01070	−1.48 ± 0.56
				5	0.22 ± 0.05	54.38 ± 2.73	602.66098 ± 0.00297	0.00776	−1.01 ± 0.39
16	Herschel Gap OEG	118283.52 ± 0.01		1	0.24 ± 0.02	127.45 ± 5.24	4.94609 ± 0.00553	−0.00500	33.37 ± 36.92
		176	0.15	1	0.25 ± 0.01	57.07 ± 2.62	−4.92430 ± 0.00506	−0.00560	−37.78 ± 34.15
				0	1.27 ± 0.02	232.50 ± 0.88	746.91637 ± 0.00097	−0.01679	1.78 ± 0.10
				2_{Mimas}	0.67 ± 0.02	76.01 ± 0.86	381.98441 ± 0.00099	0.00091	−0.19 ± 0.20
				−3	0.11 ± 0.02	96.61 ± 3.35	1000.83562 ± 0.00412	−0.02601	2.05 ± 0.32
				−2	0.11 ± 0.02	144.86 ± 5.60	1125.34236 ± 0.00677	−0.00813	0.57 ± 0.47
				−1	0.23 ± 0.02	197.18 ± 4.64	1498.79019 ± 0.00551	−0.02688	1.41 ± 0.29
16	Herschel Gap OEG	118283.51 ± 0.01		1	0.28 ± 0.02	113.47 ± 3.70	4.94653 ± 0.00467	−0.00456	30.41 ± 31.15
		176	0.11	1	0.24 ± 0.01	58.29 ± 2.06	−4.92546 ± 0.00389	−0.00676	−45.61 ± 26.23
				0	1.27 ± 0.01	233.42 ± 0.68	746.91625 ± 0.00074	−0.01697	1.80 ± 0.08
				1	0.18 ± 0.02	244.98 ± 5.78	5.08901 ± 0.00736	0.13826	−923.00 ± 49.17
				2_{Mimas}	0.68 ± 0.01	77.00 ± 0.63	381.98423 ± 0.00074	0.00073	−0.15 ± 0.15
				−3	0.07 ± 0.01	90.70 ± 3.66	1000.84253 ± 0.00472	−0.01917	1.51 ± 0.37
				−2	0.11 ± 0.01	147.75 ± 3.90	1125.33982 ± 0.00487	−0.01076	0.75 ± 0.34
				−1	0.25 ± 0.02	196.49 ± 3.22	1498.79145 ± 0.00387	−0.02574	1.35 ± 0.20

[a] The epoch is UTC 2008 January 1, 12:00:00.

In a complementary study based on *Cassini* ISS images, Spitale and Hahn (2016) determined best-fitting keplerian models for each ringlet edge, and searched for evidence of additional free and forced normal modes. For the $m = 1$ (keplerian) mode, they found $ae = 28.32$ and 28.52 km for the inner and outer edges (assuming a common pattern speed of 5.02691° d^{-1}) very similar to our corresponding values of 27.81 and 29.72 km. They identified $m = 2$ Mimas modes on the two edges with amplitudes of 1.62 and 1.20 km, assuming a pattern speed of 381.9842° d^{-1}, roughly consistent with our results of 2.09 and 1.78 km. They found only one other mode: a free $m = 2$ mode on the outer ringlet edge with $A_2 = 2.22$ km; our corresponding result is $A_2 = 1.54$ km for our orbit model including only a single $m = 1$ mode, and $A_2 = 2.02$ km for the orbit fit described previously that included a second simultaneous $m = 1$ mode with a slightly different apsidal precession rate (i.e., pattern speed). By virtue of the very high spatial resolution of the occultation data compared to the imaging data, we were able to identify an additional 5 OLR-type modes on the Huygens IER and an $m = 5$ ILR-type mode on the Huygens OER—see Table 2 for details.

Despite the nearly identical eccentricities of its inner and outer edges, the Huygens ringlet exhibits substantial variations in its radial width. These are readily visible in Fig. 11, and are plotted vs true anomaly and the mean radius of the ringlet in **Fig. SM-2**. Observed widths vary from 11–28 km, but there is no apparent correlation with true anomaly or mean ringlet radius. Instead, it appears that most of the observed width variations in the occultation data can be accounted for by the combined effect of the various normal modes on each edge identified above. As indicated by the dashed lines in the upper panel of Fig. SM-2, the combined amplitudes of all modes other than $m = 1$ or the $m = 2$ Mimas modes (both of which are nearly identical on the inner and outer ring edges, and so do not contribute to width variations) amount to ± 6.4 km on the inner edge and ± 6.5 km on the outer edge, or ± 12.9 km in the width. As further evidence in support of this assertion, we note that the rms residuals of our fits to the individual ringlet edges are only 1.30 and 0.97 km, respectively, indicating that we can successfully model each edge independently, despite the large scatter in Fig. SM-2. However, this conclusion seems to disagree with the results of Spitale and Porco (2006), who in a preliminary study of the Huygens ringlet in *Cassini* images found what appeared to be substantial temporal variations in the Huygens ringlet's mean width. This is difficult to reconcile with the fits presented here. We have tried subdividing our dataset by year of acquisition, but find no obvious changes in the mean width or in its range of variation.

In a recent investigation, Spitale and Hahn (2016) propose that the Huygens ringlet contains two large objects (features A and B) that systematically perturb the inner edge of the ringlet. They associate the larger of these, feature A, with a proposed embedded satellite with a diameter of ~3.6 km that produces IER radial distortions of about 10 km over a longitudinal extent of about 20° (as

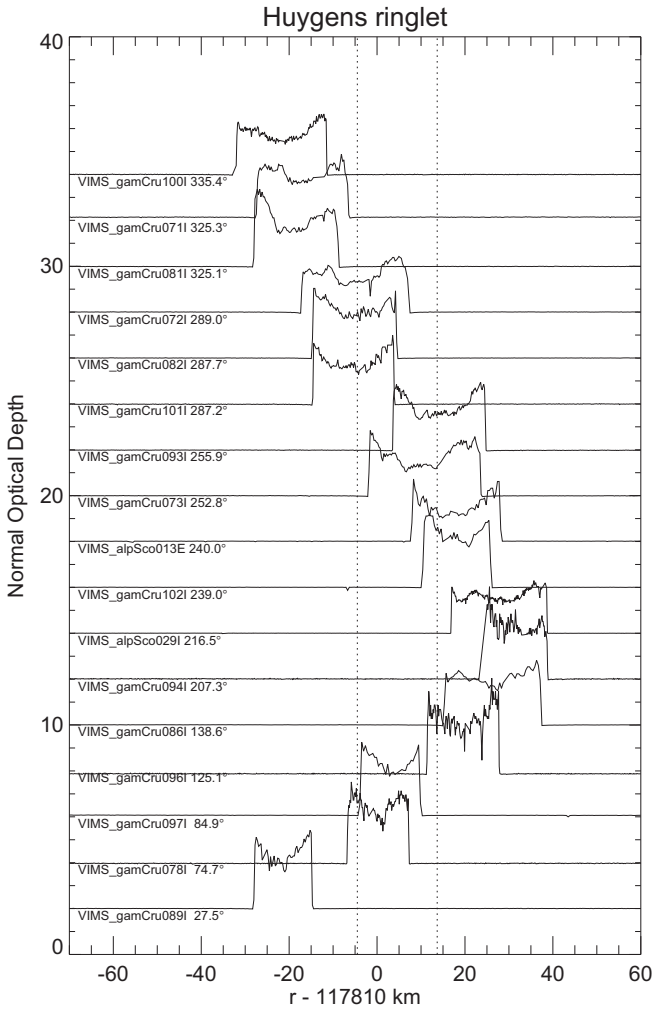

Fig. 11. Optical depth profiles for the Huygens ringlet. Profiles are derived from selected VIMS stellar occultation profiles, offset vertically by a constant amount, and arranged (and labeled) in order of increasing true anomaly of the ringlet's midline. Vertical dotted lines indicate the mean radii of the ringlet edges, based on our orbital fits.

estimated from their Fig. 11). In contrast, the largest individual deviations of the occultation data from our models for the inner and outer edges are far below 10 km: +4.4 and −1.4 km, respectively. In **Fig. SM-3**, we plot the residuals of our model fits to each edge as a function of mean anomaly, and mark the locations of the putative features A and B at the locations for these features estimated from Fig. 19 of Spitale and Hahn (2016). If these are long-lasting features on the inner edge orbiting at the local Keplerian rate, we would expect to see a cluster of larger residuals at these locations in our occultation. No such pattern of residuals is seen. Our alternative suggestion is that the occultation data did indeed sample the regions near features A and B, but that the structures observed in the ISS images represent radial deviations associated with the OER-type normal modes at longitudes and at moments when they happen to be largely in phase.

Without knowing the exact time of the imaging observations, and in light of the very fast pattern speeds of these modes, it is not possible to calculate the actual ring shape for the ISS observations based on the normal modes we have identified. Instead, as a plausibility argument, we show in **Fig. SM-4** three separate representations of the instantaneous shape of the Huygens ringlet, based on random phases of the $m = -10, -5, -4, -3,$ and -2 OLR modes on the inner edge of the ringlet, and the $m = 2$ and 5 ILR modes on the outer edge of the ringlet. (For simplicity, we ignore the $m = 1$ and the forced $m = 2$ Mimas modes, which are in phase for both edges.) To our eyes, these three simulations qualitatively resemble the ISS observations shown in Fig. 11 of Spitale and Hahn (2016), and in particular the features that they label as A and B seem quite consistent in character with the inner ringlet edge deviations (marked by arrows in Fig. SM-4) resulting from the coaddition of normal modes that we have positively identified as present in the occultation data.

Of course, this interpretation requires that the long-term coherence of the two features and their apparent motion at the keplerian rate, as asserted by Spitale and Hahn (2016), be coincidental or illusory—future *Cassini* ISS observations of the Huygens ringlet that confirm or refute the persistence of features A and B and their pattern speeds are likely to provide the best test of these two competing proposals. Perhaps the most secure statement about our results is that they do not provide independent or supporting evidence for the proposed existence of embedded satellites within the Huygens ringlet.

4.2. R6: The Strange ringlet

Between the Huygens ringlet and the outer edge of the Huygens gap lies an opaque, very narrow feature designated R6 by Colwell et al. (2009b) but informally known as the Strange ringlet. Sample profiles of this ringlet are shown in Fig. 16, arranged by true anomaly (see fit below). While not apparent in these particular profiles, which were mostly obtained at a rather steep elevation angle to the ring plane of $B = 62.3°$, in some *Cassini* images as well as some low-elevation occultations the Strange ringlet appears not to lie within the Huygens gap at all, but is superimposed on the ring material exterior to the Huygens gap. A mild example of this is the α Sco ingress profile for rev 13 in Fig. 16, which was obtained at $B = 32.5°$ and shows the ringlet right at the outer edge of the gap. This curious circumstance is most easily accounted for by a nonzero inclination, combined with a low viewing angle with respect to the ring plane.

Because of its suspected inclination, we used our spectral scanning program to search for a vertical distortion with $m = 1$ and a plausible nodal regression rate, after first fitting a simple precessing keplerian ellipse to the data, with the results shown in **Fig. SM-5**. Here we plot the vertical amplitude and post-fit residuals for the ringlet's centerline as a function of the assumed nodal precession rate, $\dot{\Omega}$. We find a strong signal at $\dot{\Omega} = -4.960° \, d^{-1}$, very close to the predicted value of $\dot{\Omega}_{sec} = -4.9745° \, d^{-1}$ at the ringlet's mean radius of 117907.7 km, with a vertical amplitude of ~7.5 km. The importance of a nonzero inclination in accounting for the Strange ringlet's apparent radial excursions is reinforced by the fact that the largest deviations in our data set from a simple equatorial keplerian ellipse occur for the low-elevation RSS occultations on revs 57–64 and range from −40 to +30 km (see Eq. (8)). The inclination probably also explains why this ringlet was seen in the *Voyager* PPS stellar occultation data (Esposito et al., 1983), but not in the *Voyager* radio occultation profile, which was obtained at a very low elevation of 5.6° (Tyler et al., 1983).

Our orbital fits to the Strange ringlet include separate fits for the inner and outer ring edges, where clearly measurable, as well as fits of the ringlet's center radius (COR = center of ringlet), because of the possibility that the ringlet might not be resolved in some occultations. The best fit for the COR, given in Table 2, shows a substantial eccentricity ($ae = 7.5 \pm 0.2$ km) and inclination ($a \sin i = 7.1 \pm 0.2$ km), as well as a plethora of statistically significant normal modes. In order of decreasing amplitude, we find $m = 2$, 0, and 3, with amplitudes from 3.8 to 2.3 km. There is also an $m = 2$ Mimas mode with an amplitude of 1.5 km. In Fig. 17 we plot the fit residuals for each of these modes, where the abscissa

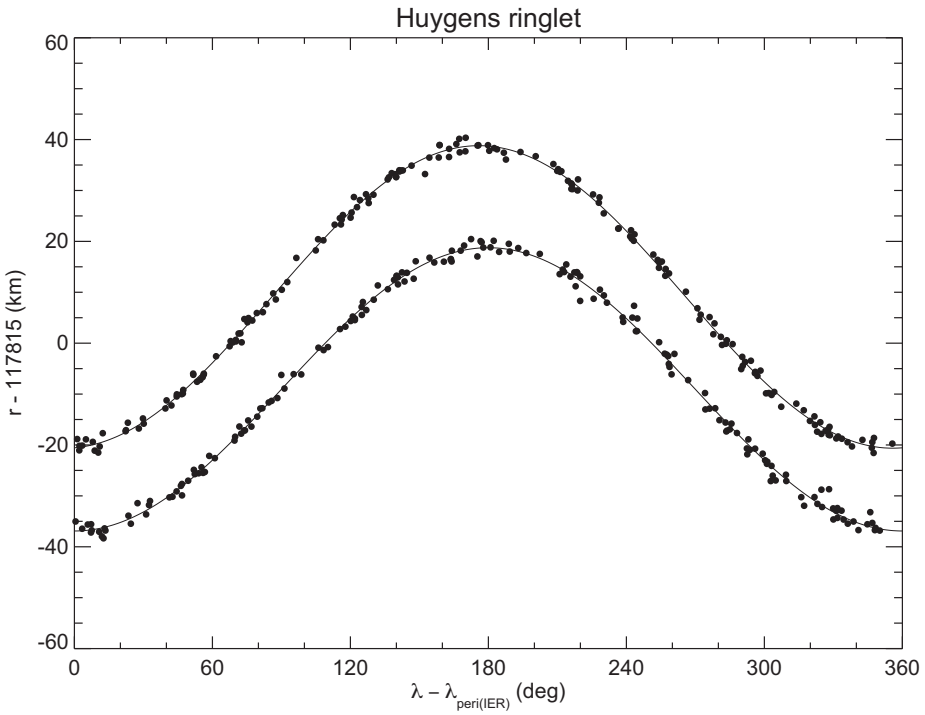

Fig. 12. The measured radii of the Huygens ringlet inner and outer edges, plotted as a function of longitude relative to the periapse longitude of the inner ring edge. The fitted $m = 1$ amplitudes are 27.7 km (IER) and 27.8 km (OER); other normal modes have not been subtracted (see Table 2). Note the phase offset of the outer edge relative to the inner edge of $\Delta\lambda = \varpi_{OER} - \varpi_{IER} = 4.2^\circ$.

Table 4
Orbital elements of Laplace Ringlet and Gap.

ID	Feature	a(km)		m	ae(km)	ϖ_0(°)[a]	$\dot{\varpi}$ (°/d)	$\Delta\dot{\varpi}$ (°/d)	$\Delta a_{\dot{\varpi}}$ (km)
		N	rms (km)		$a \sin i$ (km)	Ω_0(°)	$\dot{\Omega}$(°/d)	$\Delta\dot{\Omega}$(°/d)	$\Delta a_{\dot{\Omega}}$ (km)
					A_m (km)	δ_m(°)	Ω_p(°/d)	$\Delta\Omega_p$(°/d)	Δa_p (km)
115	Laplace Gap IEG	119844.78 ± 0.03		1	3.25 ± 0.04	310.11 ± 0.73	4.72673 ± 0.00087	0.00254	−17.99 ± 6.19
		112	0.26	1	0.25 ± 0.02	10.17 ± 4.59	−4.69233 ± 0.00863	0.00179	12.80 ± 61.81
				2_{Mimas}	0.29 ± 0.04	82.70 ± 4.17	381.98579 ± 0.00499	0.00229	−0.49 ± 1.06
14	Laplace Ringlet IER	120036.53 ± 0.02		1	1.19 ± 0.02	236.12 ± 1.34	4.71250 ± 0.00139	0.01524	−108.87 ± 9.90
		168	0.20		[0.000][b]				
				0	2.22 ± 0.03	160.05 ± 0.68	730.64946 ± 0.00072	−0.05715	6.29 ± 0.08
				2_{Mimas}	0.27 ± 0.03	75.51 ± 2.90	381.98821 ± 0.00304	0.00471	−1.01 ± 0.65
				−4	0.13 ± 0.02	19.39 ± 2.76	918.04749 ± 0.00343	−0.03268	2.84 ± 0.30
				−2	0.74 ± 0.02	141.40 ± 1.03	1100.71164 ± 0.00122	−0.04519	3.28 ± 0.09
				−1	0.61 ± 0.02	193.60 ± 2.47	1466.03143 ± 0.00272	−0.07870	4.30 ± 0.15
12	Laplace Ringlet OER	120077.75 ± 0.01		1	2.79 ± 0.02	51.49 ± 0.36	4.72457 ± 0.00040	0.03307	−236.69 ± 2.83
		174	0.14		[0.000][b]				
				2	0.62 ± 0.02	86.10 ± 0.82	369.88543 ± 0.00099	0.02822	−6.03 ± 0.21
				2_{Mimas}	0.22 ± 0.02	78.01 ± 2.38	381.98827 ± 0.00254	0.00477	−1.02 ± 0.54
				3	0.42 ± 0.02	34.20 ± 0.82	491.60221 ± 0.00101	0.02298	−3.71 ± 0.16
				4	0.25 ± 0.02	46.96 ± 0.97	552.46291 ± 0.00136	0.02267	−3.26 ± 0.20
				6	0.12 ± 0.02	16.13 ± 1.37	613.31846 ± 0.00148	0.01720	−2.23 ± 0.19
114	Laplace Gap OEG	120085.65 ± 0.01		1	1.34 ± 0.01	308.73 ± 0.54	4.71707 ± 0.00058	0.02668	−190.99 ± 4.18
		172	0.10		[0.000][b]				
				2_{Mimas}	0.22 ± 0.01	76.33 ± 1.62	381.98649 ± 0.00165	0.00299	−0.64 ± 0.35

[a] The epoch is UTC 2008 January 1, 12:00:00.
[b] Quantities in square brackets were held fixed during orbit determination.

is the appropriate argument, $\theta = m(\lambda - \Omega_p t - \delta_m)$ for each case. The rms residual for the final fit remains rather large at 1.60 km, suggesting that the Strange ringlet probably harbors additional perturbations, as yet unidentified. (If we neglect the inclination, our best fit has an unsatisfactory rms residual of 8.4 km.) In a separate fit to the IER, we find normal modes $m = 0, 2, 3$ and 5, and for the OER there is a combination of both ILR- and OLR-type modes with $m = -1, 0, 2,$ and 3; both the IER and OER also show clear $m = 2$ Mimas modes.

There is no obvious pattern in the varying widths shown by the Strange ringlet in Fig. 16, which range from ∼1 to ∼3.5 km. The corresponding width-radius relationship is shown in **Fig. SM-6**. Note from Table 2 that the inner edge of the ringlet nominally has larger eccentricity than outer edge! The difference in the fitted amplitudes of the $m = 2$ modes on the inner and outer edges contributes a systematic ∼0.4 km $m = 2$ pattern to the width of the ringlet, but this is a small fraction of the overall width variations, which remain unexplained.

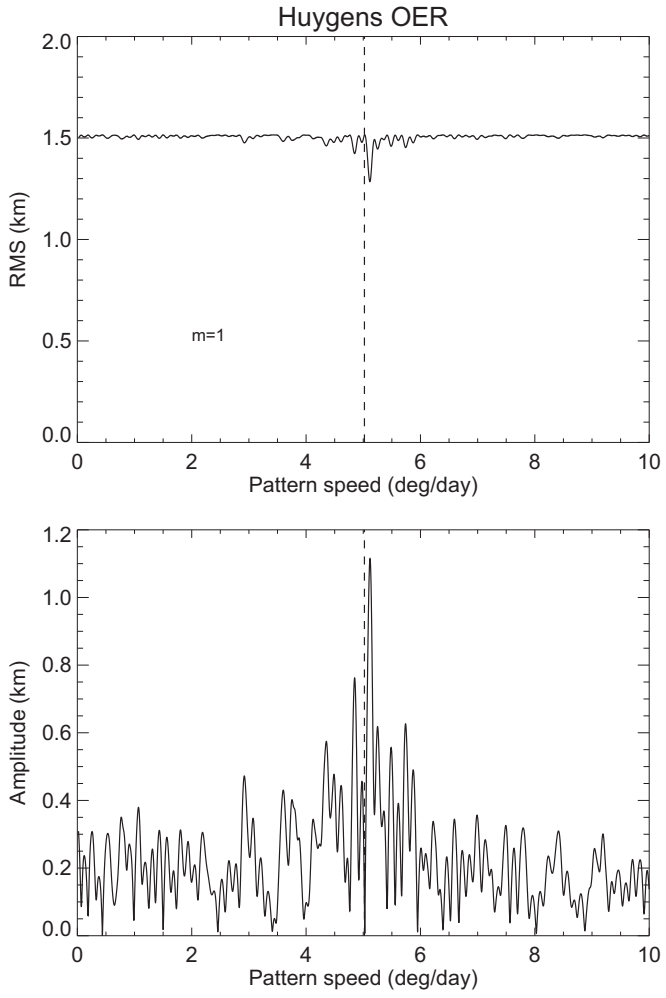

Fig. 13. Huygens OER normal mode scan for secondary $m = 1$ mode. Note the zero amplitude at the nominal pattern speed for the appropriate radius of the gap edge, confirming that the best-fitting single $m = 1$ eccentric model has already been removed. (When the pattern speeds and amplitudes of both $m = 1$ modes are allowed to be fitted simultaneously, the amplitude of the subsidiary $m = 1$ mode increases to 3.9 km—see Table 2.).

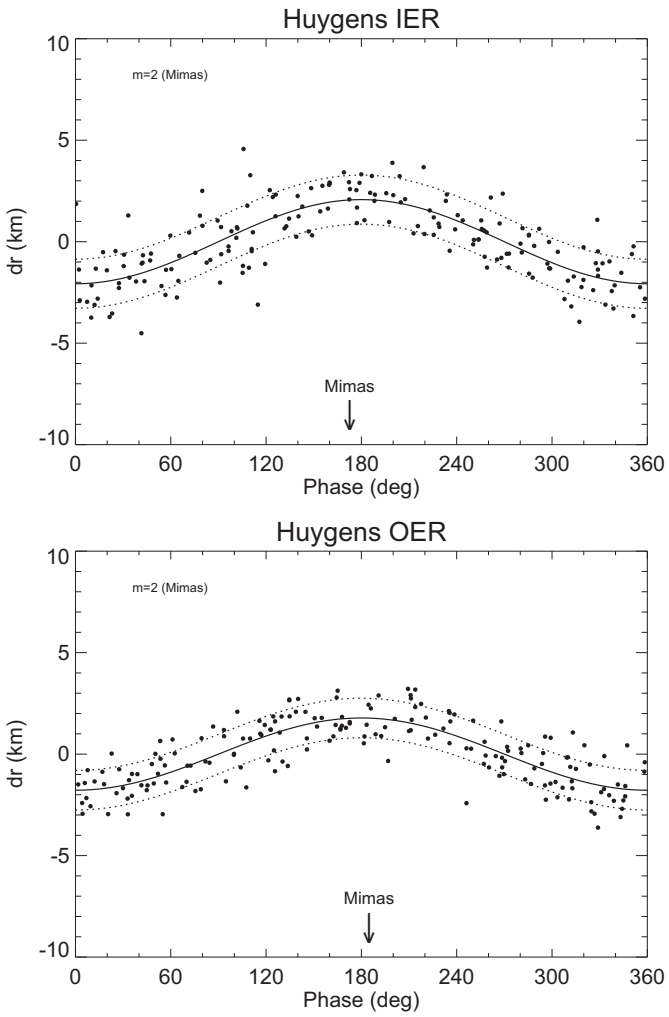

Fig. 14. The Huygens ringlet residuals vs $m = 2$ phase. The fitted amplitudes are 2.0 km (IER) and 1.8 km (OER). Arrows mark the longitude of Mimas at epoch: -7.4° and $+4.8^\circ$ relative to apoapse for the inner and outer ringlet edges, respectively.

4.3. Huygens gap outer edge

The outer edge of the Huygens gap harbors a significant $m = 2$ signature, rotating at a pattern speed very close to the mean motion of Mimas, as also found for the Huygens and Strange ringlets. In this case, the amplitude is 1.3 km. But this is not the dominant perturbation on this edge. Unlike the simple gaps with their generally circular outer edges, we find a strong signature of a freely-precessing keplerian ellipse (i.e., an $m = 1$ distortion) with $ae = 2.2$ km, which is visible (with some difficulty) at the right in Fig. 16.

Second in importance is an $m = 0$ normal mode, with an amplitude of 1.8 km. A search for other modes yields evidence for additional OLR-type modes with $m = -1$, -3 and -4 and amplitudes of 0.3–0.8 km (see Table 2). There is also a small but significant inclination with $a \sin i = 0.45 \pm 0.03$ km. It is surprising to find an $m = 1$ ILR-type mode on the outer edge of a gap, and we note that the fitted apsidal precession rate for this mode of $\dot{\varpi} = 5.035 \pm 0.002^\circ\,\mathrm{d}^{-1}$ is significantly faster (by $0.03^\circ\,\mathrm{d}^{-1}$) than the expected value at this distance. It may be the result of a forced response to the nearby eccentric Huygens ringlet, although the precise mechanism remains to be explored. The pattern speeds for the other normal modes are all very close to their predicted values, with $0.9 < \Delta a_p < 2.7$ km. The postfit rms residual is an acceptable 0.43 km, but considerably larger than the typical uncertainty in the edge measurements themselves or their computed absolute radii.

4.4. Summary

Several things stand out when we compare our orbital fits for the Huygens and Strange ringlets and for the outer edge of the gap wherein they reside. Most notable are the nonzero inclinations we have found for all three features, especially for the Strange ringlet. It might be suspected that the smaller vertical amplitudes we have found for the Huygens ringlet and gap edge represent inclinations forced by the nearby Strange ringlet, but in this case we would expect to find matching precession rates and aligned (or anti-aligned) nodes for all three features. While the fitted precession rates are arguably equal to within their uncertainties, and the nodes of the two ringlets are indeed quite similar, the node of the gap's outer edge is ~130° away from that of the Strange ringlet. Also intriguing are the fitted apsidal precession rates $\dot{\varpi}$, and their deviations from the predicted values, $\Delta\dot{\varpi}$, listed in Table 2. These appear to form part of a larger pattern of anomalous precession rates found in the complex gaps, and will be discussed as a group in Section 9 below.

In Fig. 18 we show the distribution of normal mode amplitudes for all four measured features in the Huygens gap, in the same format as Figs. 9 and 10 above.

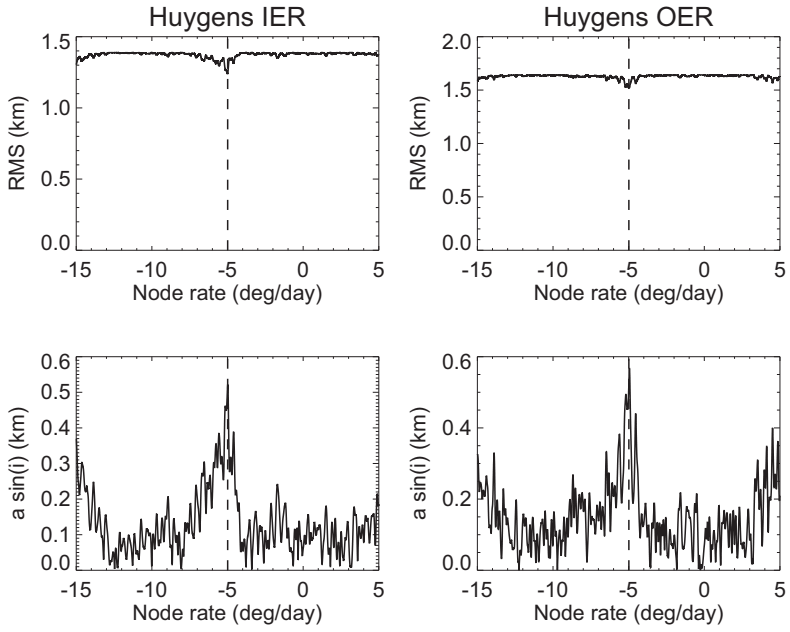

Fig. 15. Huygens ringlet IER and OER node rate scans. Both inner and outer edges show similar inclinations, with fitted $a \sin i \simeq 0.5$ km, and nearly identical nodal regression rates that are close to the predicted values at the center of the ringlet.

5. The Herschel gap

Moving outwards from the Huygens gap, we come to the ~100 km-wide Herschel gap with its eponymous ringlet, as illustrated in Fig. 19. Most striking here is the eccentricity of the gap's inner edge, which is readily apparent in the figure, compared with the near-circularity of its outer edge. Upon closer inspection one sees that the ringlet, too, has noncircular edges, though perhaps not simple ellipses. These observations are borne out by our orbital fits, which show that the inner gap edge exhibits one of the largest eccentricities in the Cassini Division, with $ae = 8.3$ km. Indeed, the ellipticity of this feature was originally noted by Flynn and Cuzzi (1989), using relatively low-resolution *Voyager* images. Also detected on the gap's inner edge are a plethora of ILR-type modes with $m = 2, 3, 4, 5, 7, 8$ and 10 and amplitudes of 0.2–1.3 km, a forced $m = 2$ Mimas mode of 0.89 km amplitude, and a probable inclination with $a \sin i = 0.34$ km (see Table 3). The outer gap edge also proves to be measurably noncircular, dominated by an $m = 0$ mode with an amplitude of 1.27 km, with a forced Mimas mode of amplitude 0.67 km and a weak $m = 1$ eccentric mode ($ae = 0.24$ km). This edge also shows a small inclination ($a \sin i = 0.25$ km) as well as three other very weak OLR-type modes ($m = -1, -2$, and -3) with amplitudes of 0.1–0.2 km. Post-fit rms residuals are 0.41 and 0.15 km for the inner and outer gap edges, respectively. The mean width of the Herschel gap is 95.1 km.

When searching for signatures of additional normal modes, we identified a potential secondary $m = 1$ mode on the outer edge of the Herschel gap. **Fig. SM-7** shows a normal mode scan for $m = 1$ of the residuals to the best-fitting eccentric model, with a clear signature for a mode with a pattern speed of about $5.1^\circ\,\mathrm{d}^{-1}$. When both the primary and secondary $m = 1$ modes are fitted simultaneously, the amplitude of the secondary mode reaches 0.17 km. While somewhat correlated with the main $m = 1$ signature, the final fitted pattern speed of the second $m = 1$ mode is substantially larger than for the first: $\dot{\varpi} = 5.089^\circ\,\mathrm{d}^{-1}$ compared to $\dot{\varpi} = 4.947^\circ\,\mathrm{d}^{-1}$. The best fit that includes this second $m = 1$ mode is included in Table 3, and has a significantly reduced post-fit rms error of just 0.11 km. It is perhaps significant that the apse rate of the smaller $m = 1$ mode lies rather close to the fitted $m = 1$ pattern speed of the B ring's outer edge of $\dot{\varpi} = 5.0835 \pm 0.0019^\circ\,\mathrm{d}^{-1}$ (Nicholson et al., 2014a), hinting that the B ring itself may be responsible for this additional $m = 1$ mode. On the other hand, the beat period between the primary and secondary $m = 1$ modes is on the order of a decade, roughly the span of data included in the fit, and thus there is a possibility that this signature is an artifact of aliasing. If so, it is a rare phenomenon, since we have identified only one other instance of a putative secondary $m = 1$ mode in our fits to over 150 ring and gap edges.

5.1. The Herschel ringlet

Our fits show that the Herschel ringlet's edges both have small but significant eccentricities, with amplitudes $ae = 1.5$ and 1.8 km, and comparable inclinations, with $a \sin i = 1.5$ and 2.1 km (see Table 3). In addition, there are Mimas modes with amplitudes of ~0.7 km. However, neither the nodes nor especially the pericenters of the ringlet's inner and outer edges are well-aligned, with differences of $\delta\Omega_0 = 20 \pm 2^\circ$ and $\delta\varpi_0 = 95 \pm 3^\circ$. Moreover, the fitted apsidal and nodal precession rates of the two edges each differ at the 4σ level, suggesting that the inner and outer edges may be behaving independently of one another. Fig. 20 shows the measured radii of the Herschel ringlet's edges relative to the periapse longitude of the inner edge. Note that difference in apse rate results in about 18° shift in periapse longitudes over the course of 3000 days, the interval spanning the observation period of our observations.

Post-fit rms residuals are 0.25 and 0.45 km for inner and outer edges, respectively, while the mean width of the ringlet is 28.9 km, slightly less than one-third of the gap width.

As in the case of the Strange ringlet, we used our spectral-scanning program to verify the reality of the inclinations of the Herschel ringlet's edges. **Fig. SM-8** shows scans of residuals vs nodal rate; in each case we see a clear signature of an inclination with a nodal regression rate very close to the predicted value. The amplitudes are 1.4 and 1.6 km, respectively, compared to the least-squares fit results of 1.5 and 2.1 km. As an aside, we note that Nicholson et al. (1990) found an apparent radial displacement of the Herschel ringlet between the *Voyager* PPS and RSS profiles of ~10 km, which is much larger than the eccentricities established by our fits to the much more extensive *Cassini* data. These results

can probably be reconciled by appealing to the ringlet's inclination, and to the very low elevation of the *Voyager* RSS occultation: at $B = 5.6^\circ$, a vertical displacement of $z = 1.8$ km can appear as an *apparent* radial displacement of as much as $z/\tan B = 18$ km (see Eq. (8)), even larger than the observed value.

The Herschel ringlet's width–radius relation is illustrated in **Fig. SM-9**, but is relatively uninformative. The overall width variations are modest ($24 - -33$ km) and there is little correlation with the ringlet's mean radius, reflecting the misalignment of the pericenters of the inner and outer edges. Nevertheless, when using the mode-scanning algorithm, we find clear evidence for an $m = 1$ width variation at the appropriate pattern speed for the ring. We reconcile this strong detection of a width variation with true anomaly, and the corresponding weak evidence for a classical width-radius relation expected for an eccentric ringlet, by appealing to Fig. 20, which shows that the ring width varies systematically with the anomalies of the two edges, but is not a minimum at $f = 0^\circ$ or a maximum at $f = 180^\circ$.

5.2. Summary

It is unclear whether the Herschel ringlet can be regarded as a dynamically coherent eccentric ringlet, in the usual meaning of this term. The differing pericenter longitudes and rates for the edges of this ringlet suggest that the two edges are behaving independently, although the situation is not so clear for the inclinations and nodes. The inclinations of the edges are similar, but the node rates differ by $\sim 4\sigma$, even though the fitted nodes are just 20° apart. Taken together, these suggest that the ringlet as whole may be inclined, even if the pericenters are not locked together, but just how such a configuration might arise and be maintained is admittedly perplexing. Further complicating the story is the evidence for a weak secondary $m = 1$ mode on the Herschel gap's outer edge, perhaps indicative of forcing by the B ring itself.

In Fig. 21 we plot the fitted amplitudes of the normal modes identified for the Herschel gap and ringlet, in the same format as for the Huygens gap.

6. The Laplace gap

The wide Laplace gap and its prominent ringlet dominate the outer part of the Cassini Division. At 241 km, it is second in width only to the Huygens gap, and is comparable to the Maxwell gap in the C ring. As can be seen in Fig. 22, the Laplace ringlet is located extremely close to the outer edge of the gap, leaving a space of only ~8 km between the ringlet and the gap edge, which is reduced to < 4 km when the eccentric edges of ringlet and gap are anti-aligned. Note that, unlike the situation with the Herschel gap, the optical depths immediately adjacent to the inner and outer gap edges are very different, and both regions are much less opaque than the ringlet (see Fig. 1).

Although the inner edge of the Laplace gap is quite indistinct, and difficult to measure accurately, it—like most of the other Cassini Division gaps—shows a pronounced eccentricity; in this case the amplitude $ae = 3.3$ km. But unlike most other gaps, the Laplace gap also has an eccentric outer edge, albeit with a smaller amplitude of 1.3 km. The Mimas $m = 2$ modes have amplitudes of ~0.25 km, and there is a possible inclination on the inner edge with $a \sin i = 0.25$ km. Curiously, the fitted pericenter longitudes and apsidal precession rates for the inner and outer gap edges are very similar, despite their large radial separation. The rate of the more eccentric inner edge, $\dot{\varpi} = 4.727^\circ\,\mathrm{d}^{-1}$, is fairly close to the predicted value, but that of the outer edge is much too fast, with $\Delta a_{\dot{\varpi}} = -191 \pm 4$ km (see Table 4). Post-fit rms residuals are 0.26 and 0.10 km for the inner and outer gap edges, respectively.

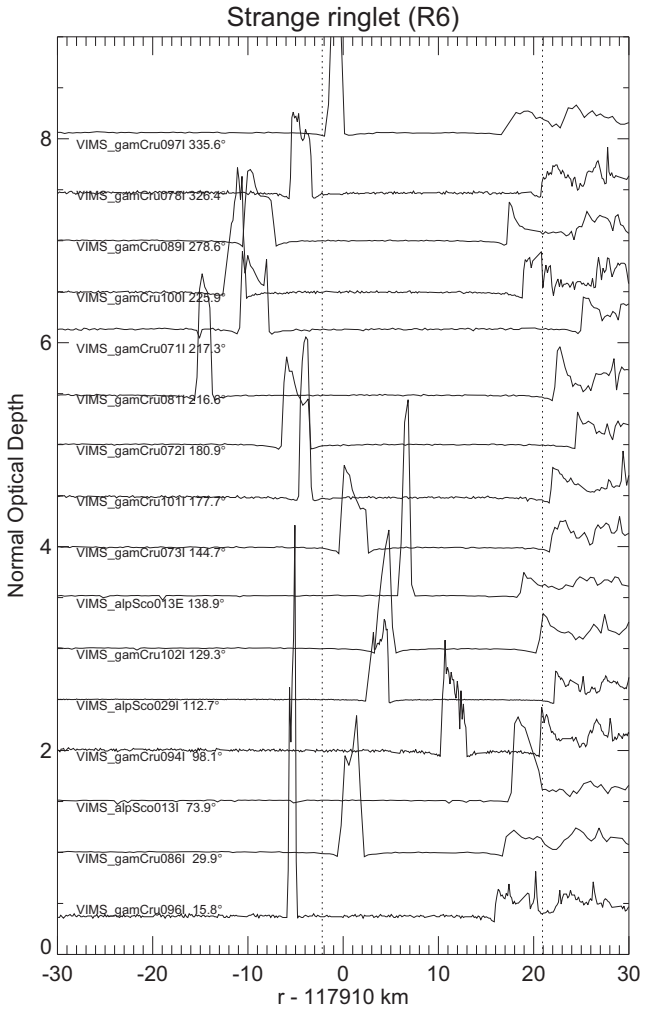

Fig. 16. Optical depth profiles for the Strange ringlet (R6) and the outer edge of the Huygens gap, derived from selected VIMS stellar occultation profiles. The profiles are offset vertically by a constant amount, and arranged (and labeled) in order of increasing true anomaly of the ringlet's midline. Vertical dotted lines indicate the mean radius of the ringlet, based on our orbital fits, and the outer edge of the Huygens gap.

6.1. R10: The Laplace ringlet

Our fits show clearly that both edges of the Laplace ringlet (R10) are noncircular, but are dominated by different modes. The inner edge has a small eccentricity ($ae = 1.2$ km), but a somewhat larger $m = 0$ normal mode with an amplitude of 2.2 km as well as two smaller OLR-type modes with $m = -1$ and -2 with amplitudes of ~0.6 km, and an even weaker $m = -4$ mode with an amplitude of 0.1 km. The outer edge is predominantly eccentric ($ae = 2.8$ km), with much smaller ILR-type modes with $m = 2$, 3, 4, 6 and 8 and amplitudes of $0.1 - -0.6$ km. The usual $m = 2$ Mimas modes have amplitudes of ~0.24 km, and there is no detectable inclination on either edge. The pericenters of the inner and outer edges are not aligned, and their fitted apsidal rates are quite different, with that of the outer edge being *faster* than that of the inner edge (see Table 4). So, as in the case of the Herschel ringlet, the Laplace ringlet does not precess rigidly and thus cannot be considered an eccentric ringlet in the usual sense of the term.

The optical depth profiles in Fig. 22 show that the Laplace ringlet has a rather complex internal profile, with quasi-linear ramps at the inner and outer edges and a prominent wavelike structure in its central region. The latter has been identified by

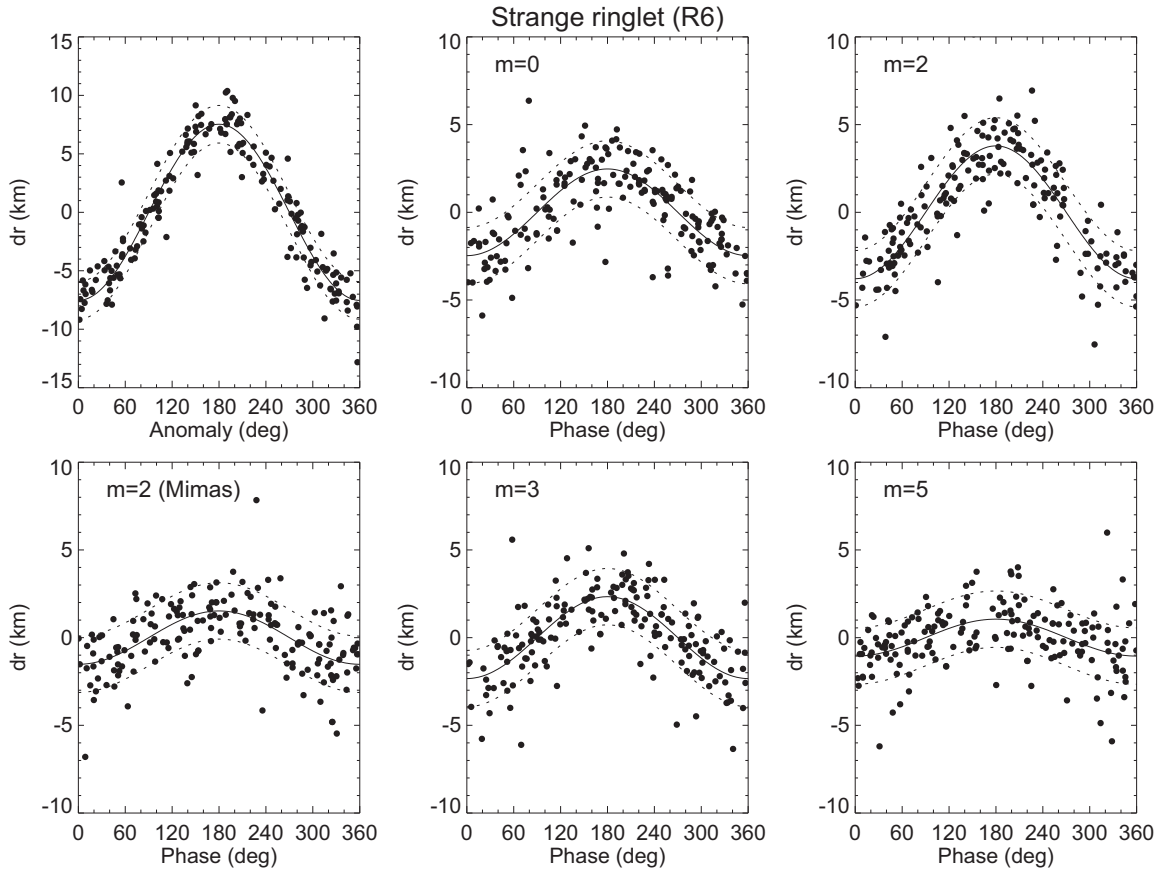

Fig. 17. Observations of Strange ringlet plotted vs mode argument. Note that, for each panel, the inclination and all other modes have been subtracted from the measurements, in order to reveal the mode of interest. See Table 2 for fitted parameters.

Colwell et al. (2009a) as a density wave driven by the Pandora 9:7 inner Lindblad resonance, which is located close to the inner edge of the ringlet at 120036.8 km. Despite this coincidence, and the evidence of the wave, we have been unable to identify any corresponding $m = 8$ perturbation on the ringlet's inner edge. When the profiles are sorted by true anomaly, as they are in Fig. 22, the width of the inner ramp varies systematically, disappearing completely in the upper six profiles. The outer ramp also varies in width, but is apparently present at all longitudes. Looking at these profiles, one has the strong impression that the $m = 0$ and 1 modes we have identified on the edges of the ringlet do not penetrate very far into its interior.

Post-fit rms residuals are 0.20 and 0.14 km for inner and outer edges, respectively, while the mean width of the ringlet is 41.2 km.

The Laplace ringlet's width–radius relation is illustrated in **Fig. SM-10**. The overall width variations are significant (34 – −48 km) but there is little correlation with the ringlet's mean radius, reflecting the fact that the inner and outer edges are dominated by different (and multiple) modes. As before, however, a normal mode scan in the ring width does reveal a weak correlation in ring width with the pattern speed corresponding to the precession rate of the eccentric ringlet, as a result of the nearly anti-aligned apses of the ringlet edges.

In Fig. 23 we plot the fitted amplitudes of the normal modes identified for the Laplace gap and ringlet, in the same format as for the Huygens and Herschel gaps.

7. Normal modes

Perhaps the most striking characteristic of the orbital properties of the Cassini Division ringlets and gaps is the sheer abundance and variety of normal modes identified at the sharp edges of these features. Normal modes in planetary rings were first identified in the narrow uranian γ and δ rings, where conspicuous $m = 0$ and 2 radial distortions were identified with amplitudes of 5.15 and 3.11 km, respectively (French et al., 1986; 1991). These are examples of *global modes* that are coherent across a narrow ringlet. More recently, non-resonant normal mode perturbations with $m = 1, 3, 4,$ and 5 were identified in the outer edge of the B ring (Nicholson et al., 2014a), consistent with the notion that normal modes in a broad ring can arise from density waves reflected by the sharp edge of the ring, effectively trapped in a resonant cavity near the ring boundary (Spitale and Porco, 2010)—we will refer to these as *edge modes*. Additional normal modes were identified at the edges of sharp ringlets in the C ring (Nicholson et al., 2014b), and in this work we have found literally dozens of normal modes of both types in the Cassini Division.

Nicholson et al. (2014b) reviewed the concept of normal modes in planetary rings in some detail (see Section 2 and Appendix A of that work), and here we briefly summarize the key physical concepts. As introduced by Borderies et al. (1986) and further developed by Longaretti and Rappaport (formerly Borderies), outward- and inward-propagating density waves can arise spontaneously in dense, self-gravitating rings, and can result in amplified standing waves in the presence of a feedback mechanism, such as interference between the waves approaching and reflecting from a ring boundary. In its simplest form, this amplification process favors wavelengths of density waves that are comparable to the ringlet width, and a precessing eccentric ringlet can be thought of as such an $m = 1$ global mode. But normal modes are not restricted to narrow ringlets, and a similar feedback mechanism can reinforce additional modes near sharp inner or outer edges of broad rings. For a

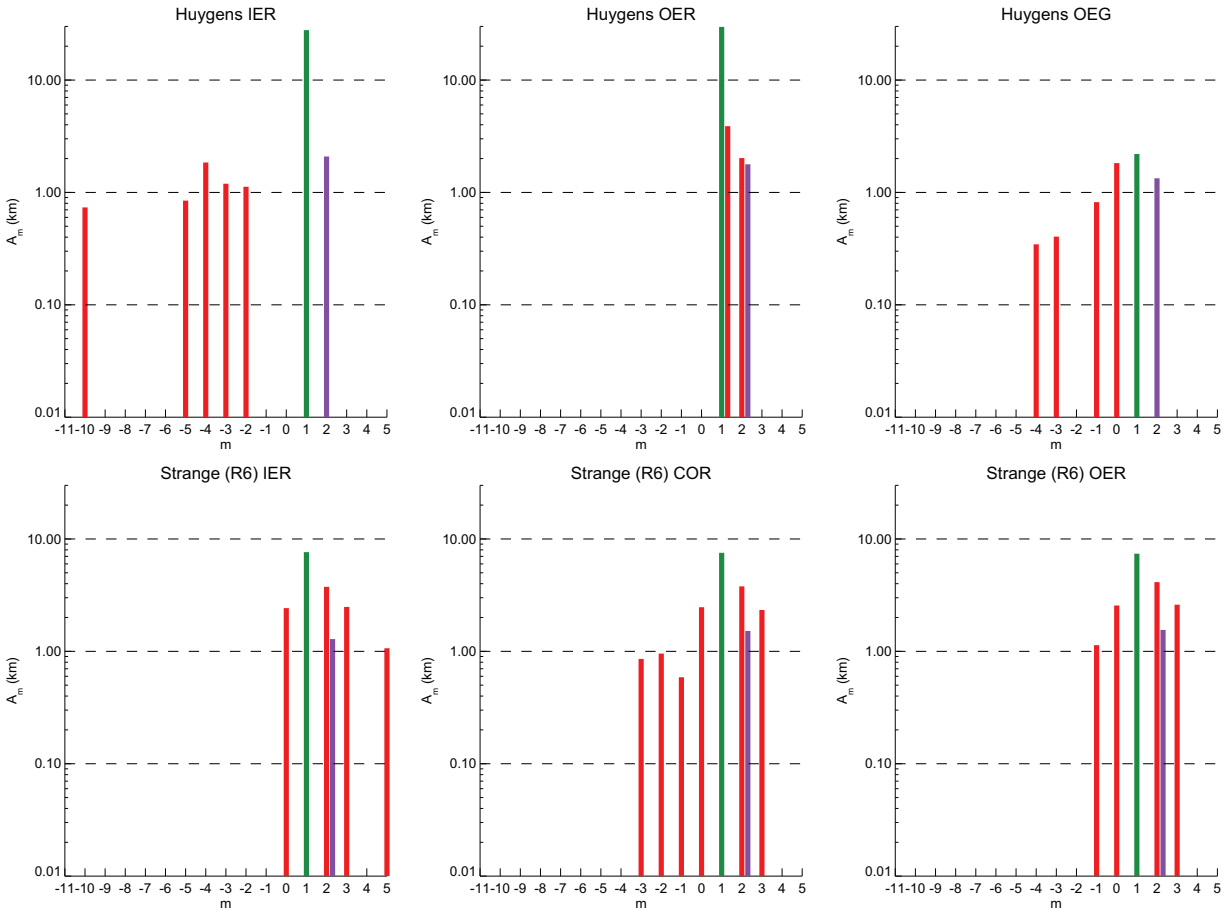

Fig. 18. Detected normal modes for the Huygens and Strange ringlets and the Huygens OEG. Modes are coded by color: free eccentric modes ($m = 1$) are green, other free modes are red, and modes forced by an external satellite (in this case, the $m = 2$ mode forced by Mimas) are violet. Note the presence of a secondary $m = 1$ mode on the Huygens OER. The unexpected $m = 1$ mode on the Huygens OEG may be a forced response to the nearby eccentric Huygens ringlet, given their similar values of $\dot{\varpi}$, although the pericenter leads the latter's by ~110° (see Table 2). Several nearly identical modes are observed on both edges of the Strange ringlet, presumably due to its mean width of only ~2 km. (For interpretation of the references to color in this figure legend, the reader is referred to the web version of this article.)

sharp outer edge, outward-propagating trailing density waves with an ILR within a few radial wavelengths interior to the ring edge will reflect at the edge, back towards its source as a leading wave with the same wavenumber and pattern speed. This will in turn reflect at the ILR and reappear as an outward-propagating trailing wave, ultimately amplifying the mode. A similar situation applies at the inner edge of a broad ring, but in this case the reflection occurs at the *outer* Lindblad resonance (OLR) location within a few wavelengths *exterior* to the ring edge. Thus, our expectation is that ILR-type edge modes (with $m \geq 1$) will appear at the *outer* edges of ringlets and the *inner* edges of gaps (at OERs and IEGs), and OLR-type edge modes (with $m \leq 0$) will appear at the *inner* edges of ringlets and the *outer* edges of gaps (at IERs and OEGs).

7.1. Distribution of ILR- and OLR-type edge modes

The actual distribution of normal modes on ringlet and gap edges is remarkably consistent with this theoretical expectation. Table 5 summarizes the normal modes we have identified for all Cassini Division ringlets and gaps, organized by ringlet and gap type, and further sorted by orbital radius. For completeness, we also list the fitted ae for the nominal global eccentric ($m = 1$) mode, the forced $m = 2$ Mimas mode amplitudes, $a \sin i$ for features with measured inclinations, the post-fit rms residual, and the number of data points. At the top are the IER/OEG features, and as expected, all of the detected modes (other than the eccentric $m = 1$ modes and the $m = 5$ mode at the Barnard gap OEG, probably forced by the nearby Prometheus 5:4 ILR) are OLR-type, with $m \leq 0$. Low wavenumber modes typically have larger fitted amplitudes than higher wavenumber modes, but this is by no means uniformly true. For example, the strongest edge mode for the Huygens ringlet IER is $m = -4$, with an amplitude of 1.83 km, accompanied by marginally weaker $m = -3$ and -2 modes, but no detectable $m = -1$ or 0 modes. The innermost four features have measurable inclinations, and with the exception of the Huygens ringlet IER, the rms residuals for all features are less than 0.5 km. As discussed below, the amplitude of the forced $m = 2$ Mimas mode decreases systematically with increasing distance from the inner edge of the Cassini Division (the outer edge of the B ring). In addition to the usual $m = 1$ keplerian shapes of the ringlets and gaps, there is a possible secondary $m = 1$ mode on the outer edge of the Herschel gap.

Next in Table 5 is the Strange ringlet, narrowest of the ringlets in this study, and perhaps not surprisingly, there is overlap in the modes identified on the inner and outer edges, and the ring mid-line. These modes effectively span the entire ringlet, and are thus more properly thought of as global modes. The combination of large eccentricity and inclination and the abundance of normal modes make this among the most complex kinematical models we

Table 5
Summary of normal modes in Cassini Division features.

Type	ID	Feature	a(km)	−10	−9	−8	−7	−6	−5	−4	−3	−2	−1	0	ae	1	2_M	5	$a \sin i$	rms	N
IER/OEG	54	Huygens Ringlet IER	117805.55	0.74	...	...	...	...	0.85	1.85	1.20	1.12	...	...	27.81	...	2.09	...	0.59	1.30	178
	20	Huygens Gap OEG	117930.90	...	...	...	...	...	...	0.35	0.40	...	0.82	1.82	2.20	...	1.34	...	0.44	0.45	176
	18	Herschel Ringlet IER	118234.30	...	...	...	...	...	...	...	...	...	...	0.32	1.49	...	0.69	...	1.49	0.26	171
	16	Herschel Gap OEG	118283.51	...	...	...	...	...	...	...	0.07	0.11	0.25	1.27	0.28	0.18	0.68	...	0.24	0.11	176
			118283.52	...	...	...	...	...	...	...	0.11	0.11	0.23	1.27	0.24	...	0.67	...	0.25	0.15	176
	13	Russell Gap OEG	118628.40	...	...	...	...	...	...	...	...	...	...	...	0.11	...	0.47	...	...	0.09	160
	15	Jeffreys Gap OEG	118966.70	...	...	...	...	...	...	...	...	...	...	...	0.08	...	0.37	...	...	0.12	162
	118	Kuiper Gap OEG	119406.27	...	...	...	...	...	...	...	...	...	...	...	0.10	...	0.29	...	...	0.13	157
	14	Laplace Ringlet IER	120036.53	...	...	...	...	...	...	0.13	...	0.74	0.61	2.22	1.19	...	0.27	...	...	0.20	168
	114	Laplace Gap OEG	120085.65	...	...	...	...	...	...	...	...	...	...	...	1.34	...	0.22	...	...	0.10	172
	11	Bessel Gap OEG	120243.71	...	...	...	...	...	...	...	...	...	0.14	0.20	0.64	...	0.23	...	...	0.23	169
	9	Barnard Gap OEG	120316.04	...	...	...	...	...	...	...	...	...	...	...	0.23	...	0.22	0.19[a]	...	0.11	161
	ID	Feature	a(km)	−3	−2	−1	0	*ae*	1	2	2_M	3	4	5	6	7	8	9	$a \sin i$	rms	N
Narrow Ringlet	560	Strange Ringlet IER	117907.04	...	...	−1	0	2.42	7.63	...	3.75	1.29	2.49	...	1.06	...	...	...	7.44	1.63	167
	100	Strange Ringlet COR	117907.73	0.86	0.96	0.59	2.47	7.53	...	3.79	1.52	2.33	...	1.05	...	...	...	...	7.15	1.60	179
	561	Strange Ringlet OER	117908.77	...	...	1.14	2.56	7.40	...	4.13	1.55	2.60	...	...	...	...	...	...	7.39	1.99	180
	ID	Feature	a(km)	*ae*	1	2	2_M	3	4	5	6	7	8	9	10	11	12	13	$a \sin i$	rms	N
OER/IEG	53	Huygens Ringlet OER	117823.65	28.03	...	1.54	1.84	...	...	0.71	...	...	...	...	...	...	...	...	0.58	1.50	183
			117823.68	29.72	3.89	2.02	1.78	...	...	0.55	...	...	...	...	...	...	...	...	0.51	0.97	183
	19	Herschel Gap IEG	118188.42	8.27	...	1.34	0.89	0.71	0.35	0.36	0.37	0.37	0.34	...	0.25	...	...	...	0.34	0.41	173
	17	Herschel Ringlet OER	118263.25	1.76	...	0.37	0.72	0.32	0.20	0.22	...	...	...	...	...	...	...	...	2.12	0.35	147
	123	Russell Gap IEG	118589.92	7.60	...	0.23	0.51	0.25	...	...	...	...	...	...	...	...	...	...	...	0.25	157
	120	Jeffreys Gap IEG	118929.63	3.26	...	...	0.44	...	...	...	...	...	...	...	...	...	...	...	0.17	0.13	93
	119	Kuiper Gap IEG	119401.67	0.93	...	...	0.25	...	...	...	...	...	...	...	...	...	...	...	0.18	0.16	137
	115	Laplace Gap IEG	119844.78	3.25	...	...	0.29	...	...	...	...	...	...	...	...	...	...	...	0.25	0.26	112
	12	Laplace Ringlet OER	120077.75	2.79	...	0.62	0.22	0.42	0.25	...	0.12	...	...	...	...	...	...	...	...	0.14	174
	127	Bessel Gap IEG	120231.17	1.78	...	...	0.29	...	...	...	...	...	0.36	...	...	...	...	...	...	0.44	170
	10	Barnard Gap IEG	120303.69	0.44	...	0.61	0.25	1.31	1.64	1.36[a]	0.59	0.55	0.30	0.71	0.42	...	...	0.36	...	0.43	161

[a] Prometheus 5:4 ILR; see Table 7.

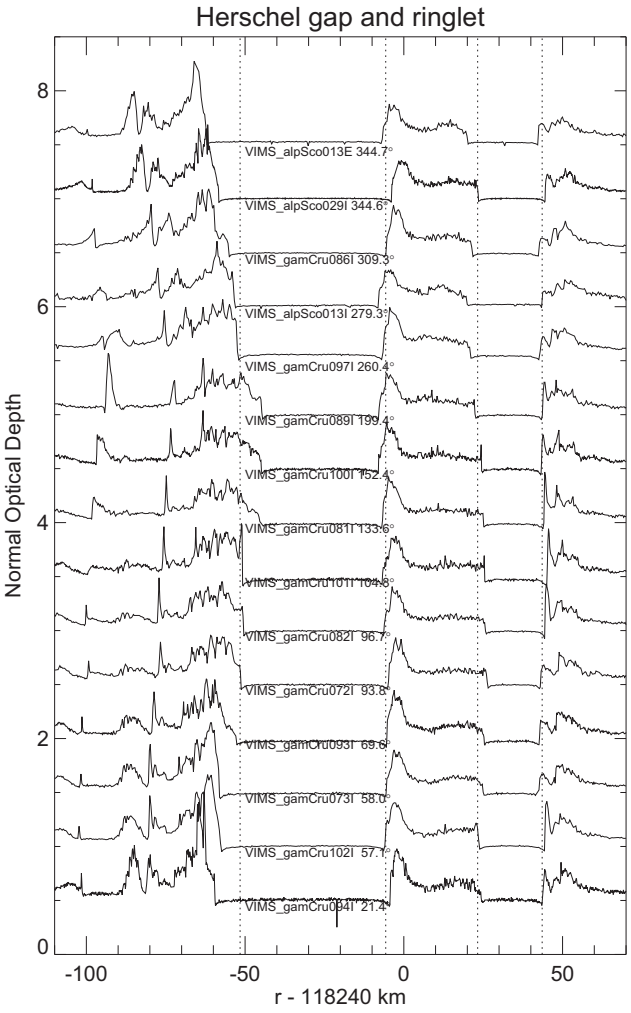

Fig. 19. Optical depth profiles for the Herschel gap and ringlet, derived from selected VIMS stellar occultation profiles. The profiles are offset vertically by a constant amount, and arranged (and labeled) in order of increasing true anomaly of the gap's inner edge. Vertical dotted lines indicate the mean radii of the inner and outer gap and ringlet edges, based on our orbital fits.

have encountered, with the largest post-fit rms residuals of all of the Cassini Division features. Evidently there are significant radial and/or vertical distortions that are not currently included in this multi-mode model.

Finally, we list the OER/IEG features. In this case, the agreement with the cavity mode model is exact: all detected edge modes are ILR-type modes, as expected. As before, the innermost of the features are the only ones with measurable inclinations, although there may be no dynamical significance to this pattern. With the exception of the Huygens ringlet, which has substantial unmodeled radial distortions, as noted previously, all of the OER/IEG features have post-fit rms residuals below 0.5 km. The inner edges of the Herschel and Barnard gaps each have an abundance of edge modes, while the inner edges of the Jeffreys, Kuiper, and Laplace gaps have no detected free normal modes at all, other than $m = 1$. There is a $m = 5$ mode at the Barnard gap IEG that is probably forced by the nearby Prometheus 5:4 ILR, as we discuss below in Section 8.2.

7.2. Systematic patterns in resonance locations and estimated mass densities

The resonant cavity model for normal modes requires that the resonant radii for each mode must lie within the ring material,

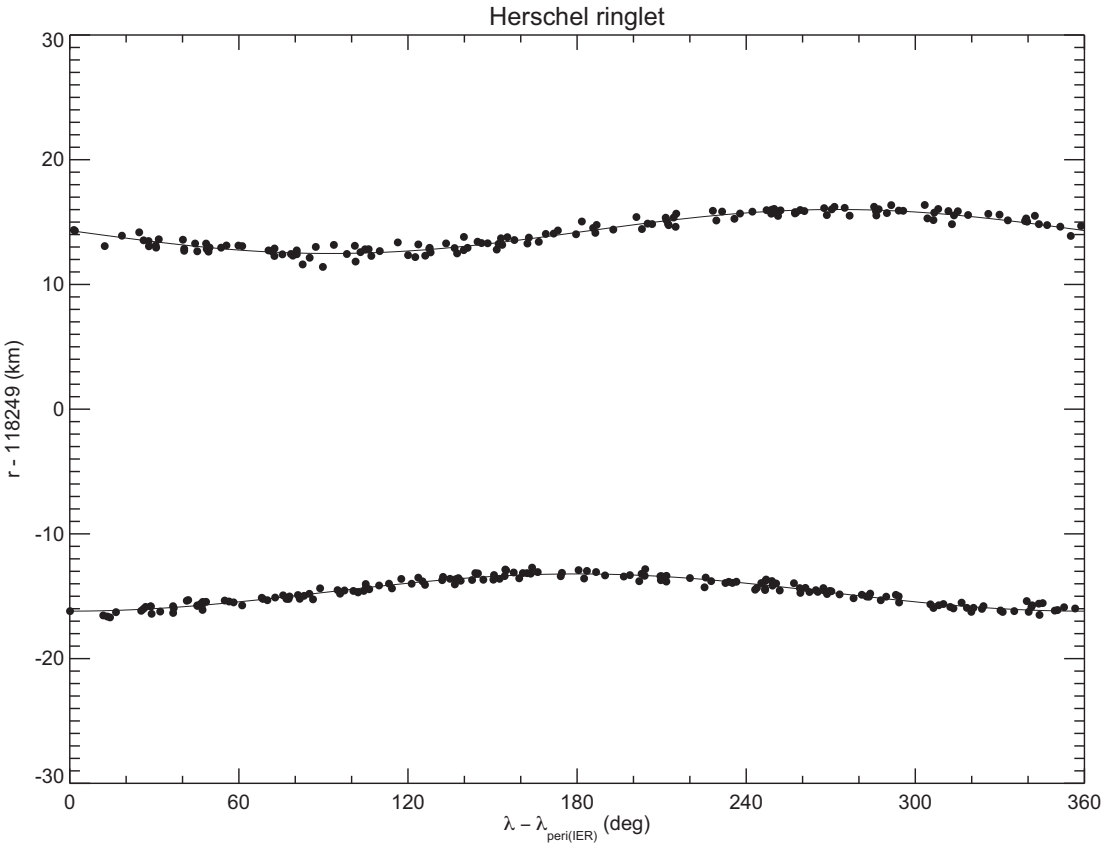

Fig. 20. The measured radii of the Herschel ringlet inner and outer edges, plotted as a function of longitude relative to the periapse longitude of the inner ring edge. The fitted $m = 1$ amplitudes are 1.5 km (IER) and 1.9 km (OER); other normal modes have not been subtracted (see Table 3). Note the phase offset of the outer edge relative to the inner edge of $\Delta\lambda = \varpi_{\rm OER} - \varpi_{\rm IER} = 95^\circ$.

and not in the adjacent gap. Thus, for IEG/OER features, we expect that $\Delta a_p = a_{\rm res} - a_{\rm edge} > 0$, and for OEG/IER features that $\Delta a_p < 0$. Furthermore, we expect that, within a ring with multiple normal modes, $|\Delta a_p|$ should systematically decrease with increasing $|m|$, since the wavelength of density waves scales as $|m-1|^{-1}$, for a given surface mass density (Shu et al., 1984). The calculated values of Δa_p are plotted for individual edges in Fig. 24, as a function of m. As predicted by the model, Δa_p is located within ring material, and not in free space, for every mode. Similarly, the expected trend of decreasing distance of the resonance from the ring edge with increasing $|m|$ is followed in almost every instance.

Encouraged by these trends, we can use the dispersion relation for density waves to estimate the surface mass density near the edges of features with multiple normal modes. As described in Nicholson et al. (2014a), the method assumes that the distance Δa_p between each mode's resonant radius and the ring edge is equal to 1/4 of the first wavelength of the corresponding density wave. Taking amplitude-weighted averages over the strongest free modes for a given edge, we obtain the nominal mean surface densities Σ listed in Table 6. Since this simple prescription underestimates the true surface density by about a factor of 4, based on numerical simulations by P. Goldreich (personal communication, 2013), we have included values for 4Σ as well, representing our best estimates of the actual surface densities. Finally, for the listed mean normal optical depth $\bar{\tau}$, we compute the mean opacity $\kappa = \bar{\tau}/4\Sigma$ for each feature.

For the Huygens and Laplace ringlets, we find quite reasonable agreement between the surface densities derived from the inner and outer edges: for the Huygens ringlet, $4\Sigma = 19.1$ and 14.5 gm cm^{-2}, and for the Laplace ringlet we find $4\Sigma = 12.6$ and 10.9 gm cm^{-2} for the inner and outer edges, respectively. The relatively low optical depth Huygens OEG and Herschel IEG and OEG have 4Σ =2.0, 3.0, and 1.2 gm cm^{-2}, respectively; the Barnard IEG has a somewhat larger value of 7.3 gm cm^{-2}. By means of comparison, Colwell et al. (2009a) estimated surface mass densities of Cassini Division features based on density wave analysis, including the 9:7 Pandora density wave in the Laplace ringlet. They obtained an estimated surface mass density of 5.76 gm cm^{-2}, roughly half the 4Σ value we find from the normal mode analysis, suggesting that the correction factor of 4 we have applied may be an overestimate. In the C ring, the Maxwell ringlet's mean surface mass density is estimated to be ~11 gm cm^{-2} from self-gravity estimates, comparable to a range of 5–12 gm cm^{-2}, inferred from the properties of the internal $m = -2$ wave present in the ringlet itself (French et al., 2016), and the Titan ringlet's surface density is estimated at 5.2–6.5 gm cm^{-2}, based on the resonance locations of multiple edge modes (Nicholson et al., 2014b).

7.3. Open questions

Every Cassini Division ring edge or gap that we have measured has a detectable eccentricity ($m = 1$) and forced $m = 2$ Mimas mode; nearly all have additional ILR- or OLR-type normal modes. This is in striking contrast to the situation in the C and B rings, where (with the exception of the narrow ringlets described in Nicholson et al., 2014b), near all sharp-edge features are circular and equatorial, with no detectable modes at the A_m ~0.1 km level. Most of these features are not bounded on one side by free space, but instead are embedded within regions of non-zero optical depth material, and it may be that normal modes are excited and persist

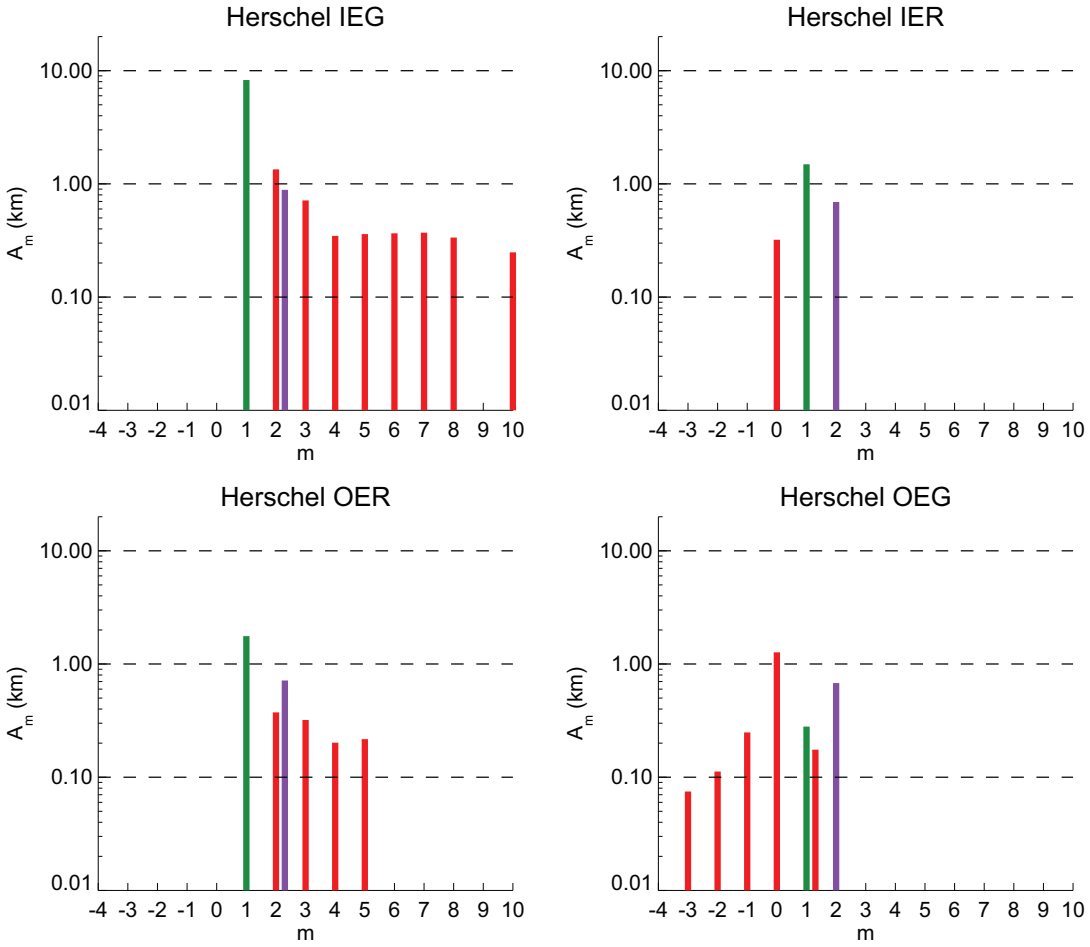

Fig. 21. Detected normal modes for the Herschel ringlet and gap edges. Modes are coded by color: free eccentric modes ($m = 1$) are green, other free modes are red, and modes forced by an external satellite (in this case, the $m = 2$ mode forced by Mimas) are violet. (For interpretation of the references to color in this figure legend, the reader is referred to the web version of this article.)

Table 6
Surface densities and opacities derived from normal modes.

Feature	a (km)	m values	Σ (g cm^{-2})	4Σ (g cm^{-2})	$\bar{\tau}$	$\kappa (= \bar{\tau}/4\Sigma)$ cm^2 g^{-1}
Huygens IER	117806	$-2, -3, -4, -5$	4.8	19.1	3.0	0.16
Huygens OER	117824	2, 5	3.6	14.5	3.0	0.21
Laplace IER	120037	$0, -1, -2$	3.1	12.6	0.7	0.06
Laplace OER	120078	2, 3, 4	2.7	10.9	0.7	0.06
Huygens OEG	117931	$0, -1, -3, -4$	0.5	2.0	0.2	0.10
Herschel IEG	118188	2, 3, 4, 5, 6, 7, 8, 10	0.8	3.0	0.4	0.13
Herschel OEG	118284	0	0.3	1.2	0.3	0.25
Barnard IEG	120304	2, 3, 4, 6, 7, 9	1.8	7.3	0.4	0.05

only near free-space boundaries such as isolated ringlet edges or true gap edges. This is consistent with the resonant cavity model for normal modes described in detail in Section 2 of Nicholson et al. (2014b), but it does not account for which specific edges and gaps contain strong normal modes.

Although the general pattern of ILR- and OLR-type normal modes agrees with theoretical expectations, and the trend of A_m with distance from ringlet and gap edges seems largely consistent with the resonant cavity model, we are left with a number of vexing questions. What characteristics determine which ring features are most or least likely to harbor normal modes? What governs the specific selection of modes? Are there saturation mechanisms that limit their amplitudes? What are their lifetimes?

We can gain some insight into the formation and destruction timescale for normal modes from an examination of the change in character of the outer edge of the A ring when Janus exchanges its orbital position as part of the Janus/Epimetheus coorbital swap. From *Cassini* imaging data, El Moutamid et al. (2016) found that the $m = 7$ pattern driven by Janus when in its outer orbit had disappeared within two years of the coorbital swap, and in the interim free ILR-type normal modes with $m = 9$ and 12 appeared de novo in both imaging and occultation data.

As a separate experiment, we subdivided our occultation data sets into separate time periods to explore whether any modes have appeared or disappeared over the eight or so years of observations, but we were not able to reach any statistically significant conclusions from these tests.

8. Resonant perturbations in the Cassini Division

In contrast to the adjacent A ring, the Cassini Division is host to a relatively small number of first- or second-order satellite

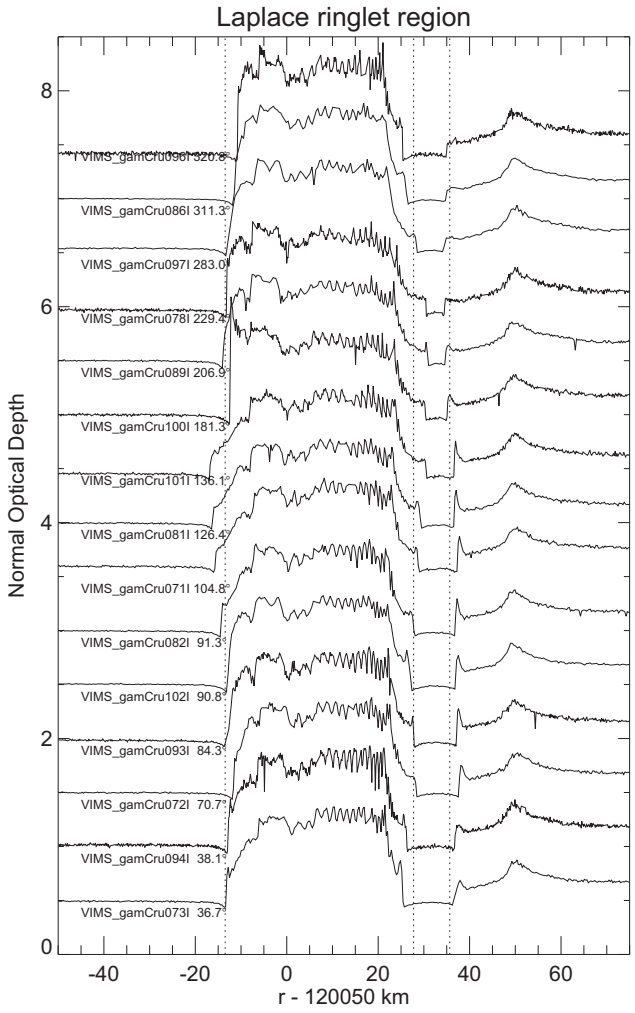

Fig. 22. Optical depth profiles for the Laplace ringlet located within the Laplace gap, derived from selected VIMS stellar occultation profiles. The profiles are offset vertically by a constant amount, and arranged (and labeled) in order of increasing true anomaly of the eccentric outer edge. Vertical dotted lines indicate the mean radii of the inner and outer ringlet edges, and the outer edge of the Laplace gap, based on our orbital fits.

resonances. Other than the Mimas 2:1 resonance that falls near the inner boundary of the Cassini Division at the B ring's outer edge, the only significant resonances in the Cassini Division are the first-order Pandora 6:5 and 7:6, the Prometheus 5:4, and the Atlas 5:4 ILRs, and the second-order Prometheus and Pandora 9:7 ILRs. Colwell et al. (2009a) analyzed density waves in the Cassini Division associated with several of these resonances, and inferred the surface mass density, viscosity, and opacity of the ring material in these regions from the dispersion and damping of the density waves. Here, we use the results of our orbit fits to the edges of sharp features to explore resonant perturbations in the Cassini Division.

8.1. The $m = 2$ Mimas mode

The inner edge of the Cassini Division is also the B ring's outer edge, which is strongly perturbed by the nearby Mimas 2:1 ILR. It is not surprising, then, that the response of Cassini Division ringlets and gaps to this resonance is detectable over a significant radial range. Indeed, we have identified statistically significant perturbations for every measured feature in the Cassini Division. Moreover, the amplitude, phase, and pattern speed of the forced $m = 2$ modes are in excellent agreement with theoretical expectations, as shown in Fig. 25. In the top panel, we compare the fitted mode amplitudes from Table 5 with the predictions of a simple model for a test particle perturbed by this resonance (Goldreich and Tremaine, 1982; Spitale and Hahn, 2016). Numerically, we compute a theoretical resonance strength $\mathcal{S} = 466$ km^2, and a corresponding forced $m = 2$ amplitude at radius a of $A_{2M} = \mathcal{S}/|a - a_{\rm res}|$, where $a_{\rm res}$ is the resonance radius (117570 km). The agreement is quite satisfactory. As further evidence of the reality of these detections, note that the apoapses of the edge perturbations are approximately aligned with Mimas, as expected for orbits exterior to the ILR. Furthermore, all fitted pattern speeds match Mimas's mean motion in 2006–2010, as shown in the third panel of the figure.

This is the second reported instance in Saturn's rings in which an ILR of an external satellite creates detectable systematic regional perturbations in the shapes of sharp features: Titan's strong 1:0 ILR similarly introduces forced $m = 1$ perturbations in more than two dozen features located throughout the inner C ring. In both cases, detectable perturbations up to 3000 km from the resonance location (see Fig. 19 of Nicholson et al., 2014a).

Table 7
Barnard Gap resonance models.

Feature	Barnard IEG	Barnard OEG
Resonance	Prometheus 5:4 ILR	Prometheus 5:4 ILR
m	5	5
a (km)	120303.69 ± 0.05	120316.04 ± 0.01
$a_{\rm res}$ (km)	120304.0	120304.0
$\Delta a_{\rm res}$ (km)	−0.31 ± 0.05	12.04 ± 0.01
$n_{\rm Prom}$ (° d^{-1})	587.28379	587.28379
Ω_P (° d^{-1})	587.28565 ± 0.00088	587.28403 ± 0.00103
$\Delta\Omega_P$ (° d^{-1})	0.00186 ± 0.00088	0.00024 ± 0.00103
δ_m(°)[a]	27.61 ± 0.57	58.97 ± 0.87
$\lambda_{\rm Prom}$(°)[a]	22.91	22.91
$\Delta\delta_m$(°)	4.70 ± 0.57	36.06 ± 0.87
$\mathcal{S}$ (km^2)	2.12	2.12
$A_{\rm pred}$ (km)	6.84	0.18
A_m (km)	1.36 ± 0.06	0.19 ± 0.01

[a] At epoch 2008 January 1, 12:00:00 UTC = JD 2454467.0.

8.2. The Prometheus 5:4 resonance at the Barnard Gap

As we have noted previously, the inner edge of the Barnard Gap lies very close to the resonance radius for the Prometheus 5:4 ILR, which may result in resonant forcing of an $m = 5$ mode of the edges of this gap. Indeed, an $m = 5$ signature is present among the rich set of other ILR-type modes detected for the Barnard IEG. There is also a weaker $m = 5$ ILR-type mode on the *outer* edge of the gap, where we would normally expect to find only OLR-type modes. **Fig. SM-11** shows the normal mode scans for both modes, and in particular provides clear indications of an ILR-type $m = 5$ edge mode with an amplitude of just 0.19 km. Here, we evaluate the evidence that these modes are forced by Prometheus.

In Table 7, we list for both inner and outer gap edges the best-fitting semimajor axis a and observed $m = 5$ mode amplitude A_m, pattern speed Ω_P, and phase δ_m, and the key properties of the forced resonance, including its predicted strength $\mathcal{S}$. We also list the corresponding differences between the observed and predicted pattern speed $\Delta\Omega_P$ and orientation $\Delta\delta_m$. For the predicted phase, we assume that the pericenter of the $m = 5$ distortion is aligned with aligned with Prometheus, as expected for an orbit located interior to $a_{\rm res}$.

For the $m = 5$ mode at the inner edge, the agreement between the observations and the forced resonance model is quite satisfactory: the pattern speed differs by only 0.00186° d^{-1} from Prometheus's mean motion, and the pericenter orientation is less

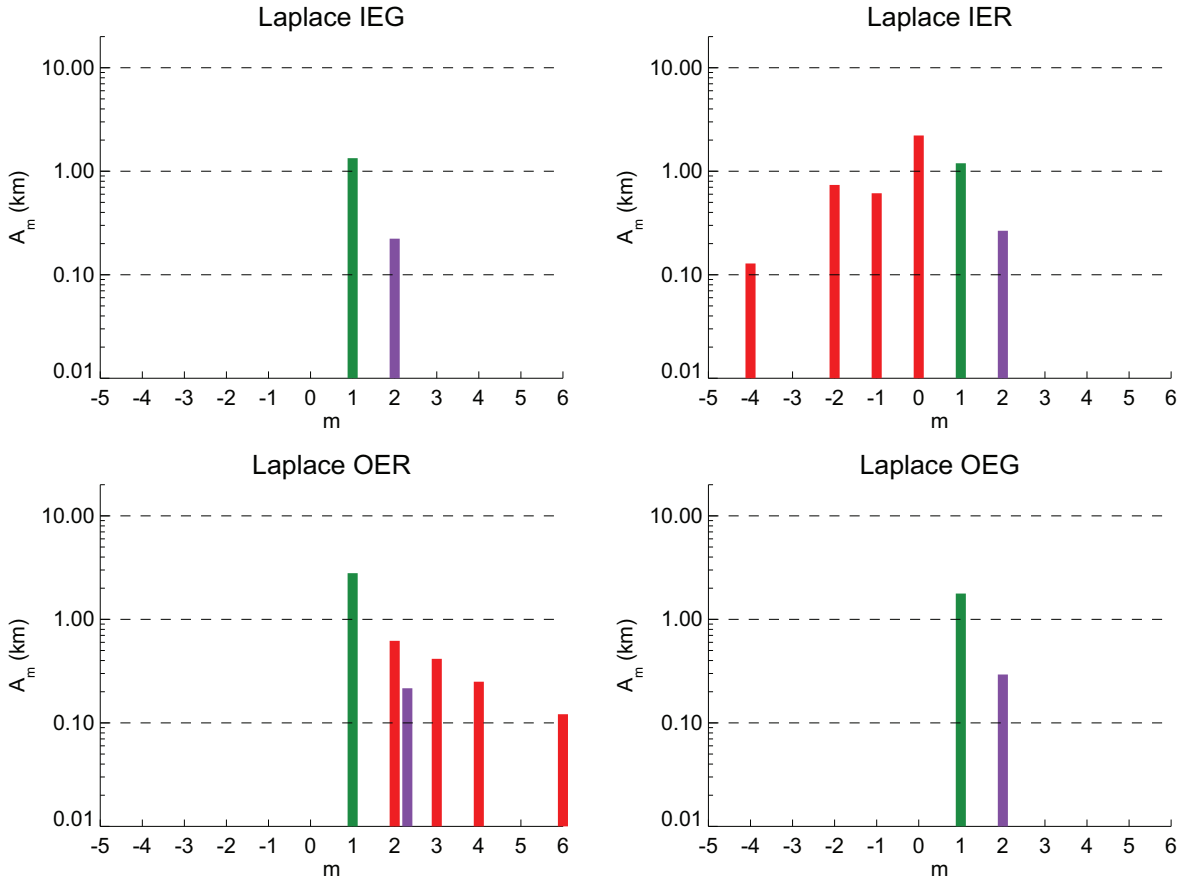

Fig. 23. Detected normal modes at the edges of the Laplace gap and ringlet. Modes are coded by color: free eccentric modes ($m = 1$) are green, other free modes are red, and modes forced by an external satellite (in this case, the $m = 2$ mode forced by Mimas) are violet. (For interpretation of the references to color in this figure legend, the reader is referred to the web version of this article.)

than 5° from the direction to Prometheus. These differences do exceed the quite small formal errors of the orbit fit, but these geometrical agreements support the idea that the $m = 5$ mode is forced, rather than free. The observed amplitude $A_m = 1.36$ km, however, is much smaller than the predicted value of 6.84 km. Nominally, we find that the gap edge is only 0.31 km from the resonance location, but the uncertainty in the absolute radius scale is comparable to this value, making the predicted amplitude itself uncertain by about a factor of two. Furthermore, linear theory probably fails when $\Delta a_{\rm res} \lesssim \mathcal{S}^{1/2}$ (i.e., $\mathcal{S}/\Delta a_{\rm res} \gtrsim \Delta a_{\rm res}$) because of streamline crossing in the ring. We note that similar disagreements were found for three forced resonant perturbations in the C ring: the pattern speeds and orientations of the fitted modes for the Titan 1:0 ILR, the Prometheus 2:1 ILR at the Bond OER, and the Mimas 3:1 ILR at the Dawes IEG matched those of the putative forcing satellites quite well, whereas the amplitudes of the modes differed more substantially from the predictions of the test particle model (see Table 7 of Nicholson et al., 2014b).

The $m = 5$ mode on the outer gap edge is at first glance a bit more perplexing, since we generally expect only OLR-type modes for such features. In this instance, however, we have compelling evidence that the mode is forced by Prometheus: its pattern speed differs by only $0.00024 \pm 0.00103^\circ\,{\rm d}^{-1}$ from the predicted value, and the observed amplitude, $A_m = 0.19 \pm 0.01$ km, while very small, matches almost exactly the predicted amplitude of 0.18 km. Furthermore, the observed phase difference between the mode's pericenter and the mean longitude of Prometheus, $\Delta\delta_m \simeq 36^\circ$, corresponds to a phase difference of $5 \times 36^\circ = 180^\circ$ from periapse when measured along a single lobe of the 5-lobed edge distortion, just as expected for orbits outside of the satellite's resonance radius. A similar change of 180° in the orientation of the perturbation from inside to outside the Titan 1:0 ILR resonance radius is seen for a host of C ring gap edges, as shown in Fig. 19 of Nicholson et al. (2014b).

9. Eccentric gap and ringlet edges

In Fig. 8 above we illustrated the radius variations associated with the $m = 1$ modes on the edges of the five simple gaps in the Cassini Division. A similar gallery of plots for the three complex gaps and their embedded ringlets is presented in Fig. 26. In this section, we examine regional patterns in the eccentricities and precession rates of non-circular gap and ringlet edges.

9.1. Eccentricities

In Fig. 27 we plot the $m = 1$ mode amplitudes, for all sharp-edged features in the Cassini Division that show a detectable eccentricity, vs their distance from the outer edge of the B ring. The largest eccentricities are found for the Huygens ringlet ($ae = 28$ km) and the B ring's outer edge (21 km, see Nicholson et al., 2014a), while the smallest definitely non-zero values are those of the inner edges of the Kuiper gap (0.9 km) and the Laplace ringlet (1.2 km). As noted by Hedman et al. (2010), the eccentricities generally decrease with increasing radius (or distance from the B ring edge), though the trend is not monotonic.

Most of the features in Fig. 27 are inner gap edges (IEGs); only two outer gap edges show measurable eccentricities in our fits:

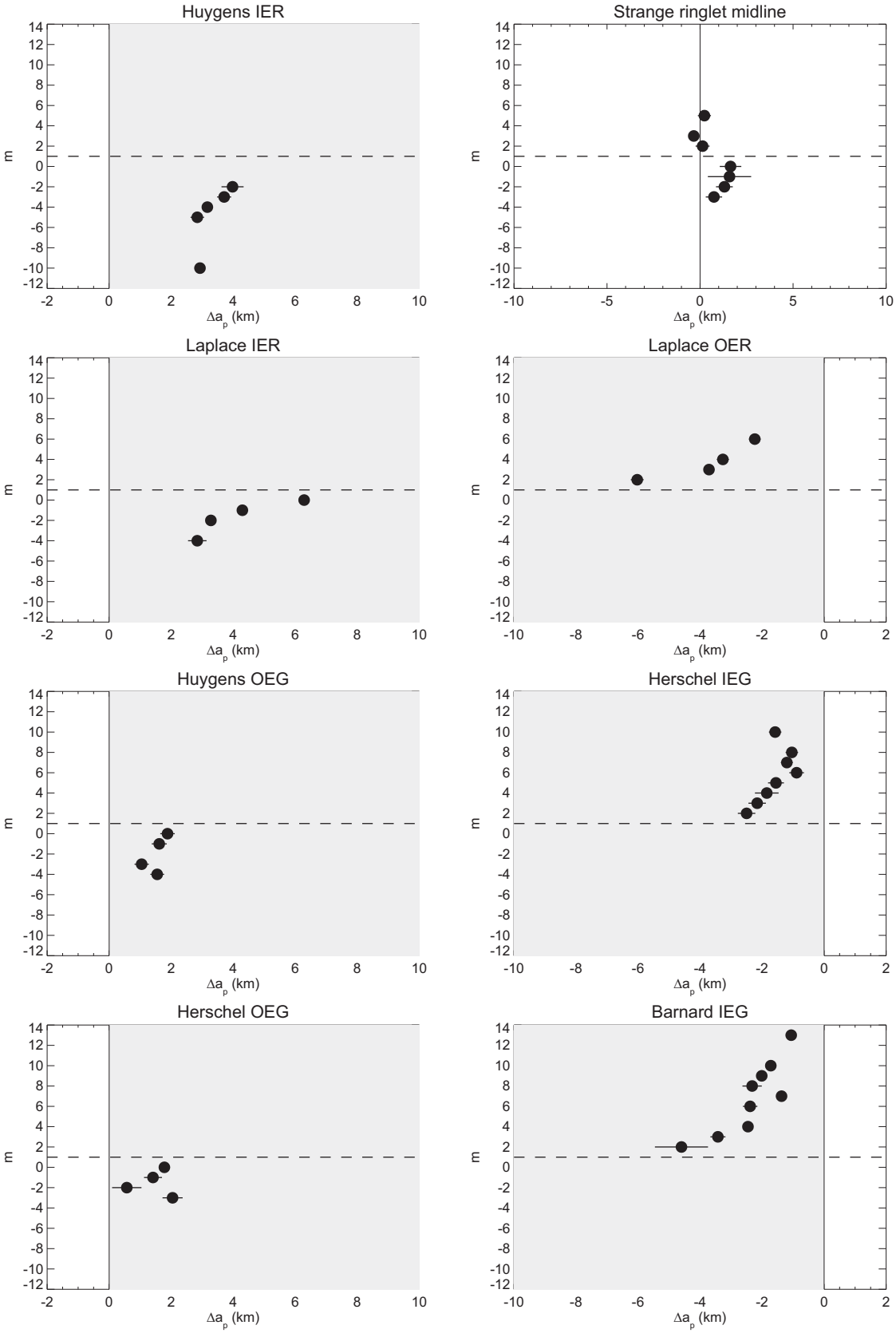

Fig. 24. The locations of calculated normal mode resonant radii relative to selected ringlet and gap edges in the Cassini Division. For each edge, the value of Δa_p is plotted vs m, with negative values of the latter indicating OLR-type modes. Vertical lines denote ringlet or gap edges, and shading indicates the presence of ring material. Resonantly forced modes ($m = 2$ Mimas modes and the $m = 5$ Prometheus 5:4 ILR at the Barnard gap inner edge) and $m = 1$ keplerian perturbations are excluded. Note that the magnitude of Δa_p generally decreases with increasing $|m|$. The Strange ringlet (upper right panel) is a special case: It is so narrow that even the $m \neq 1$ modes span the entire ringlet, and are best considered to be global modes, rather than edge modes.

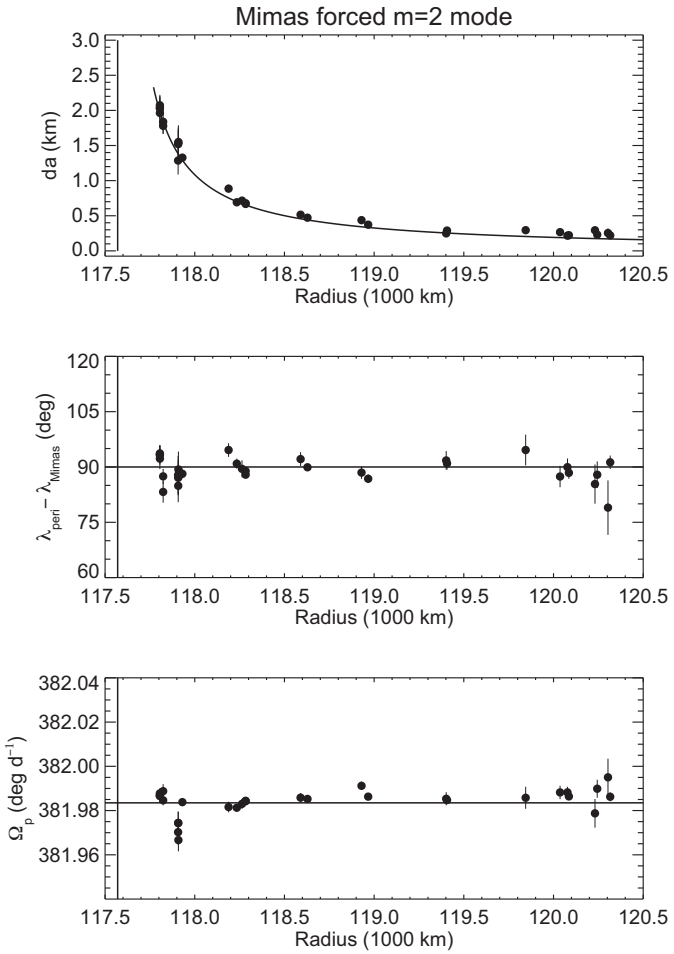

Fig. 25. Amplitude, phase, and pattern speed of the forced $m = 2$ Mimas mode vs radius, from the orbit fits summarized in Table 5. The curve in the upper panel shows the predicted amplitude falling inversely with distance from the resonance, based on a simple test-particle model and a calculated resonance strength $\mathcal{S} = 466$ km^2. The second panel shows that the fitted periapses of the forced normal mode are very close to 90° from Mimas's longitude, as expected for orbits exterior to an ILR. All signatures have pattern speeds very close to Mimas's mean motion in 2006-2010, as indicated by the solid line in the third panel.

those of the Huygens and Laplace gaps, and these are noticeably smaller than the eccentricities seen on their inner edges. A third outer gap edge—the Herschel gap—is not eccentric but shows a definite $m = 0$ normal mode. It is probably not a coincidence that all three of these gaps contain embedded ringlets. By contrast, of the five simple gaps, only the Bessel gap shows a measurable perturbation on its outer edge, and this has an amplitude of only 0.6 km. (Here, we are excepting the ubiquitous $m = 2$ modes forced by the Mimas 2:1 resonance.)

9.2. Precession rates

In Fig. 28 the fitted apsidal precession rates for the same features shown in Fig. 27 are plotted vs semimajor axis, along with the rates calculated from the best current estimates for Saturn's zonal gravity coefficients (Jacobson et al., 2006). Hedman et al. (2010) pointed out that, starting with the outer edge of the B ring and going out to the inner edge of the Bessel gap, there are eight eccentric features (or groups of nearby features with similar apsidal rates) that form a quasi-regular sequence in their apsidal precession rates, with an average interval of $\delta\dot{\varpi} = 0.06°\,\mathrm{d}^{-1}$. They proposed further that this common interval may match the libration frequency of the dominant $m = 2$ mode on the outer edge of the B ring, and suggested that the Cassini Division gaps may have formed at a series of three-body resonances with the B ring edge. Subsequent work, however, has established that the $m = 2$ perturbation on the B ring circulates rather than librates, and that its circulation frequency is $0.182°\,\mathrm{d}^{-1}$ (Nicholson et al., 2014a; Spitale and Porco, 2010), or about three times greater than the libration frequency estimated by Hedman et al. (2010). This calls into question the viability of the three-body resonance model.

The regular intervals between neighboring gap edges are quite apparent in Fig. 28, with the large interval between the B ring edge and the inner edge of the Herschel gap being filled by the co-precessing edges of the Huygens ringlet. (Following Hedman et al., 2010, we group the eccentric Herschel ringlet along with its inner gap edge and do likewise for the Laplace ringlet.) Excluding the two eccentric outer gap edges, we find that the intervals between neighboring edges in this sequence vary from 0.043 to $0.068°\,\mathrm{d}^{-1}$, with a characteristic spacing of $\sim 0.06°\,\mathrm{d}^{-1}$. Given the regular sequence of precession rates, Nicholson et al. (2014) studied the corresponding pericenter distribution over time, in search of an underlying resonant relation of the kind suggested by Hedman et al. (2010). Exploring this idea further, we investigated whether or not there is a recent (or future) epoch at which all (or a significant subset) of these eight eccentric edges are co-aligned. Unfortunately, the answer is no, at least over a period of 200 years centered on the Cassini epoch. (Over longer periods, the uncertainties in the fitted precession rates make such an exercise increasingly meaningless.) The closest grouping is in mid-2051, when the rms scatter in ϖ is reduced to 24°. If the criterion for alignment is relaxed to include cases of anti-alignment (i.e., $\delta\varpi \simeq 180°$), then the tightest grouping is in early 1933, when the rms spread in $\sin(\delta\varpi)$ is reduced to 0.267, corresponding to a scatter of 16°. Similar searches for groupings modulo 90° or 60° do not yield anything closer.

9.3. Anomalous precession rates

In the middle panel of Fig. 28 we plot the residual precession rates, after subtracting the predicted values due to Saturn's zonal gravity coefficients $J_2 - J_{10}$ (Jacobson et al., 2006). Most noticeable here is that *all* the residuals are positive, except for the Strange ringlet ($a = 117907$ km). This is in contrast to the situation in the C ring, where the precession rates of the Maxwell and Titan ringlets were found to be very close to their predicted values (Nicholson et al., 2014b), and in the case of the resonantly-forced Titan ringlet, the resonant radius deduced from the observed eccentricity closely matches the predicted location. In general, we may attribute these excess rates to gravitational perturbations from the nearby B ring; the dot-dashed curve in the figure shows the secular contribution to the apsidal rates in this region for a nominal uniform surface mass density of $\Sigma = 100$ g cm^{-2}. Although the match is by no means perfect, suggesting that additional perturbations may be involved in some cases, this does provide a reasonable fit to the general trend of the observed residuals.

Three features, however, stand out by virtue of their very large residuals, or anomalous precession rates: the outer edges of the Huygens and Laplace gaps and the outer edge of the Laplace ringlet, all of which exceed their predicted rates by at least $0.03°\mathrm{d}^{-1}$. Slightly less prominent, but also troublesome, are the Bessel gap's inner edge and the Laplace IER. All other edges show residuals less than $0.01°\mathrm{d}^{-1}$, or $< 0.2\%$. The worst offenders are associated with two of the three complex gaps, and we suspect that perturbations by the opaque, embedded ringlets might be responsible. However, each gap/ringlet combination seems to be unique, so we will discuss each in turn.

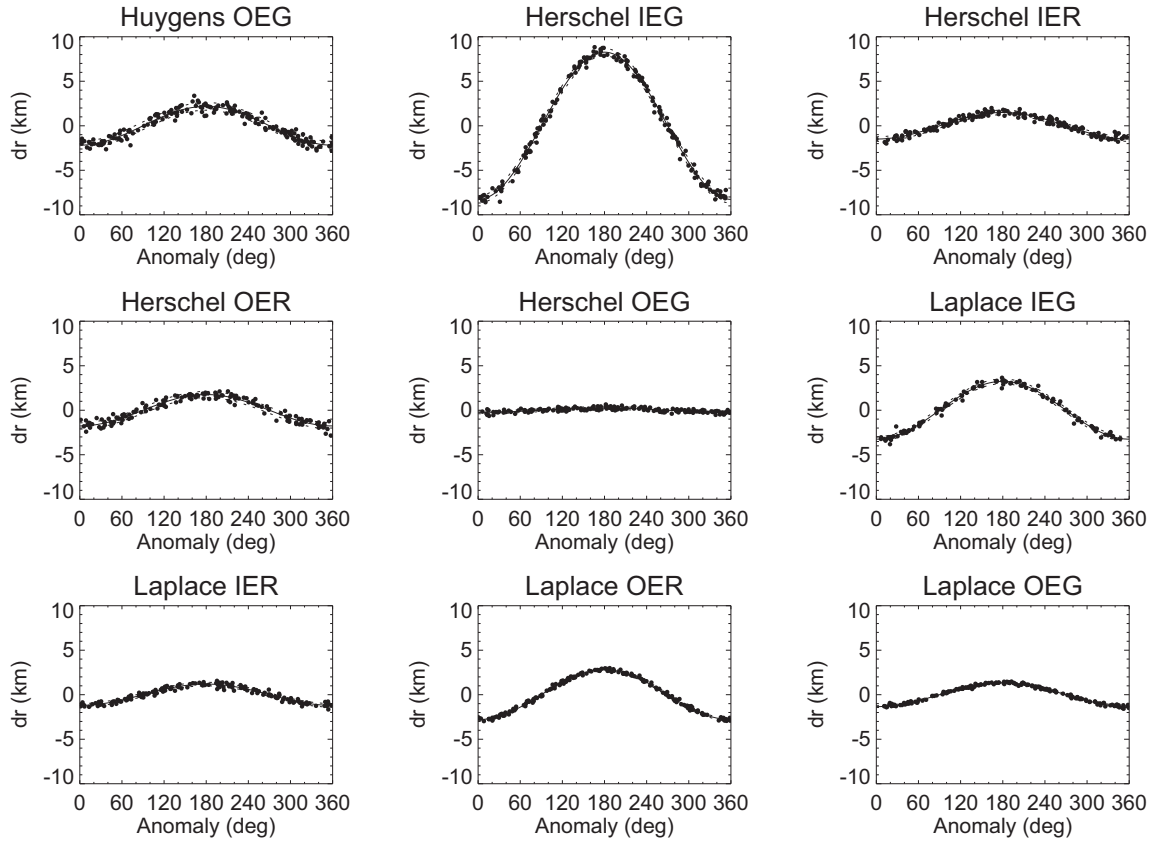

Fig. 26. A gallery of $m = 1$ models and residuals vs true anomaly for the three complex gaps in the Cassini Division, and the eccentric edges of the Herschel and Laplace ringlets. Fit parameters are given in Tables 2–4. Note the non-zero eccentricities of the three OEGs, unlike the nearly circular edges of the simple gaps shown in Fig. 8. Normal modes have been removed, when present.

9.3.1. The Huygens gap and ringlets

While the Huygens and Strange ringlets have mean precession rates only slightly larger than those expected, that of the gap's outer edge is substantially faster. In fact, it is faster than that of either ringlet. Expressed in terms of the offset between the effective radius at which $\dot{\varpi}_{sec} = \dot{\varpi}(\text{fit})$ and the actual semimajor axis of the edge, we find that $\Delta a_{\dot{\varpi}} = -201 \pm 11$ km for the OEG (see Table 2). The fitted rate of $5.0348 \pm 0.0017^\circ\,\text{d}^{-1}$ is in fact quite close to that of the Huygens ringlet (5.0285–$5.0303^\circ\,\text{d}^{-1}$), and we might be tempted to conclude that the modest eccentricity of the gap edge is forced by the much larger eccentricity of the ringlet. However, the corresponding pericenter longitudes at epoch ϖ_0 differ by over 100°, which makes this situation unlikely to be true. Note that both rates are significantly slower than the observed pattern speed of the $m = 1$ mode at the edge of the B ring, which is $5.081 \pm 0.006^\circ\,\text{d}^{-1}$ (Nicholson et al., 2014a), so it seems unlikely that either is being directly influenced by the B ring edge.

9.3.2. The Herschel gap and ringlet

If we compare the apsidal precession rates of the three edges in the Herschel gap with significant $m = 1$ signatures in Table 3, we find that the inner ringlet edge and inner gap edge have very similar values of $4.962^\circ\,\text{d}^{-1} < \dot{\varpi} < 4.974^\circ\,\text{d}^{-1}$, whereas the inner and outer edges of the ringlet exhibit statistically significant differential precession. On this basis, as noted in Section 5 above, the Herschel ringlet does not precess as a unit like most other eccentric ringlets, and perhaps should not be classified as such. (We note also that the pericenters of the ringlet's inner and outer edges differ by 92°, at our epoch of 1 January 2008.) Taken together with the fact that the eccentricity of the inner gap edge is much larger than that of the ringlet, we are again tempted to conclude that the eccentricity of the inner edge of the ringlet is being forced by that of the inner gap edge, while the outer edge of the ringlet is behaving independently. In this case, this inference is supported by the further observation that the pericenter longitudes of the inner gap and ringlet edges differ by almost 180°, as expected where an eccentric inner orbit forces an outer one (Nicholson et al., 2014b).

9.3.3. The Laplace gap and ringlet

With the Laplace gap and its ringlet, we are presented with a puzzling situation: From Table 4, we see that the inner gap edge and the outer ringlet edge have very similar precession rates, with $4.725^\circ\,\text{d}^{-1} < \dot{\varpi} < 4.727^\circ\,\text{d}^{-1}$, whereas the less-eccentric inner edge of the ringlet is significantly slower at $4.713 \pm 0.001^\circ\,\text{d}^{-1}$, and very similar to the outer gap edge rate of $4.717 \pm 0.001^\circ\,\text{d}^{-1}$. The apse rates of the two ringlet edges differ by many times their formal errors, and once again, we have what appears to be an eccentric ringlet that does not rigidly precess. Furthermore, we see that the pericenter longitudes of the inner and outer gap edges are almost identical, but differ from that of the ringlet's co-precessing outer edge by ~100°. We are at a loss to offer an explanation for this situation, but suspect that the similarity of the apsidal rates and pericenters of the gap edges is too close to ascribe to chance. Given the larger eccentricity of the inner gap edge, and the fact that its precession rate is much closer to the predicted value $\dot{\varpi}_{sec}$, it would appear that the eccentricity of the outer gap edge is being forced by that of the inner edge. But this is rather surprising, given the much higher optical depth, and presumably higher surface mass density, adjacent to the outer edge (see Fig. 1).

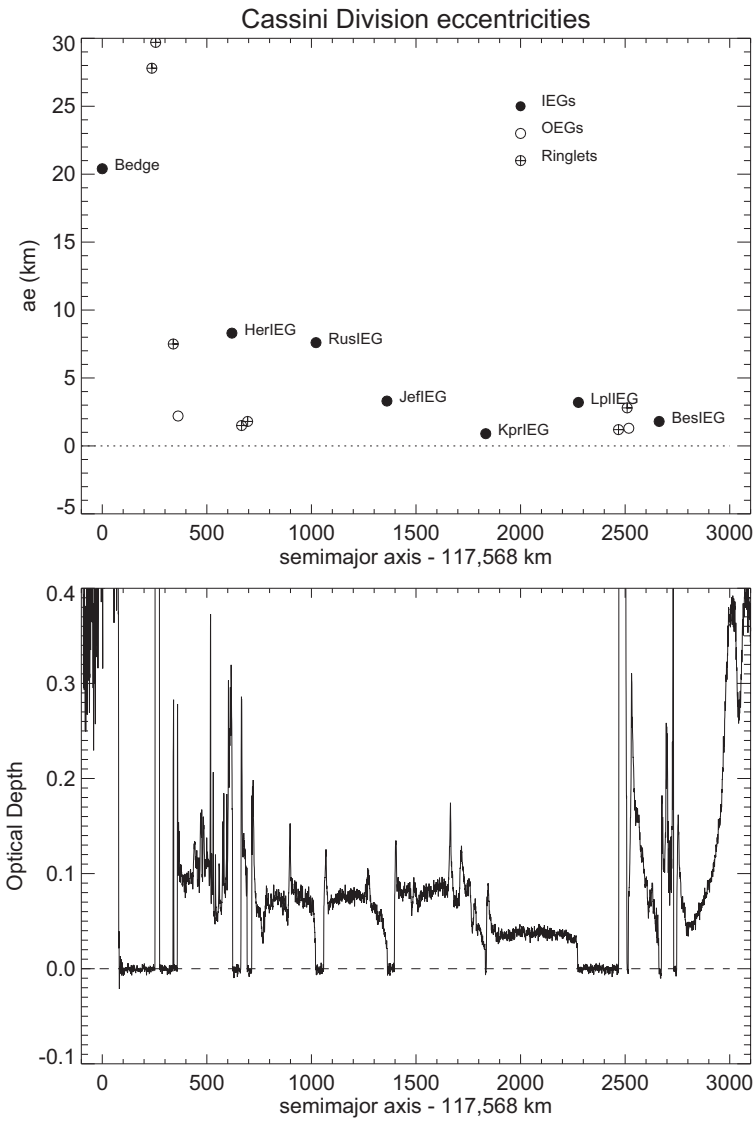

Fig. 27. Upper panel: Fitted eccentricities (i.e., $m = 1$ mode amplitudes) for clearly non-circular features in the Cassini Division, as a function of semimajor axis. Filled circles denote the inner edges of gaps (IEGs), which account for the majority of eccentric edges, while open circles denote the outer edges (OEGs) of the Huygens and Laplace gaps. Earth symbols indicate the edges of the four eccentric ringlets: Huygens, Strange, Herschel and Laplace. Lower panel:Optical depth profile, for context.

10. Conclusions

We have conducted a comprehensive survey of sharp-edged ringlets and gaps in the Cassini Division of Saturn's rings, making use of nearly 200 high-SNR stellar and radio occultation chords obtained by the *Cassini* VIMS, UVIS, and RSS instruments between 2005 and 2013. The high quality of the observations enables us to establish an absolute radius scale for the rings with an estimated accuracy of 0.25 km, and to determine the orbital elements of 22 Cassini Division ringlets and gap edges with remarkable precision. The results reveal an extraordinary richness in the shapes of these features, with eccentricities from as small as $ae = 80$ m to nearly 30 km, free normal modes (both global and edge modes) with amplitudes from ~ 0.1 to 4.1 km, and detectable inclinations as small as $a \sin i = 0.2$ km. Throughout the entire region, the forced Mimas 2.1 ILR produces systematic $m = 2$ distortions that quantitatively match the expected amplitudes, phases, and pattern speed.

The narrow Russell, Jeffreys, Kuiper, Bessel, and Barnard gaps are simplest in structure, and do not contain dense ringlets. The outer edges of these gaps are generally quite sharp and four of them are circular to within ~0.25 km, whereas most of the inner gap edges have lower contrast and have significant eccentricities, although in most cases we find evidence for additional normal modes. The Barnard gap falls very near to the Prometheus 5:4 ILR, and we find statistically significant $m = 5$ patterns on both the inner and outer edges of the gap with measured pattern speeds consistent with the mean motion of Prometheus, as expected for a forced mode. The periapses of the modes at the inner/outer gap edges are nearly aligned/antialigned with Prometheus, providing supporting evidence a resonant interaction with this small satellite.

Three Cassini Division gaps are more complex, containing one or more isolated ringlets: the Huygens, Herschel, and Laplace gaps. The Huygens gap is 361 km wide and its outer edge has a significant eccentricity $ae = 2.2$ km and four OLR-type normal modes with amplitudes from 0.3 to 1.8 km. The gap also contains two prominent ringlets. The first of these—the Huygens ringlet—is unique among eccentric ringlets in having nearly identical (and substantial) eccentricities on the two edges, in addition to a host of OLR-type normal modes on the inner edge and two ILR-type

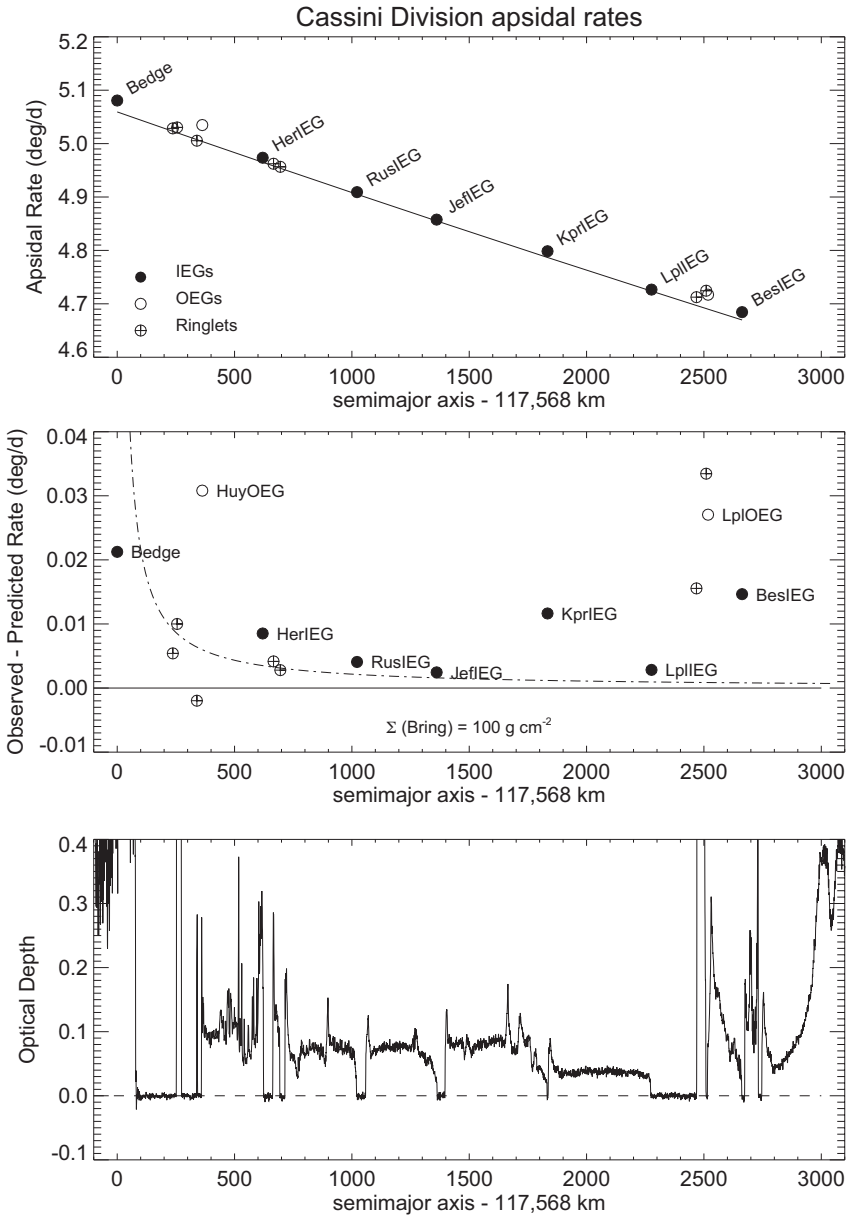

Fig. 28. Upper panel: Fitted apsidal precession rates vs mean radius for the eccentric features shown in Fig. 27. Symbols are as in that figure. Note the quasi-regular sequence in the precession rates for the gap inner edges, as first noted by Hedman et al. (2010). The solid line shows the predicted precession rates, calculated from Saturn's zonal gravity coefficients $J_2 - J_{10}$. Middle panel: The differences between the fitted and calculated precession rates in the upper panel, using the same symbols. The dot-dashed curve shows the contribution to the apsidal precession rates from the nearby B ring, assuming a uniform surface mass density of 100 g cm^{-2}. Lower panel: Optical depth profile, for context.

modes on the outer edge. We also see evidence for a secondary $m = 1$ (eccentric) mode on the outer edge of the ringlet, with a pattern speed similar to that of the B ring outer edge. It is possible that this mode is forced by the B ring itself. The ringlet has a small but measurable inclination, as do several of the other ringlets in the Cassini Division. Variations in the width of the Huygens ringlet are complex, but statistically are consistent with the expected magnitudes resulting from the random superposition of the multiple normal modes on the two edges. The occultation data do not provide independent or supporting evidence for the suggestion that embedded satellites produce long-term radial distortions in the inner edge shape that rotate at the keplerian rate of the ringlet (Spitale and Hahn, 2016). Also present in the Huygens gap is the so-called Strange ringlet, with a substantial eccentricity of $ae = 7.5$ km and inclination of $a \sin i = 7.1$ km, as well as both ILR- and OLR-type normal modes. Of all of the Cassini Division features, the Strange ringlet has the largest post-fit rms residuals (1.6 km), far greater than the typical measurement uncertainty of 0.2 km, indicative of significant unmodeled distortions in its radial shape and/or vertical variations.

The 100 km-wide Herschel gap's inner edge has one of the largest eccentricities in the Cassini Division, with $ae = 8.3$ km, and at least seven ILR-type normal modes with amplitudes from 0.2 to 1.3 km. The outer gap edge is also eccentric, and hosts four OLR-type normal modes with amplitudes from 0.1 to 1.3 km, with strong evidence for a secondary $m = 1$ mode with a pattern speed quite close to that of the B ring's outer edge, raising the possibility that the B ring itself may drive this mode. Both gap edges are weakly but measurably inclined, with $a \sin i = 0.25 - -0.34$ km. The Herschel ringlet itself is eccentric and inclined, but neither the

pericenters nor the nodes are well-aligned, raising questions about whether the Herschel ringlet can be regarded as a dynamically coherent eccentric ringlet.

The third of the complex gaps is the 241 km-wide Laplace gap, containing the Laplace ringlet. Both gap edges are eccentric, with very similar pericenter longitudes and apsidal precession rates for two edges, in spite of their large radial separation. The Laplace ringlet itself has eccentric edges, with several OLR-type normal modes on the inner edge and five ILR-type modes on the outer edge. Once again, however, the pericenter longitudes of the edges are not aligned and the fitted apsidal rates are quite different. Hence, as in the case of the Herschel ringlet, the Laplace ringlet does not precess rigidly and does not conform to the usual dynamical picture of an eccentric ringlet.

The abundance of free normal modes at gap and ringlet edges is one of the key findings of this investigation. Consistently, we find free ILR-type normal modes ($m > 0$) at the outer edges of ringlets and the inner edges of gaps, and free OLR-type normal modes ($m \leq 0$) at inner ringlet edges and outer edges of gaps, as expected for a resonant cavity model of normal modes as the superposition of density waves reflected between a resonance located within the ring material and the free edge of the ring or gap. The general trend in features containing multiple modes is for the distance between resonance and ring edge to decrease with increasing wavenumber, as expected from the dispersion relation for density waves. We use these results to estimate the surface mass density and opacity of these features.

Throughout the Cassini Division, we find fitted precession rates that are, in general, slightly larger than the predicted values based on the Saturn's zonal gravity field alone. The overall radial trend in the excess rates matches the secular contribution expected from the nearby B ring, assuming a surface mass density of $\Sigma = 100$ gm cm^{-2}. However, the outer edges of the Huygens and Laplace gaps and the outer edge of the Laplace ringlet have conspicuously large residuals, exceeding their predicted precession rates by more than 0.03° d^{-1}. These patterns are probably are the result of forcing by nearby ring material, but at present we cannot account for the patterns in detail.

Acknowledgements

This work was supported in part by the NASA Cassini project and by the NASA Cassini Data Analysis Program, grant no. NNX09SE66G. We are grateful to P-Y. Longaretti for helpful discussions of ring dynamics and to R. Jacobson for his independent ring orbit solutions, confirming the validity of our RINGFIT results. We would also like to acknowledge the efforts of over two dozen Wellesley College undergraduate students—members of "Team Cassini"—who assisted in the measurements of over 15,000 individual ring occultation observations.

Supplementary material

Supplementary material associated with this article can be found, in the online version, at 10.1016/j.icarus.2016.03.017.

References

Acton, C.H., 1996. Ancillary data services of NASA's navigation and ancillary information facility. Planet. Space Sci. 44, 65–70.
Borderies, N., Goldreich, P., Tremaine, S., 1986. Nonlinear density waves in planetary rings. Icarus 68, 522–533.
Borderies, N., Longaretti, P.Y., 1987. Description and behavior of streamlines in planetary rings. Icarus 72, 593–603.
Bosh, A.S., 1994. Stellar occultation studies of Saturn's rings with the Hubble Space Telescope. (Ph.D. thesis). MIT, Cambridge, MA.
Colwell, J.E., Cooney, J.H., Esposito, L.W., et al., 2009. Density waves in Cassini UVIS stellar occultations. 1. The Cassini Division. Icarus 200, 574–580.
Colwell, J.E., Nicholson, P.D., Tiscareno, M.S., 2009. The structure of Saturn's rings. In: Dougherty, M., Krimigis, S. (Eds.), Saturn after Cassini-Huygens. Springer, pp. 375–412.
Cuzzi, J.N., Lissauer, J.J., Esposito, L.W., et al., 1984. Saturn's rings—Properties and processes. In: Greenberg, R., Brahic, A. (Eds.), IAU Colloquium 75: Planetary Rings. Univertiy of Arizona Press, Tucson, AZ, pp. 73–199.
El Moutamid, M., Nicholson, P.D., French, R.G., et al., 2016. How Janus' orbital swap affects the edge of Saturn's A ring. Icarus, in press.
Elliot, J.L., Bosh, A.S., Cooke, M.L., et al., 1993. An occultation by Saturn's rings on 1991 October 2–3 observed with the Hubble Space Telescope. Astron. J. 106, 2544–2572.
Esposito, L.W., Ocallaghan, M., Simmons, K.E., et al., 1983. Voyager photopolarimeter stellar occultation of Saturn's rings. J. Geophys. Res. 88, 8643–8649.
Flynn, B.C., Cuzzi, J.N., 1989. Regular structure in the inner Cassini Division of Saturn's rings. Icarus 82, 180–199.
French, R.G., Nicholson, P.D., Cooke, M.L., et al., 1993. Geometry of the Saturn system from the 3 July 1989 occultation of 28 SGR and Voyager observations. Icarus 103, 163–214.
French, R.G., et al., 2016. Deciphering the embedded wave in Saturn's Maxwell ringlet. Icarus. in press.
French, R.G., Kangas, J.A., Elliot, J.L., 1986. What perturbs the gamma and delta rings of Uranus? Science 231, 480–483.
French, R.G., Marouf, E.A., Rappaport, N.J., et al., 2010. Occultation observations of Saturn's B ring and Cassini Division. Astron. J. 139, 1649–1667.
French, R.G., Nicholson, P.D., Porco, C.C., et al., 1991. Dynamics and structure of the Uranian rings. In: Bertstralh, J.T., Miner, E.D., Matthews, M.S. (Eds.), Uranus. University of Arizona Press, Tucson, AZ, pp. 327–409.
Goldreich, P., Tremaine, S., 1982. The dynamics of planetary rings. Ann. Rev. Astron. Astrophys. 20, 249–283.
Goldreich, P., Tremaine, S.D., 1978. The formation of the Cassini Division in Saturn's rings. Icarus 34, 240–253.
Hedman, M.M., Nicholson, P.D., Baines, K.H., et al., 2010. The architecture of the Cassini Division. Astron. J. 139, 228–251.
Jacobson, R.A., Antreasian, P.G., Bordi, J.J., et al., 2006. The gravity field of the saturnian system from satellite observations and spacecraft tracking data. Astron. J. 132, 2520–2526.
Jerousek, R.G., Colwell, J.E., Esposito, L.W., 2011. Morphology and variability of the Titan ringlet and Huygens ringlet edges. Icarus 216, 280–291.
Lissauer, J.J., Shu, F.H., Cuzzi, J.N., 1981. Moonlets in Saturn's rings. Nature 292, 707–711.
Longaretti, P.-Y., Rappaport (formerly Borderies), N., 1995. Viscous overstabilities in dense narrow planetary rings. Icarus 116, 376–396.
Marouf, E.A., Tyler, G.L., 1986. Detection of two satellites in the Cassini Division of Saturn's rings. Nature 323, 31–35.
Nicholson, P.D., French, R.G., Tollestrup, E., et al., 2000. Saturn's rings I. Optical depth profiles from the 28 Sgr occultation. Icarus 145, 474–501.
Nicholson, P.D., Cooke, M.L., Pelton, E., 1990. An absolute radius scale for Saturn's rings. Astron. J. 100, 1339–1362.
Nicholson, P.D., French, R.G., Hedman, M.M., et al., 2014. Architecture of the Cassini Division revisited. Bull. Amer. Astron. Soc. 45, 402.01.
Nicholson, P.D., French, R.G., Hedman, M.M., et al., 2014a. Noncircular features in Saturn's rings: I. The edge of the B ring. Icarus 227, 152–175.
Nicholson, P.D., French, R.G., McGhee-French, C.A., et al., 2014b. Noncircular features in Saturn's rings: II. The C ring. Icarus 241, 373–396.
Porco, C., Danielson, G.E., Goldreich, P., et al., 1984. Saturn's nonaxisymmetric ring edges at 1.95 r_s and 2.27 r_s. Icarus 60, 17–28.
Porco, C.C., 1983. Voyager observations of Saturn's rings. 1: The eccentric rings at 1.29, 1.45, 1.95 and 227 RS (Ph.D. Thesis) California Institute of Technology, Pasadena, CA.
Porco, C.C., Baker, E., Barbara, J., et al., 2005. Cassini Imaging science: Initial results on Saturn's rings and small satellites. Science 307, 1226–1236.
Showalter, M.R., 1991. Visual detection of 1981S13, Saturn's eighteenth satellite, and its role in the Encke gap. Nature 351, 709–713.
Showalter, M.R., Cuzzi, J.N., Marouf, E.A., et al., 1986. Satellite 'wakes' and the orbit of the Encke gap moonlet. Icarus 66, 297–323.
Shu, F.H., 1984. Waves in planetary rings. In: Brahic, A., Greenberg, R. (Eds.), Planetary Rings. University of Arizona Press, pp. 513–561.
Smith, B.A., Soderblom, L., Batson, R.M., et al., 1982. A new look at the saturn system—The Voyager 2 images. Science 215, 504–537.
Spitale, J., Porco, C.C., 2006. Shapes and kinematics of eccentric features in Saturn's C ring and Cassini Division. Bull. Am. Astron. Soc. 38, 670.
Spitale, J.N., Porco, C.C., 2010. Detection of free unstable modes and massive bodies in Saturn's outer B ring. Astron. J. 140, 1747–1757.
Spitale, J.N., Hahn, J.M., 2016. The shape of Saturn's Huygens ringlet viewed by Cassini ISS. Icarus. in press.
Turtle, E., Porco, C., Haemmerle, V., et al., 1991. The kinematics of eccentric features in Saturn's Cassini Division from combined Voyager and ground-based data. Bull. Am. Astron. Soc. 23, 1179.
Tyler, G.L., Marouf, E.A., Simpson, R.A., et al., 1983. The microwave opacity of Saturn's rings at wavelengths of 3.6 and 13 cm from Voyager 1 radio occultation. Icarus 54, 160–188.